

PHYSICS-BASED EARTHQUAKE TRIGGERING AND FAULT
INTERACTIONS

A THESIS SUBMITTED TO
THE GRADUATE SCHOOL OF NATURAL AND APPLIED SCIENCES
OF
MIDDLE EAST TECHNICAL UNIVERSITY

BY

EYÜP SOPACI

IN PARTIAL FULFILLMENT OF THE REQUIREMENTS
FOR
THE DEGREE OF DOCTOR OF PHILOSOPHY
IN
GEODETICS - GEOGRAPHICAL INFORMATION TECHNOLOGIES

JANUARY 2023

Approval of the thesis:

**PHYSICS-BASED EARTHQUAKE TRIGGERING AND FAULT
INTERACTIONS**

submitted by **EYÜP SOPACI** in partial fulfillment of the requirements for the degree of **Doctor of Philosophy in Geodetics - Geographical Information Technologies Department, Middle East Technical University** by,

Prof. Dr. Halil Kalıpçılar
Dean, Graduate School of **Natural and Applied Sciences** _____

Prof. Dr. Zuhâl Akyürek
Head of Department, **Geodetics - Geographical Inf. Tech.** _____

Assoc. Prof. Dr. Atilla Arda Özacar
Supervisor, **Geological Engineering/GGIT, METU** _____

Examining Committee Members:

Prof. Dr. Ahmet Cevdet Yalçınır
Civil Engineering/GGIT, METU _____

Assoc. Prof. Dr. Atilla Arda Özacar
Geological Engineering/GGIT, METU _____

Assoc. Prof. Dr. Ali Özgün Konca
Geophysics, Boğaziçi University) _____

Prof. Dr. Zeynep Gülerce
Civil Engineering, METU _____

Assoc. Prof. Dr. Mustafa Abdullah Sandıkkaya
Civil Engineering, Hacettepe University _____

Date: 06.01.2023

I hereby declare that all information in this document has been obtained and presented in accordance with academic rules and ethical conduct. I also declare that, as required by these rules and conduct, I have fully cited and referenced all material and results that are not original to this work.

Name, Surname: Eyüp Sopacı

Signature :

ABSTRACT

PHYSICS-BASED EARTHQUAKE TRIGGERING AND FAULT INTERACTIONS

Sopacı, Eyüp

Ph.D., Department of Geodetics - Geographical Information Technologies

Supervisor: Assoc. Prof. Dr. Atilla Arda Özacar

January 2023, 134 pages

The knowledge of earthquake triggering and stress coupling mechanisms suffer data reliability in time and space. Here, the problems are analyzed with physics-based models to fill this gap using the most established empirical friction laws. First, the effects of certain state laws on earthquake triggering are analyzed in both numerical and analytical methods. The results reveal that mechanical state changes depend highly on the healing and weakening terms, and under certain conditions, the dynamic triggering effects can be quantified. The numerical studies on the Izmit (Mw7.6, 17.08.1999) - Düzce (M7.2, 12.11.1999), Ridgecrest (M6.4, 04.06.2019 - Mw7.1, 07.06.2019), Samos rupture (Mw7.0, 30.10.2020) case studies demonstrate reasonably matching failure time advance to the nature. The investigation of the triggering potential of the moderate Mw5.8 Earthquake on the locked segment of Marmara showed that the moderate earthquake could not induce instant triggering but hasten the failure time. The large earthquake synchronization and clustering observed in nature, including the North Anatolian Fault Line, was studied with long earthquake simulation runs. The conceptual model can mimic such coupled large fault segments similar to NAF, indicating when and how faults behave more predictably. The results indicate a slow

creep process at the velocity strengthening sections play a key role in triggering and fault stress transfer, pointing out that the mechanism is mostly dynamic triggering, despite conventional models of static triggering that can well explain the aftershock recurrences. The higher stress loads do not necessarily sustain better synchronized predictable failures in time and space, but they can lead to more complexity. In order to identify a fault zones synchrony behavior, PGV, and shear waves with tracking the post-slip relaxation process are crucial.

Keywords: Earthquake simulation, Rate-and-state friction, Pseudo-spectral method, Earthquake triggering, Fault synchronization

ÖZ

FİZİK TEMELLİ DEPREM TETİKLEME VE FAY ETKİLEŞİMLERİ

Sopacı, Eyüp

Doktora, Jeodezi ve Coğrafi Bilgi Teknolojileri Bölümü

Tez Yöneticisi: Doç. Dr. Atilla Arda Özacar

Ocak 2023 , 134 sayfa

Deprem tetikleme ve stres etkileşimi mekanizmaları, zaman ve uzayda yeterli veri imkanları olmadığı için tam olarak bilinmemektedir. Bu problemler, en yerleşik ampirik sürtünme yasalarını kullanarak fizik tabanlı modellerle analiz edilmiştir. İlk olarak belirli "durum" yasalarının deprem tetikleme üzerindeki etkileri hem sayısal hem de analitik yöntemlerle analiz edilmiştir. Sonuçlar, mekanik durum değişikliklerinin büyük ölçüde iyileşme ve zayıflama terimlerine bağlı olduğunu ve belirli koşullar altında dinamik tetikleyici etkilerin ölçülebileceğini ortaya koymaktadır. İzmit (Mw7.6, 17.08.1999) - Düzce (Mw7.2, 12.11.1999), Ridgecrest (Mw6.4, 04.06.2019 - Mw7.1) ile ilgili sayısal çalışmalar, 07.06.2019), Sisam kırılması (Mw7.0, 30.10.2020) vaka çalışmaları, doğaya makul bir şekilde eşleşen tetikleme sürelerini simüle edilebildiğini göstermiştir. Marmara'nın kilitli segmentinde orta şiddette Mw:5.8 Depremin tetikleme potansiyeli de bu çalışma kapsamında incelenmiş, sonuçlara göre bu orta büyüklükteki depremin anlık büyük bir depremi tetikleyemediği ancak bu süreyi hızlandırabilmiş olduğunu göstermektedir. Kuzey Anadolu Fay Hattı da dahil olmak üzere doğada gözlemlenen büyük deprem senkronizasyonu ve kümelenmesi, uzun deprem simülasyon çalışmaları ile incelenmiştir. Kavramsal fizik abanlu modeller ile, bu tür

etkileşimli büyük fay segmentlerinin simüle edilebildiği görülmüştür. Sonuçlar, fayların ne zaman ve nasıl daha öngörülebilir davrandığını göstermektedir. Özellikle, bir yırtılmaya karşı bariyer göre gören fay kesimlerinde görülen yavaş sürünme hareketinin, tetiklemede ve fay gerilimi aktarımında kilit bir rol oynadığı görülmüştür. Ayrıca, daha konvensiyonel modellerin öngördüğü üzere daha yüksek gerilim yükleri, zaman ve mekanda daha iyi senkronize edilmiş öngörülebilir deprem zamanlarını göstermekte, tam tersi, daha fazla karmaşıklığa yol açabilmektedir. Bir fay zonunun senkron davranışını belirlemek için, kayma sonrası gevşeme sürecini takip etmek PGV ve yırtılma hızları önemli göstergeler oldukları görülmüştür.

Anahtar Kelimeler: Deprem simülasyonu, Rate-and-state sürtünme, Spektral method, Deprem tetikleme, Fay senkronizasyonu

To my family

ACKNOWLEDGMENTS

Firstly I would like to thank my supervisor Dr. Arda Özacar for his continuous support, encouraging attitude, and immense knowledge. I feel really lucky to have him as my advisor and mentor.

Besides, I would like to thank the rest of my committee, Dr. Ali Özgün Konca, Dr. Ahmet Cevdet Yalçın, Dr. Zeynep Gülerce, and Dr. Mustafa Abdullah Sandıkkaya, for their insightful comments and encouragement and provocative questions to improve knowledge and quality of the researches.

I thank my fellows Raşit Uluğ, Amir Yeganehsahab, Hakan Bora Okay, Feyza Sakil, and Ozan Kılıç for sharing views, spending time together, and their positive attitudes.

Lastly, my family deserves endless gratitude. I am grateful to my mother Gülümser Sarı and my sister Başak Sopaç for their continuous support. My beloved partner Merve Toker, was always with me, supportive and motivating, sharing the happiness and pain. Without her, nothing could be more joyful.

TABLE OF CONTENTS

ABSTRACT	v
ÖZ	vii
ACKNOWLEDGMENTS	x
TABLE OF CONTENTS	xi
LIST OF TABLES	xv
LIST OF FIGURES	xvi
LIST OF ABBREVIATIONS	xxvii
CHAPTERS	
1 INTRODUCTION	1
1.1 Motivation and Problem Definition	1
1.2 Proposed Methods and Models	3
1.3 Contributions and Novelties	3
1.4 Publications	7
1.5 Software Contribution	8
1.6 The Outline of the Thesis	8
2 STATIC AND TRANSIENT TRIGGERING OF LARGE EARTHQUAKES: SENSITIVITY ANALYSIS AND CASE STUDIES ON İZMIT-DÜZCE AND RIDGECREST EARTHQUAKE SEQUENCES	9
2.1 Introduction	9

2.2	Model	10
2.2.1	Rate and State Friction	10
2.2.2	Single degree of freedom spring-mass system	11
2.2.3	Synthetic triggering signals	11
2.2.4	Simulation strategy	13
2.3	Sensitivity Analyses	14
2.3.1	Analytic approach	14
2.3.2	Numerical simulations	17
2.3.2.1	Triggering Onset time	17
2.3.2.2	Triggering parameters	21
2.3.2.3	System Parameters	24
2.4	CASE STUDIES	24
2.4.1	Simulation Results with possible scenarios	27
2.4.2	The transient triggering effects around the Ridgecrest	30
2.5	DISCUSSION	33
2.6	CONCLUSION	35
3	IMPACT OF 2019 MW 5.8 MARMARA SEA EARTHQUAKE ON THE SEISMIC CYCLE OF LOCKED NORTH ANATOLIAN FAULT SEGMENT	37
3.1	Introduction	37
3.2	Data and Methodology	40
3.2.1	Data	40
3.2.2	Methodology	41
3.2.3	Simulation Set-up	46

3.3	Simulation Results	47
3.3.1	State Laws	47
3.3.2	Simulation Strategy	49
3.3.3	Fault Complexity	49
3.4	Discussion and Conclusion	54
4	SIMULATION OF SEISMIC TRIGGERING AND FAILURE TIME PERTURBATIONS ASSOCIATED WITH THE 30 OCTOBER 2020 SAMOS EARTHQUAKE (MW 7.0)	59
4.1	Introduction	60
4.2	Coulomb static stress changes	61
4.3	Aftershock evolution in time and space	63
4.4	Numerical simulation	66
4.4.1	Methodology and Data	66
4.5	Simulation results	71
4.6	Discussion and conclusion	74
5	SIMULATION OF LARGE EARTHQUAKE SYNCHRONIZATION AND IMPLICATIONS ON NORTH ANATOLIAN FAULT ZONE	81
5.1	Introduction	82
5.2	Simulation Set-up	86
5.3	Simulation Results	89
5.3.1	Classification of Results	89
5.3.2	Sensitivity Analyses	94
5.3.3	The roles of static and dynamic triggering	101
5.3.4	Indicator of synchronization and predictability of large earthquakes	101

5.4	Discussion On Synchronization	104
5.4.1	The State laws	105
5.4.2	Static or Transient triggering?	105
5.4.3	Sensitive parameters	105
5.4.4	Observable Indicators for synchronization and predictability of large Earthquakes	107
5.4.5	Simplified inertial effects on numerical simulations	107
5.5	Implications On NAF	108
5.6	Conclusion	110
6	CONCLUSION	111
	REFERENCES	113
	APPENDICES	
A	FULL INERTIAL EFFECTS ON SYNCHRONIZATION	129
B	CURRICULUM VITAE	133

LIST OF TABLES

TABLES

Table 2.1	Classification of earthquakes with respect to peak ground velocities .	17
Table 2.2	The default RSF and system parameters used in simulations	19
Table 2.3	Cases and Scenarios	30
Table 3.1	Simulation Parameters	46
Table 4.1	Simulation Parameters	69
Table 5.1	Simulation Parameters	88

LIST OF FIGURES

FIGURES

Figure 2.1	Showing a) fault analogy and b) Spring block system. The figure is re-drawn from [1]	12
Figure 2.2	a) Transient triggering idealized by an oscillatory signal b) static stress change idealized by a step function	13
Figure 2.3	A transient wave train is idealized for a transient triggering signal whose certain parts (amplitude Δ_{PGV} and period of oscillation is T) exceed a threshold (solid red line) and lead to a state change of a fault.	14
Figure 2.4	Analytically computed strength drops for each state law. The fault patch is triggered by a simple sine wave with various PGVs, the induced strength drops are plotted. The parameters and color codes are given in the small box and legend	16
Figure 2.5	Analytically computed sensitivities analyses when a rectangular-shaped transient triggering is applied: Horizontal axes are tuned parameters. Vertical axes are strength drops due to transient triggering.	18
Figure 2.6	Clock advance and triggering delay illustration: When a triggering signal is applied to a fault at the on set time t_p , the failure time of a fault may advance, which is called clock advance T_a . Alternatively, the earthquake does not occur exactly during the onset time, but rather delay in time, called triggering delay T_d . Time before the unperturbed failure T_b is identical to onset time t_p , which will be often referred to in this study.	20

Figure 2.7 Effects of dynamic, static, combined, static+transient triggering signals on the earthquake cycle: Horizontal axis is the time before unperturbed failure T_b identical to the onset time of triggering signal. The vertical axis is the induced clock advance due to the triggering signal. Dotted, dash-dotted, solid, and dashed lines represent dynamic, static, combined, and static+transient triggering signals, respectively. A, B, C, and D points refer $T_b = 10$ Perrin law, $T_b = 5$ Ruina law, $T_b = 5$ Nagata law, and $T_b = 75$ Dieterich law, respectively. The marker type and line colors are the same as in figure 2.4. 22

Figure 2.8 The transient triggering instances which are marked in the figure 2.7: A) Perrin law ($T_b = 10$ years) induces an instant triggering. B) Ruina law ($T_b = 5$ years) weakens the state of contact, thus reducing the frictional strength, during the passage of triggering waves. C) Nagata law ($T_b = 5$ years) have a qualitatively different pattern than other state laws, because of the stress weakening effect. As seismic waves pass the state of contact oscillates as well. D) Dieterich law ($T_b = 75$ years) can not cause a stress drop, because the healing term is dominant. 23

Figure 2.9 Sensitivity to triggering parameters: (Up-left) Amplitude of dynamic signal. (Down-left) Duration of dynamic signal (total duration is $6 \times t_w$). (Up-right) Frequency of dynamic signal. (Down-right) The amplitude of the static triggering signal. The transient triggering signals are applied at $T_b = 5$ years. The parameters are given in the table 4.1. Line colors and marker types are the same as Figure 2.4. 25

Figure 2.10 Numerically calculated sensitivity to system parameters for transient triggering: Horizontal axes are tuned parameters. Vertical axes are induced clock advances 26

Figure 2.11 Case Study Region A) Mw7.4 İzmit (07.08.1999)-Mw7.2 Düzce (12.11.1999) B)Mw6.4 (04.07.2019) - Mw7.1 (06.07.2019) Ridgecrest earthquake sequences. The aftershocks are plotted with orange circles. Triggering earthquakes are plotted in blue and triggered earthquakes with red. C) Example of a triggering signal belongs to station 8108 near the triggered Düzce fault. 28

Figure 2.12 Simulation results of the Düzce triggering case: The x and y axes are time before unperturbed failure (years) and triggering delay (months). The results of each state evolution law are plotted as individual subplots. The five scenarios are applied for each law and plotted with different line types. The shaded region shows triggering delay between 1-6 months 29

Figure 2.13 Simulation results of the Ridgecrest triggering case: The x and y axes are time before unperturbed failure (years) and triggering delay (days). The results of each state evolution law are plotted as individual subplots. The five scenarios are applied for each law and plotted with different line types. The shaded region shows a triggering delay between 1-30 days 31

Figure 2.14 Simulation results of the Ridgecrest triggering case: The system with default parameters is simulated with the horizontal components of all available stations. The strength drops values are plotted with colors, given in the color bar. Peak ground velocities and peak ground frequencies are plotted as contours as green and light blue color. In the inset figure, the attenuation of dynamic effects and the PGV values are given. 32

Figure 3.1 The map shows the moderate (M_w :5.8) earthquake, its mechanism and aftershocks [2], and primary/secondary faults along the Main Marmara Fault (MMF) of NAF [3, 4] and mechanism of earthquakes on the adjacent segments with their surface ruptures [5, 6]. The contour lines show the peak ground velocity values estimated after the main shock by USGS (<https://earthquake.usgs.gov/earthquakes/eventpage/us700051kl/map>). The Eastern component of the waveform recorded by the strong motion station TK-3412 (location is shown on the map with the inverted triangle) is plotted below with its spectral amplitudes, which is used as the dynamic triggering signal in the simulations. 38

Figure 3.2 The conceptual model used in this study consists of three fault zone, including a velocity-weakening friction circular asperity that is the nucleation point of the next large earthquake, a velocity-strengthening brittle-to-creep transition zone, and a deep ductile zone. Plate velocity is assumed to be constant and moderate earthquake is inserted into the fault system externally. 41

Figure 3.3 The induced failure time advance (vertical) versus triggering time before failure t_b in years (horizontal). Subplots show triggering simulation results of different state laws. Each scenario is plotted with a different line width, type, transparency, and color, as shown in the legend. If applied, static stress is 0.1MPa, and *dyn* in the legend denotes the dynamic triggering signal multiplied by $\times 5$ and $\times 10$ in the relevant scenarios. 48

Figure 3.4 The figure compares quasi-static-full-dynamic (FD), and quasi-dynamic (QD) approaches. On the right, velocity v , state Θ and stress τ time series of unperturbed cycles for Ruina (on top) and Dieterich (below) are plotted for FD (blue) and QD (red). On the left, plots of induced failure time advance vs. triggering onset time before failure are shown separately for different scenarios, as given in the legend. . . 50

Figure 3.5 The effects of depth-dependent complexity with varying stress coupling control parameter c_d , and ϕ angle on the recurrence time are plotted. The horizontal and vertical axes are the time and slip, and colors are defined in the legend. The Ruina law is applied with the FD simulation strategy for $a_{vw} = 0.005$. Note that to sustain better visualization, transition and ductile zones are shifted. 51

Figure 3.6 Figure shows how the VW asperity size and the stress coupling affect the of fault’s sensitivity. The horizontal and vertical axes are the onset time of the triggering signal before its failure and the induced clock advances in normalized percentage. Dynamic, static and full (static and dynamic simultaneously) triggering signals are applied with size (asperity half length L_{vw}) and control coupling c_d parameter, defined in the legend. The Ruina law is applied with the FD simulation strategy for $a_{vw} = 0.001$ 52

Figure 3.7 Figure shows how ϕ angle between the stressing direction and fault interface affect the triggering. The horizontal and vertical axes are the onset time of the triggering signal before its failure and the induced clock advances in normalized percentage. The Ruina law is applied with the FD simulation strategy for $a_{vw} = 0.001$ 53

Figure 4.1 Topography and bathymetry map showing relocated hypocenter (star), rupture area (yellow outlined rectangle) and focal mechanism solution of the 30 October 2020 Samos Earthquake identified from regional waveform modeling [7] along with regional moment tensor solutions of aftershocks [8] and active fault segments (compiled from the Neotectonic map of Greece by [9, 10, 11, 12]. Two strong-motion stations near Samos (SMG1) and İzmir (3519) which are used during simulations are also plotted in the map. 62

Figure 4.2 Coulomb static stress changes at a depth of 8 km. The large-scaled map is in the middle, and rupture edge close-ups with contour lines are given on the sides. The red rectangle and green line represent the projected rupture plane and fault trace at the surface, respectively. Solid lines represent faults. The relocated aftershocks shown by green circles are from [7] which are available online at http://www.geerassociation.org/administrator/components/com_geer_reports/geerfiles/TableS1.cat (accessed on 9.7.2021). The dashed magenta ellipse outlines the location of the SE cluster displaying delayed triggering. 64

Figure 4.3 Time versus longitude and latitude plots (at the top) and daily maps (bottom) of relocated aftershocks taken from [7] (available online, web address is given in the caption of Figure 4.2). The grey area and ellipses outline the rupture area and aftershock clusters showing almost instant and delayed triggering. The black stars represent the mainshock and large aftershocks (green) within the western cluster and preceding SE cluster at $t \approx 50$ and 80 h. Note that aftershock data is color-coded according to magnitude (top) and hour of the day (bottom). 65

Figure 4.4 The fault analogies using single-degree-of-freedom (SDF) models. a) vertical strike-slip fault with a single asperity patch, b) spring-slider representation of vertical strike-slip faulting, c) a normal fault with an inclination angle (ϕ), d) spring-slider representation of inclined normal faulting. The figures are redrawn from [1, 13] for vertical and inclined faults, accordingly. 67

Figure 4.5 The seismic waveforms (on the left) are used for dynamic earthquake triggering and their unfiltered amplitude spectrums (on the right). Station SMG1, located in Samos Island, is operated by the Institute of Engineering Seismology & Earthquake Engineering (ITSAK), and station 3519, located in Karşıyaka, İzmir, Turkey is operated by the Disaster and Emergency Management Presidency of Turkey (AFAD). Check Figure 4.1 for station locations. 71

Figure 4.6	Triggering simulation results of large characteristic and $M_w \approx 4$ earthquakes with different recurrence times (RC) on normal and strike-slip faults analogous to the delayed triggering observed SE side of the Samos Island. a) absolute clock advance plots for fixed fault slip rate V_{PL} of 3 mm/year. b) normalized clock advance plots for variable V_{PL} .	73
Figure 4.7	Triggering simulation results of large characteristic, $M_w 3.5$ and $M_w < 3.5$ earthquakes on a vertical strike-slip fault for variable Coulomb static stress change analogous to the almost instant triggering observed west of the rupture.	75
Figure 4.8	Far-field dynamic triggering simulation results showing normalized clock advance plots of large characteristic and $M_w 4$ earthquakes on normal faults analogous to faults nearby İzmir.	75
Figure 5.1	Map showing the historical earthquakes along North Anatolian Fault zone (a-e) and synchronized clusters, and its approximate recent situation (f). The historical earthquake catalog is compiled from studies [14, 15, 16, 17, 18]	83
Figure 5.2	Simulation set-up: a) Initial values, b) a representation fault model.	86
Figure 5.3	A synchronization example using slip law and default parameters in Table 5.1. a) slip profile: slip velocities are plotted in the logarithmic scale defined in the color bar on the right side. The dynamic rupture is plotted in two-second intervals, and post- or pre-seismic events are plotted with scatter plot until they reach a critical value $v_c = 10^{-8} m/s$. The inter-seismic times are plotted with black dashed lines every 20 years interval. b) time series of the middle of each asperity. The colors are given in the legend. c) Synchronization status of adjacent segments. Solid thin lines and scatters without face color denote constraint fit to normalized adjacent segment's failure time differences. The filled color scatters and bold dashed lines denote the deviations from the constraint fit.	90

Figure 5.4 A synchronization example using aging law with default parameters in Table 5.1. a) slip profile: slip velocities are plotted in the logarithmic scale defined in the color bar on the right side. The dynamic rupture is plotted in two-second intervals, and post- or pre-seismic events are plotted with scatter plot until they reach a critical value $v_c = 10^{-8}m/s$. The inter-seismic times are plotted with black dashed lines every 20 years interval. b) time series of the middle of each asperity. The colors are given in the legend. c) Synchronization status of adjacent segments. Solid thin lines and scatters without face color denote constraint fit to normalized adjacent segment's failure time differences. The filled color scatters and bold dashed lines denote the deviations from the constraint fit. 91

Figure 5.5 A complex example using aging law with default parameters in Table 5.1, except the barrier length decreased to 10km. a) slip profile: slip velocities are plotted in the logarithmic scale defined in the color bar on the right side. The dynamic rupture is plotted in two-second intervals, and post- or pre-seismic events are plotted with scatter plot until they reach a critical value $v_c = 10^{-8}m/s$. The inter-seismic times are plotted with black dashed lines every 20 years interval. b) time series of the middle of each asperity. The colors are given in the legend. c) Synchronization status of adjacent segments. Solid thin lines and scatters without face color denote constraint fit to normalized adjacent segment's failure time differences. The filled color scatters and bold dashed lines denote the deviations from the constraint fit. 92

Figure 5.6 An independent status example using slip law with default parameters in Table 5.1, except the barrier length increased to 20 km and $a_{bar} - b = 0.003$. a) slip profile: slip velocities are plotted in the logarithmic scale defined in the color bar on the right side. The dynamic rupture is plotted in two-second intervals, and post- or pre-seismic events are plotted with scatter plot until they reach a critical value $v_c = 10^{-8}m/s$. The inter-seismic times are plotted with black dashed lines every 20 years interval. b) time series of the middle of each asperity. The colors are given in the legend. c) Synchronization status of adjacent segments. Solid thin lines and scatters without face color denote constraint fit to normalized adjacent segment's failure time differences. The filled color scatters and bold dashed lines denote the deviations from the constraint fit. 93

Figure 5.7 Figure showing all examples labeled as "synchronized" in this study. The color and line codes are given in the legend. 95

Figure 5.8 Figure shows the effects in barrier length and its frictional properties change on the synchronization. The horizontal and vertical axes are the earthquake cycle and the failure time differences between adjacent asperities. The effects of a change in the barrier's frictional properties ($a_{bar} - b$) and state types are plotted in vertical and horizontal orders, respectively. The failure time differences between right-middle and left-middle asperities are plotted with solid and dashed lines, and their colors indicate barrier lengths, given in the legends. Unless otherwise stated, the parameters are set to the default values in table 5.1. . . . 98

Figure 5.9 Figure shows the effects of asperity’s frictional properties, size, and critical slip distance changes on the synchronization. The horizontal and vertical axes are the earthquake cycle and the failure time differences between adjacent asperities. The effects of a change in the asperity’s direct velocity effect parameter a_{asp} , critical slip distance d_c , and asperity length L_{asp} are plotted vertically for aging and state laws, respectively. The failure time differences between right-middle and left-middle asperities are plotted with solid and dashed lines, and changes in parameters are plotted with different colors, given in the legends. The barrier’s frictional property is set to $a_{bar} - b = 0.003$ as default in this figure. In inset figures, this parameter is set to $a_{bar} - b = 0.005$. The rest of the parameters are set to the default values in table 5.1. 99

Figure 5.10 The plot shows how fast the faults are synchronized with changing certain parameters. The so-called convergence rates (β_1 of fitted deviance) are plotted on the top. The middle row shows the converged values, defined by the failure time differences in percentage between two successive large earthquakes of adjacent faults normalized by mean recurrence time. The lower row is the converged cycle defined, after which cycle faults synchronize. 100

Figure 5.11 5 full successive full ruptures and post-seismic propagation of middle asperity are plotted. The default parameters in table 5.1 are used, except $a_{bar} - b = 0.003$. On the left and right, the propagation on the barrier is plotted with colored lines that define the time and state law, given in the color bar. In the middle subplots, the propagation on the middle asperity is plotted with 5 seconds intervals. Rupture times are written in the middle plot for each state law with the color code defined in the color bar. 102

Figure 5.12 The stress propagation of complex and synchronized simulations are plotted for full ruptures on the middle asperity and continuation on the left and right barrier. The plotted waves correspond to the highest amplitudes of the first-fourth ruptures on the middle asperity and 5km away from it. The parameters for simulation are written on the first subplot (upper-left) and plotted with a color code for the synchronization status given in the legend. For both aging and slip law, complex and synchronized status simulations correspond to different $a_{bar} - b$ values given in the first column. 103

Figure 5.13 Distribution stats of slip event vs Peak Ground Velocity (PGV) . 104

Figure 5.14 The Map (a) shows the synchronized segments along NAF in different color codes, and historical earthquakes on it (green circles) and most recent earthquakes (Time>1900) with the yellow stars. The segment boundaries are highlighted with a black frame on map (a) and plotted on a larger scale in b-d. The possible barriers are highlighted in the large yellow circles in subplots b-d. 109

Figure A.1 The rupture difference between full-dynamic, and quasi-dynamic (inertial effects are simplified to radiation damping as all the simulations done in the main manuscript. The frames are plotted every 2 seconds for a two-asperity model. The color code for plots are given in the legend 130

Figure A.2 Plots show the difference between FD and QD. The time series of stress are given on upper subplots. The slip profiles for qd (left) and fd (right) are given in below figures. 131

LIST OF ABBREVIATIONS

ABBREVIATIONS

RSF	Rate-and-State Friction
QS-FD	Quasi-Static and Full-Dynamic
QD	Quasi-Dynamic
FD	Full-Dynamic
SSM	Spring slider Model
1D	1 Dimensional
2D	2 Dimensional
2.5D	2.5 Dimensional
3D	3 Dimensional
NAF	North Anatolian Fault
MMF	Main Marmara Fault

CHAPTER 1

INTRODUCTION

1.1 Motivation and Problem Definition

This thesis studies earthquake triggering, asperity barrier interaction, fault synchronization, and clustering of large earthquakes, on physics-based models. Those phenomena are observed in nature, but their origin mechanisms are inadequately understood, because of the fact that the dense seismologic and geodetic networks are recently available comparable to long recurrence cycles of large characteristic earthquakes [18, 17, 14, 16, 19, 20, 21]. The numerical simulations are valuable tools to fill this gap [22, 23, 24, 25, 26, 21, 27, 28]. Especially, the laboratory-based empirical Rate-And-State frictions [29, 30, 31, 32, 33] are well-established models for shear resistance from slow to dynamic slip rates, and implemented to many aspects of faults [34, 33, 35, 36].

The earthquake triggering with the conventional Coulomb models by assuming permanent static stress changes at the particular sections of the fault zone depending on the focal mechanism of ruptures have been well-established and appears to agree well with aftershock distribution [37, 38]. Yet, quantifying the triggering of earthquakes by means of other earthquakes' seismic waves or any temporal oscillatory wave acting on the fault interface is not straightforward as a static triggering case [39]. The most important reason is the fact that the dynamic effects are mostly nested in static triggering nearby, overshadowed by static effects. Therefore, the simplest explanation emerges as remote and small events triggered by dynamic and in close range static triggering is the main reason [40, 41, 42]. The explanations seem fair, but the static failure models fail to explain the after-slip distribution after the M7.3 Landers

(1992) earthquake [39, 43], or M7.2 Düzce (12.11.1999) rupture triggered by M7.4 İzmit (17.08.1999) [44]. The numerical simulations using rate and state friction [45] argued either static and dynamic triggering have different mechanisms, or the conventional static triggering should be revised.

The earthquake triggering by means of static, dynamic, and combined using rate-and-state friction and other failure models were studied both numerically [1, 46, 45, 47, 48, 49, 50, 51] and through laboratory tests [41, 52]. However, especially the underlying exact mechanism of dynamic friction especially for the rear earthquake cases is still poorly understood [42]. More importantly, the studies so far did only two state law comparisons and indicated the state dependence [53], but a complete comparison among available state laws [54, 36, 33] in terms of triggering is still missing. Additionally, the studies were limited to synthetic signals, but their applicability to real waveforms and how can these conceptualized models mimic the real world are still missing.

The first problem deals with a complete comparison of the state laws by analytical and numerical approaches. Especially, the study focused on the most poorly understood dynamic triggering mechanism in a framework of complete comparison between state definitions of RSF laws and quantifying dynamic effects as parameters of observable waveforms. As a matter of fact that the "conceptual" nature of models and the possible effects, including state evolution effects, inertial terms, and stress coupling relations are investigated. The conceptual models were also tested by real case scenarios, such as Dü-İzmit earthquake triggering sequences (Chapter 2). During the study, two new earthquakes occurred. First, an M5.8 moderate earthquake on 26.09.2019 ruptured on a secondary fault connecting to the Main Marmara Fault's locked segment (Kumburgaz), which is thought to rupture soon with $M > 7$ [2] heated a debate about triggering a larger event. Therefore, the case is studied with similar conceptual models, to explain possible triggering scenarios 3. Then on 30.10.2020, a normal-type fault ruptured (M7) on the north of Samos island, and showed clear examples of delayed triggering with mixtures of different mechanisms. Those delayed triggering events were investigated by considering the different mechanisms with shear-stress coupling relations (Chapter 4).

The second problem aims to reveal earthquake synchronization. The historical earthquakes along the North Anatolian Fault (NAF) Zone demonstrate a pattern that large fault segments synchronize in time [55, 14, 56] and constitute clusters along the NAF. The cluster edges correspond to step-overs, according to the most valid theory those sections are velocity-strengthening barriers in the framework of RSF [24, 57]. Therefore, investigating long-time asperity-barrier interaction is of great importance because of the fact that those large events happen quasi-periodically and the mechanism could shed light on the triggering and synchronization mechanism of large events, predicting the timing of the next event (Chapter 5).

1.2 Proposed Methods and Models

In all chapters, the used model changes to fit the physical mechanism of interest, and they are explained in each chapter. In general, the used models assume the shear stress on the frictional interface obeys laboratory-based Rate and State friction [29, 30, 58, 32].

1.3 Contributions and Novelties

In Chapter 2, the conceptual model of a single spring slider system with shear stress following rate and state friction with different state evolution laws is studied. The model assumes a single isolated asperity with a regular circular shape, to allow pure effects of triggering signals, without interfering with complex relations. The analytical and numerical sensitivity analyzes are conducted especially to reveal dynamic triggering. This simplified conceptual model is tested with M7.4 İzmit (17.08.1999) - M7.2 Düzce (12.11.1999) real case triggering scenario. Our contributions in Chapter 2 are as follows:

- Both static and dynamic triggering have non-linearly on time, and their mechanisms differ.
- The dynamic triggering mechanism depends drastically on the state. This difference is insignificant for static triggering, especially when the fault is imma-

ture, resembling conventional coulomb-like failure.

- We derive analytical relation quantifying the dynamic triggering effect that is a function of the amplitude and frequency of an oscillatory signal. The derived formula agrees well with pure numerical results and suggests different sensitivity to state evolution, to their velocity change dependent "weakening" terms.
- Several simulation results using the slip law explained the clock delays of the Düzce earthquake ($M_w:7.2$, 12.11.1999) better.

Chapter 3 is a case study about the possible triggering effects of the M5.8 Marmara Sea earthquake (26.09.2019) on the Main Marmara Fault (MMF), which is locked and a possible large earthquake ($M > 7$) is expected. The conceptual model is a simple spring slider system governed by rate and state friction, but apart from the model in Chapter 2, the simplified and full inertial effects are involved. The complete triggering effects (static and combined) are tested on a specific model for the locked segment of MMF.

Our contributions in Chapter 3 are as follows:

- The moderate (M5.8) earthquake is weak to trigger the large pending Marmara earthquake. However, results show an advance in failure time, if the time to natural failure is less than 20 years, which is likely.

Chapter 4 is a case study on the observed off-fault delayed triggering events observed after the M7 Samos earthquake (30.10.2020). The earthquake happened during the study of this thesis, necessitating analyses using a simple spring slider system. Apart from the models in Chapter 2 and 3, the shear-normal stress coupling relation is applied to quantify the complex fault mechanism of aftershocks and possible faults nearby.

Our contributions in Chapter 4 are as follows:

- The variable-sized events after the main shock are simulated with a relation depending on the asperity size. Despite the simplicity of the model, the results

grasp the main features of earthquake triggering and explained the triggered aftershocks.

- Inclusion of shear-stress coupling relation demonstrates similarity and differences between the purely vertical fault models. The triggering signals show an increase in clock advance if the cycle time is early. This region corresponds to state evolution still prevails. If the cycle is in the end, the state evolution is either 0 or becomes negative and self-acceleration is about the start, the difference in the clock advance between the purely vertical and inclined faults with shear stress coupling disappears, and both models are identical.

Chapter 5 simulates the earthquake synchronization pattern in North Anatolian Fault Zone. The historical earthquake catalog displays regularly failing of large events in time, and large events form clusters where characteristic earthquakes generally nucleate and arrest. The cluster edges correspond to step-overs, an indication of velocity-strengthening barriers in the framework of rate and state friction. The synchronized behavior along North Anatolian Fault (NAF) Zone is examined on a conceptual continuum model, consisting of three strong asperity patches using the pseudo-spectral FFT method and Rate-and-State (RSF) dependent friction. The motivations are: first, is it possible to simulate the synchronization pattern of large earthquakes, likewise NAF, via physics-based numerical models? Second, if it is, what is the physical mechanism? Third, what are the implications for NAF and many other major fault zones? Fourth, which natural indicators point to rupture's triggering and synchronization potentials? Finally, this study could improve the knowledge of large earthquake behaviors which suffer scarce data availability and poor resolution, and help seismic risk hazard assessments.

Our contributions in Chapter 5 are as follows:

- The results suggest that a transient triggering mechanism mainly controls the synchronization behavior, unlike the traditional belief which states permanently raising or lowering stress on the asperity patch, which is called static triggering and is often quantified by Coulomb's stress failure criteria.
- The direct velocity effect a in the framework of RSF shows the highest sensitiv-

ity for synchronization, by altering two distinct processes on asperities, where earthquakes nucleate, and on barriers, where relaxation oscillation of loaded stress takes place.

- Particularly by changing the a parameter, and also depending on other factors including the barrier's length and its frictional properties, the coupling effect between the asperities can drastically change.
- An over-coupled stress interaction between asperities causes premature partial ruptures which leads to more "complex" earthquake recurrences, and prediction of triggered next earthquakes is extremely challenging.
- If the coupling is extremely weak, then the characteristic events are more regular and more predictable, with no synchronization pattern as it is labeled as "independent".
- The adequately coupled systems show synchronization analogous to NAF.
- The different "state" laws or contacting properties of interfaces in the framework of RSF resemble each other at the velocity-strengthening barrier, but they drastically differ in generating dynamic ruptures, hence the results also depend on the type of state definition significantly.
- The simulations and laboratory tests suggest empirical formulation for quantifying barrier efficiency that depends on the asperity-barrier size. However, our results show insensitivity to asperity size.
- Examination of over 275 simulation setups and 30000 earthquakes point to several indicators that can be observed in nature. The classified results as "complex", "independent", and "synchronized" offer distinguishable contrasts in rupture wave speeds, ground motion observable of pre-seismic, co-seismic, and post-seismic duration, and extents. The study indicates that rupture wave speeds, peak ground velocity, and tracking post-seismic slips are of great importance to define synchronization behavior and hence the predictability of the next large earthquakes in nearby faults.

1.4 Publications

The published journal article is as follows:

- Sopaci, E., and Özacar, A. A. (2021). Simulation of seismic triggering and failure time perturbations associated with the 30 October 2020 Samos earthquake (Mw 7.0). *Turkish Journal of Earth Sciences*, 30(5), 653-664.

Under review or yet to be submitted:

- Sopaci, E., and Özacar, A. A. (202X). Impact of 2019 Mw 5.8 Marmara Sea Earthquake on the Seismic Cycle of Locked North Anatolian Fault Segment. *Tectonophysics*, Manuscript number: TECTO15976, (Revision received from reviewers on 05 Dec 2022, during the time this thesis is being written).
- Sopaci, E., and Özacar, A. A. (202X). Simulation of Large Earthquake Synchronization and Implications On North Anatolian Fault Zone, Recently in preparation.
- Sopaci, E., and Özacar, A. A. (202X). Static and dynamic triggering of large earthquakes: sensitivity analysis and case studies on Izmit-Duzce and Ridge-crest earthquake sequences, Recently in preparation.

The conference presentations are as follows:

- Sopaci, E., and Özacar, A. A. (2020, May). Investigation of Dynamic and Static Effects on Earthquake Triggering Using Different Rate and State Friction Laws and Marmara Simulation. In *EGU General Assembly Conference Abstracts* (p. 533).
- Sopaci, E., and Özacar, A. A. (2021, April). Simulation of Instant and Delayed Seismic Triggering Observed After the 30 October 2020 Samos Earthquake at Nearby Faults. In *EGU General Assembly Conference Abstracts* (pp. EGU21-13090).
- Sopaci, E., and Özacar, A. A. (2022). Do Large Earthquakes along Major Faults Synchronize in Time? (No. EGU22-508). *Copernicus Meetings*.

1.5 Software Contribution

- Sopaci (2023). Discrete spring slider models for earthquake triggering simulations. on GitHub and Zenodo [59].
- Sopaci (2022) Spectral Boundary Integral Method for simulation of continuum fault models with applying full-inertial or simplified inertial effects. The shear stress of the interface is assumed to be Rate-And State Friction, with different contact history evolution effects. <https://github.com/eyupsopaci/sbiem> [60].

1.6 The Outline of the Thesis

This thesis is organized as follows: Chapter 2 provides a full sensitivity analysis of earthquake triggering plus a real case scenario. Chapter 3 investigates the triggering potential of the moderate (Mw:5.8) earthquake ruptured on a secondary fault connecting to the locked Kumburgaz fault segment. Chapter 4 simulates the off-fault delayed triggering events observed a few days after the Mw:7.0 Samos earthquake (30.10.2020). Chapter 5 studies asperity-barrier interaction, fault synchronization, and clustering of large events on NAF. Chapter 6 provides a conclusion to all chapters.

CHAPTER 2

STATIC AND TRANSIENT TRIGGERING OF LARGE EARTHQUAKES: SENSITIVITY ANALYSIS AND CASE STUDIES ON İZMIT-DÜZCE AND RIDGECREST EARTHQUAKE SEQUENCES

2.1 Introduction

A traditional view of earthquake triggering posits that static triggering occurs in close ranges while transient triggering occurs in remote and small earthquakes, mainly in geothermal or volcanic areas [61, 62]. However, observations suggest that transient signals can be as effective as static triggering in close cases or even be the dominant triggering mechanism [39, 43, 61, 63].

Transient influences can continue for hours and challenge simple failure models for aftershock occurrences. The exact mechanism of near-case earthquake triggering remains unresolved due to challenges in separating the influence of static and transient triggering [64, 50]. Physics-based models and laboratory tests using rate and state friction laws have been used to fill this gap, but the definition of state in these laws can differ, and their effect on earthquake triggering has not been thoroughly studied [1, 65, 66, 47, 13, 41, 42, 48, 49]. Conceptual and laboratory tests also provide conflicting results on the effect of oscillation frequency on triggering [1, 48, 67, 50, 42].

In this study, four state laws for static and transient triggering are revisited, and a comparison of rate and state dependent friction for earthquake triggering is conducted. A single-degree-of-freedom model is used with full inertial effects during rupture and mature faults. Numerical and analytical methods are used to analyze the transient and static triggering mechanisms', revealing the frequency dependence of transient triggering. Real earthquake sequences on M=7.6 İzmit 17-08-1999 - M:7.2 Düzce

12-11-1999 [68, 44] and M6.4 4.07.2019 - M7.1 06.07.2019 Ridgecrest [69, 70, 71] are used to test the conceptual model and evaluate the state laws in real-case scenarios.

2.2 Model

2.2.1 Rate and State Friction

The frictional strength is assumed to be the rate and state friction,

$$\tau = \sigma_n \mu = \tau_0 + \Theta + A \ln\left(\frac{v}{V_0}\right) \quad (2.1)$$

where τ , μ , and σ_n denote frictional strength, friction, and the effective normal stress. $\tau_0 = \mu_0 \sigma_n$ is reference strength depending on reference friction μ_0 at reference velocity V_0 . The second term is the state of contact which is equal to $\Theta = B \ln(V_0 * \theta / d_c)$ in the original form, and the third term is the velocity-dependent component $A \ln(\frac{v}{V_0})$. $A = \sigma_n a$, $B = \sigma_n b$, and d_c are empirical constants defined as direct velocity and state evolution effect parameters and the critical slip distance. The state is defined by one of the following evolution formulas.

$$\frac{d\Theta_D}{dt} = \frac{BV_0}{D_C} \exp\left(-\frac{\Theta}{B}\right) - \frac{B}{d_c} v \quad (2.2)$$

$$\frac{d\Theta_R}{dt} = -\frac{v}{D_c} \left[\Theta + B \ln\left(\frac{v}{V_0}\right) \right] \quad (2.3)$$

$$\frac{d\Theta_P}{dt} = \frac{BV_0}{2d_c} \exp\left(-\frac{\Theta}{B}\right) - \frac{B}{2D_C V_0} v^2 \exp\left(\frac{\Theta}{B}\right) \quad (2.4)$$

$$\frac{d\Theta_N}{dt} = \frac{BV_0}{d_c} \exp\left(-\frac{\Theta}{B}\right) - \frac{B}{d_c} v - C \frac{d\tau}{dt} \quad (2.5)$$

Equations (2.2, 2.3, 2.4 and 2.5) are the state evolution for aging or Dieterich law [29], slip or Ruina law [30], a modified law of Dieterich by [31] or simply Perrin law and modified law of Dieterich by [32] or simply Nagata law, respectively. Hereafter we refer to them by the first author's name for convenience as Dieterich, Ruina, Perrin,

and Nagata laws. Each state law has miscellaneous views o friction, healing (first), and weakening (second) terms [33, 36]. The Nagata law has an additional stress-weakening scaled with empirical constant C term and requires a scaling relation to compare uniquely given by [54].

$$A_N/(C + 1) = A_R \quad d_c(C + 1) = d_c \quad (A - B)_N = (A - B)_R \quad (2.6)$$

where, subscripts N and R denote Nagata and Ruina, respectively. The parameters for Dieterich, Ruina, and Perrin laws are assumed to be identical.

2.2.2 Single degree of freedom spring-mass system

The equation of motion of a fault analogy, shown in figure 2.1, is given by.

$$m\ddot{\delta} = \tau_e + \Delta\tau_S - \tau_f \quad (2.7)$$

where m and δ denote mass per unit area and slip, respectively and dots are derivatives with respect to time t . The first term in the right-hand side of the equation 2.7 is the elastic traction $\tau_e = K(\delta_0 + X_T(t) - \delta)$, a transient signal $X_T(t)$ changes temporarily the loading stress as the slip deficit between the loading and the asperity's nucleation points $(\delta_0 - \delta)$ increases, that is multiplied by the elastic fault stiffness $K = \Gamma G/L$, approximated by the ratio between the shear modulus G and linear length of the patch L , with a patch geometry parameter $\Gamma \approx 1$ [72]. Mass per unit area is approximated by $m \approx (T/2\pi)^2 K$, where T is the period of freely oscillating mass [73]. The second and third terms in the equation 2.7 are static stress change and frictional stress given in the equation 2.1, respectively.

2.2.3 Synthetic triggering signals

In this study, two types of triggering (transient and static) are applied, whose shapes are illustrated in figure 2.2. The first one is the transient oscillatory signal enveloped within a Gaussian pulse [72].

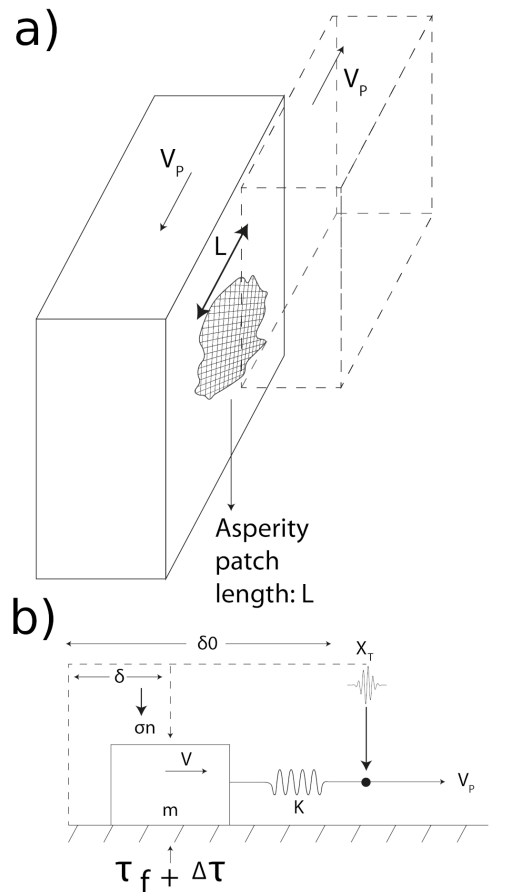


Figure 2.1: Showing a) fault analogy and b) Spring block system. The figure is re-drawn from [1]

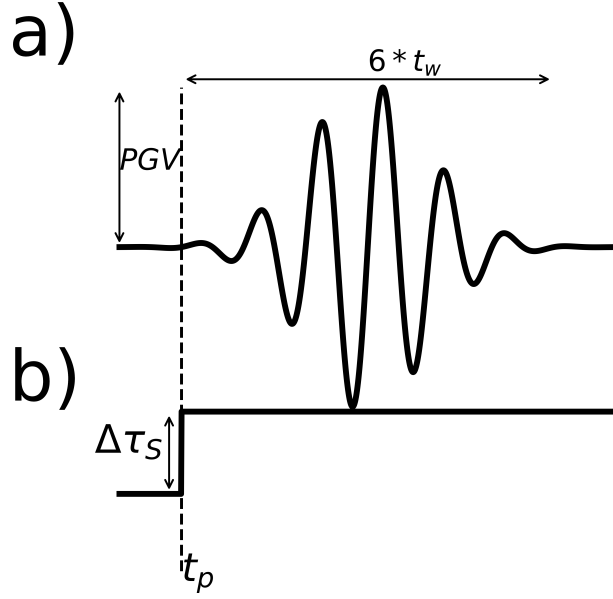


Figure 2.2: a) Transient triggering idealized by an oscillatory signal b) static stress change idealized by a step function

$$\dot{X}_T(t) = \Delta_{PGV} \sin(2\pi f_0 t) \exp\left[-\frac{(t - t_p - 3t_w)^2}{2t_w^2}\right] \quad (2.8)$$

where Δ_{PGV} , f_0 , t_p , t_w denote peak ground velocity (PGV), frequency, onset time, and duration of the transient triggering signal. The total length of the triggering oscillating transient signal is $6t_w$.

A Heaviside function approximates the permanent static stress increase (or decrease).

$$\Delta\tau_S = \begin{cases} \Delta\tau_s & \text{if } t \geq t_p \\ 0 & \text{otherwise} \end{cases} \quad (2.9)$$

where $\Delta\tau_s$ is the amplitude of the stress.

2.2.4 Simulation strategy

The quasi-static approach replaces the equation of motion during the slow phase if the slip rate is smaller than a critical value $v < V_C = 100\mu/s$ and the frictional strength is set equal to elastic traction with $\tau_e = \tau_f$ [73]. Otherwise ($v \geq V_C$), the inertial

effects are included in the fast phase using equation 2.7. The Adams' and backward differentiation formula solves the equation of slow and fast phases, considering their stiffness change [74].

2.3 Sensitivity Analyses

2.3.1 Analytic approach

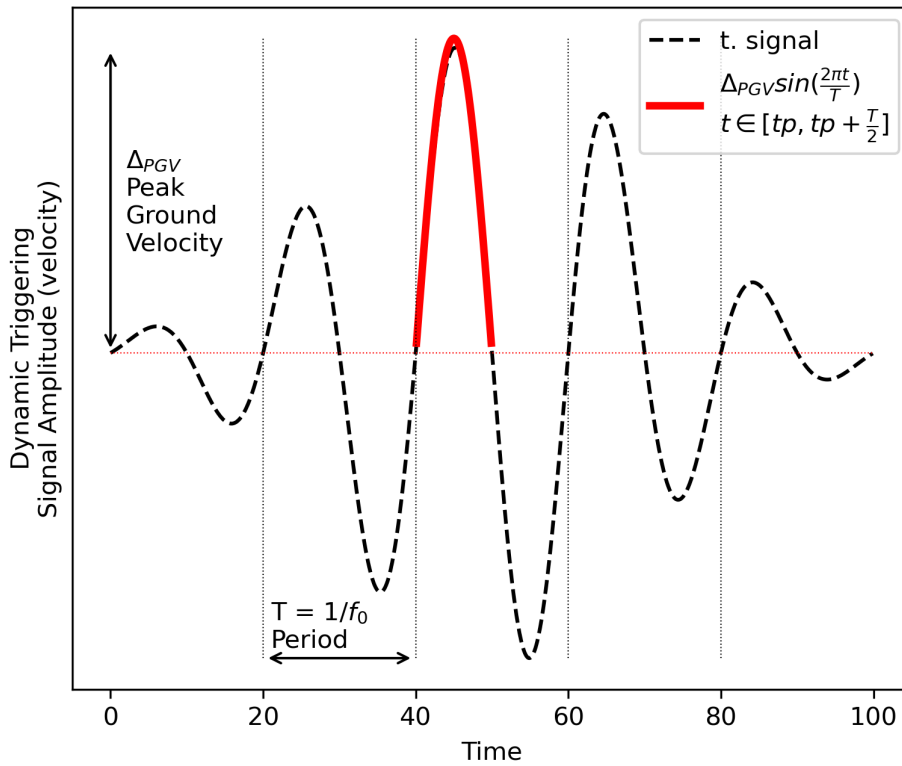


Figure 2.3: A transient wave train is idealized for a transient triggering signal whose certain parts (amplitude Δ_{PGV} and period of oscillation is T) exceed a threshold (solid red line) and lead to a state change of a fault.

$\tau_0 + \Theta$ defines the frictional strength during the slow evolution [36]. Θ heals slower (first terms of equations 2.2-2.5) as it increases, and eventually, a self acceleration begins after which the second weakening rates becomes more dominant depending

on the state law. The transient triggering effects depend highly on the time, activation of dynamic weakening term(s), and a threshold of effective transient signal's amplitude [1, 75]. Here, we assumed a conceptual transient signal in Figure 2.3, whose maximum amplitude part can exceed a threshold and induce a strength drop.

$$\dot{\tau}_X = K(V_P + \dot{X}_{T(t)} - v) \approx K\dot{X}_{T(t)} \quad (2.10)$$

, since v and V_P are negligible. Then, the passage of such a wave leads to,

$$\Delta\tau_X = \int_{t_p}^{t_p+T/2} K\Delta_{PGV} \sin\left(\frac{2\pi t}{T}\right) dt = \frac{KT\Delta_{PGV}}{\pi} \quad (2.11)$$

temporarily change in elastic stress. Induced slip and slip rate at the interface due to the transient perturbations can be approximated in analytical forms as [76].

$$\delta = -A/H \ln\left(\frac{\dot{\delta}_0 H}{\dot{\tau}_X} [1 - \exp \Delta\tau_X] + 1\right) \quad (2.12)$$

$$\dot{\delta} = \left(\frac{1}{\dot{\delta}_0} + \frac{H}{\dot{\tau}_X}\right) \exp \Delta\tau_X - \frac{H}{\dot{\tau}_X} \quad (2.13)$$

$H = \frac{B}{d_c} - K$ denotes the model constants. Note that we assume slip rates at the interface are equal to the plate's slip rate and the healing terms are negligible. Then the induced strength drops can be approximated by the following analytical relations.

$$d\Theta_D \approx -\frac{B}{d_c} \dot{\delta} dt \quad (2.14)$$

$$d\Theta_r \approx -\frac{\dot{\delta}}{d_c} (\Theta_{ss} - B \ln(\dot{\delta})) dt = -\frac{B}{d_c} \dot{\delta} \ln\left(\frac{\dot{\delta}}{v_0}\right) dt \quad (2.15)$$

$$d\Theta_P \approx -\frac{B}{2d_c} \frac{\dot{\delta}^2}{v_0} \exp\left(\frac{\Theta}{B}\right) dt \quad (2.16)$$

$$d\Theta_N \approx -\left(\frac{B_N}{d_{cN}} \dot{\delta} - C\dot{\tau}\right) dt \quad (2.17)$$

Note that due to the strict assumption that the fault is at the end of its seismic cycle and healing effects do not contribute to state evolution, the analytical relations have

shortcomings applying to nature. Yet it supports evaluating the state laws' response to the transient triggering.

We computed the strength drops using the analytical approximation and the parameters in table 4.1, shown in figure 2.4. The horizontal and vertical axes denote the PGV of the triggering signal (the frequency is constant and the initial values equal to the plate velocity V_{PL}) and strength drop, accordingly. The PGVs are changed according to damaging potential, in table 2.1.

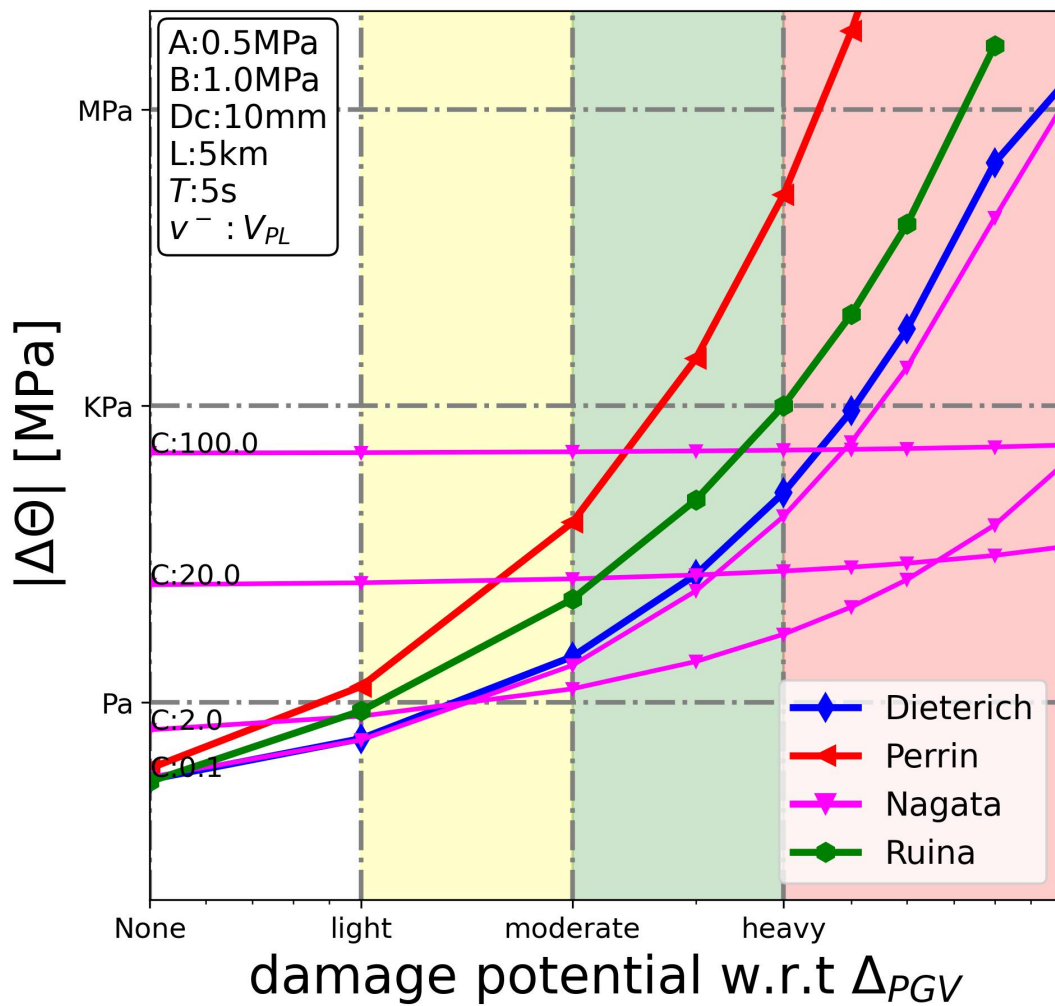


Figure 2.4: Analytically computed strength drops for each state law. The fault patch is triggered by a simple sine wave with various PGVs, the induced strength drops are plotted. The parameters and color codes are given in the small box and legend

According to the figure, Nagata law has a relatively different pattern due to its addi-

Table 2.1: Classification of earthquakes with respect to peak ground velocities

Shaking	Light	Moderate	Strong	Very Strong	Severe	Violent
Damage	None	Very light	Light	Moderate	Moderate heavy	Heavy
PGV[cm/s]	1.4	4.7	9.6	20	41	86

The scales are taken from [77]

tional stress weakening term. When triggering amplitudes are weak, the extra stress weakening term promotes a higher strength drop. This value increases as the C value increases. On the other hand, the scaling relation increases the resistance against the perturbation, hence higher values of C lead to also less sensitive to triggering.

Perrin is the most sensitive law to transient triggering because of the square dependence of triggering velocity. The second sensitive state evolution is the Ruina law and Dieterich law is the less sensitive to velocity perturbation.

Analytically computed parameter sensitivities are shown in figure 2.5. According to the results, the asperity patch size (velocity weakening) " L ", direct velocity effect A , and effective normal stress σ_n are the sensitive parameters to the triggering process. In contrast, the state evolution effect B , and critical slip distance d_c have no significant impact. The positive constant of Nagata law " C " is also secondarily sensitive for the triggering process.

2.3.2 Numerical simulations

We analyze sensitive parameters using numerical simulations, with the default parameters given in the table 4.1. Clock advance, triggering delay, or stress drop is used as an indicator interchangeably. Definitions of indicators are illustrated in figure 2.6.

2.3.2.1 Triggering Onset time

Figure 2.7 shows that the earthquake triggering is non-linearly dependent on the onset time of the triggering signal. The static, dynamic, combined, and static+transient

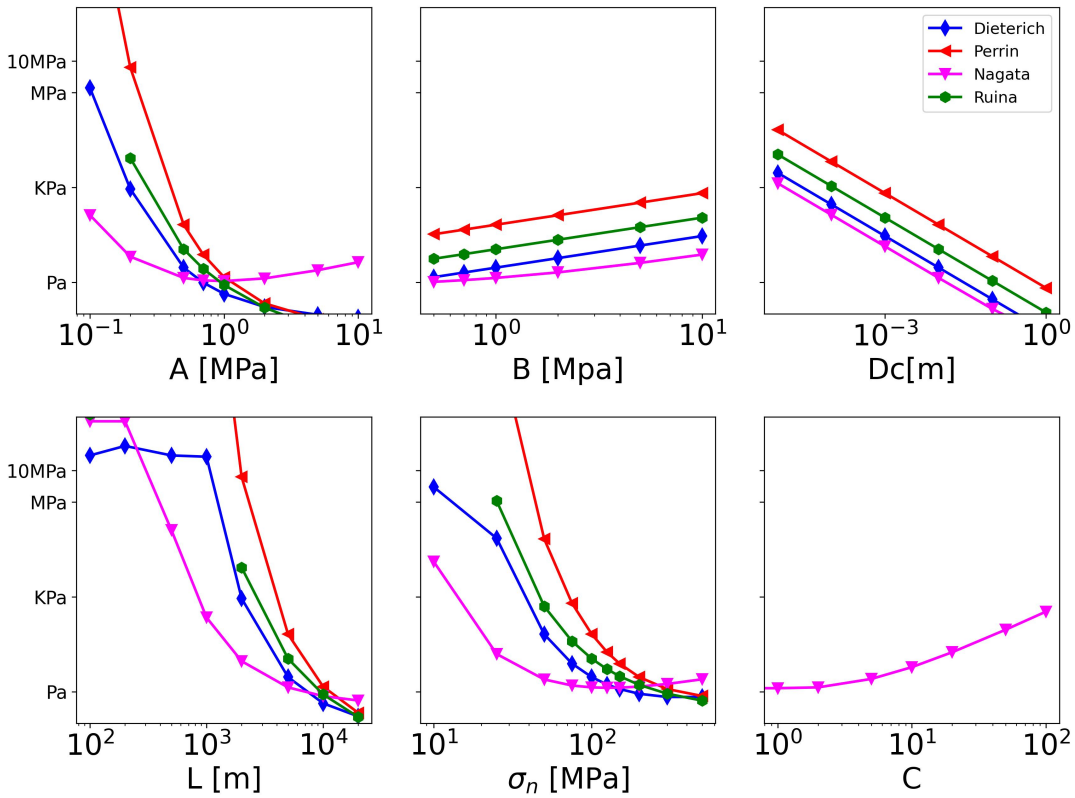


Figure 2.5: Analytically computed sensitivities analyses when a rectangular-shaped transient triggering is applied: Horizontal axes are tuned parameters. Vertical axes are strength drops due to transient triggering.

Table 2.2: The default RSF and system parameters used in simulations

Parameter	Value	Unit	Description
G	3×10^4	(MPa)	Shear modulus
L	5	(km)	Length of the patch
σ_n	100	(MPa)	Effective normal stress
V_{PL}	20	(mm/yr)	Plate slip rate
A	0.5	(MPa)	Direct velocity effect
B	1	(MPa)	State evolution effect
d_c	1	(mm)	Critical slip distance
C	20		stress state coupling constant
Δ_{PGV}	30	(cm/s)	Peak ground velocity
$\Delta\tau_S$	0.1	(MPa)	Static stress change
f_0	0.05	(Hz)	triggering signal frequency
t_w	20	(s)	triggering duration ($6 \times t_w$)
T	5	(s)	oscillating period

Default values for simulations, unless otherwise stated. The recurrence time is 250 years.

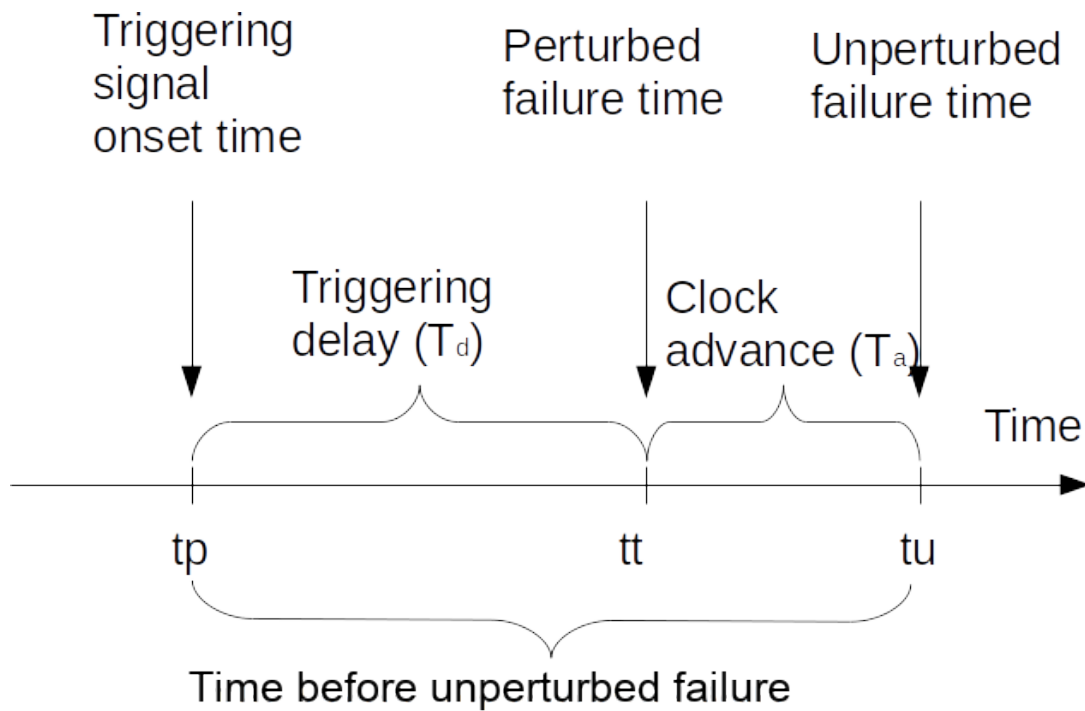


Figure 2.6: Clock advance and triggering delay illustration: When a triggering signal is applied to a fault at the onset time t_p , the failure time of a fault may advance, which is called clock advance T_a . Alternatively, the earthquake does not occur exactly during the onset time, but rather delay in time, called triggering delay T_d . Time before the unperturbed failure T_b is identical to onset time t_p , which will be often referred to in this study.

triggering signals using the parameters in the table 4.1 are plotted in the same figure, to compare their effectiveness.

Firstly, transient triggering appears to be effective only if the time to instability T_b is short enough, corresponding to activation of the weakening term and negligible healing term. The numerical results agree well with the analytical results given in figure 2.4. Among the state laws, the Perrin law exhibits the most sensitivity to the transient triggering, due to its exponential velocity change dependence, so that for $T_b \leq 10$ values it displays instant triggering. The Ruina law's sensitivity to transient triggering is also higher than the rest, which has a linear weakening rate to velocity change. Dieterich and Nagata laws with logarithmic weakening rate (and stress weakening for The Nagata law) do not show much sensitivity to transient triggering, similar to the analytical results. The triggering instances of state laws, marked as A, B, C, D in figure 2.7, are shown in figure 2.8. The A sub-figure plots the instant triggering event of the Perrin law when $T_b = 10$ years. B reveals how the state of contact is decreased as an oscillatory signal is passing by for the Ruina law when $T_b = 5$ years. C shows that due to the stress weakening term, Nagata law's state oscillates as a triggering signal passes. D reveals no change in the state of contact for the Dieterich law because the clock is still early and the healing effect prevails for $T_b = 75$ years.

In contrast to transient triggering, all state laws exhibit quite identical static stress change for large values of T_b . This value agrees well with Coulomb's failure criteria with a constant stressing rate $T_a = \Delta\tau_s/\dot{\tau}$. The deviation between the state laws emerges, with smaller values of T_b . The slip law shows the most clock advance followed by Perrin, Deiterich, and Nagata, similar to analytical results. Static triggering shows dominance over dynamic effects for combined triggering examples unless the simulation leads to an instant triggering as in Perrin's law. The superimposed individual static and transient triggering results show a non-linear effect such that their sum is not equal to the combined triggering.

2.3.2.2 Triggering parameters

We analyze sensitivity to peak ground velocity, frequency, and duration of a transient triggering and amplitude of the static signal (Figure 2.9). In terms of transient trigger-

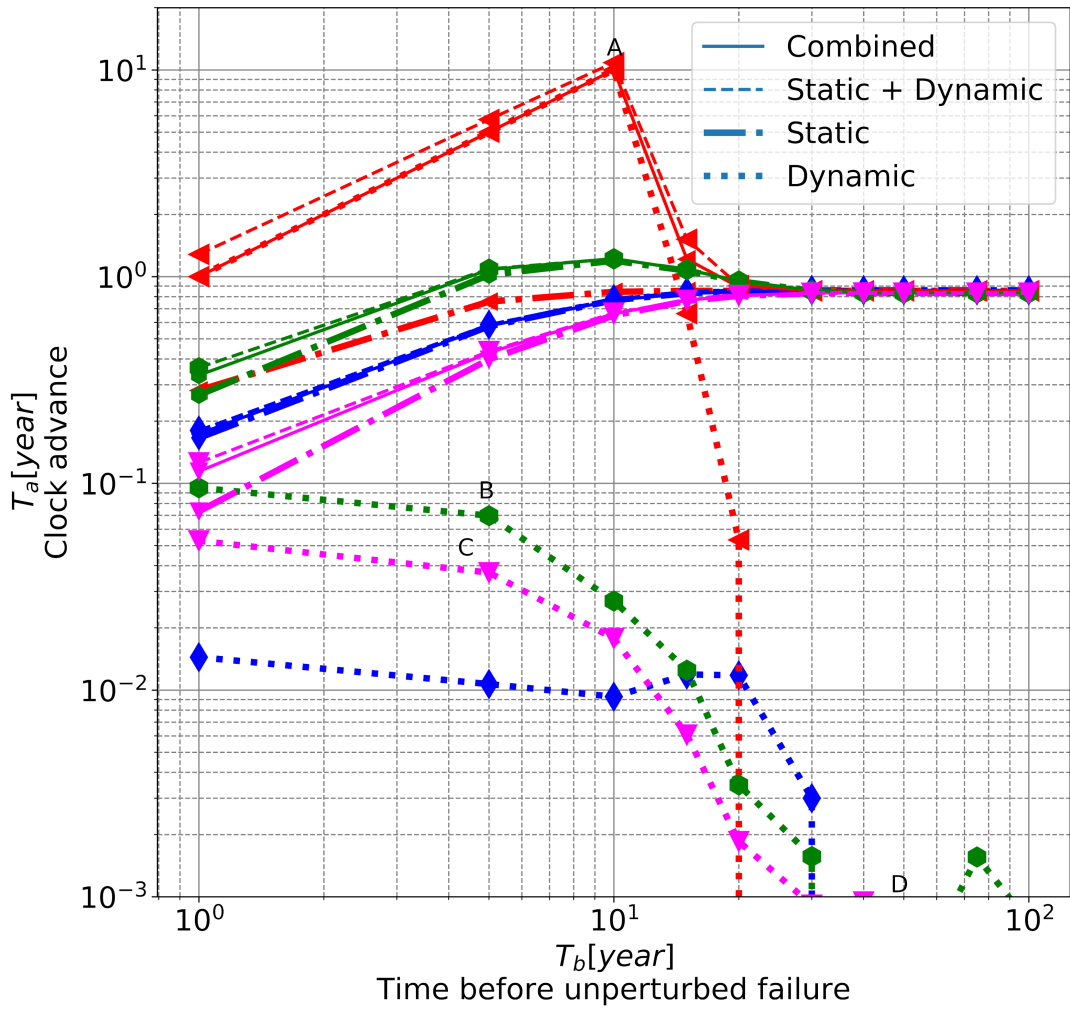


Figure 2.7: Effects of dynamic, static, combined, static+transient triggering signals on the earthquake cycle: Horizontal axis is the time before unperturbed failure T_b identical to the onset time of triggering signal. The vertical axis is the induced clock advance due to the triggering signal. Dotted, dash-dotted, solid, and dashed lines represent dynamic, static, combined, and static+transient triggering signals, respectively. A, B, C, and D points refer $T_b = 10$ Perrin law, $T_b = 5$ Ruina law, $T_b = 5$ Nagata law, and $T_b = 75$ Dieterich law, respectively. The marker type and line colors are the same as in figure 2.4.

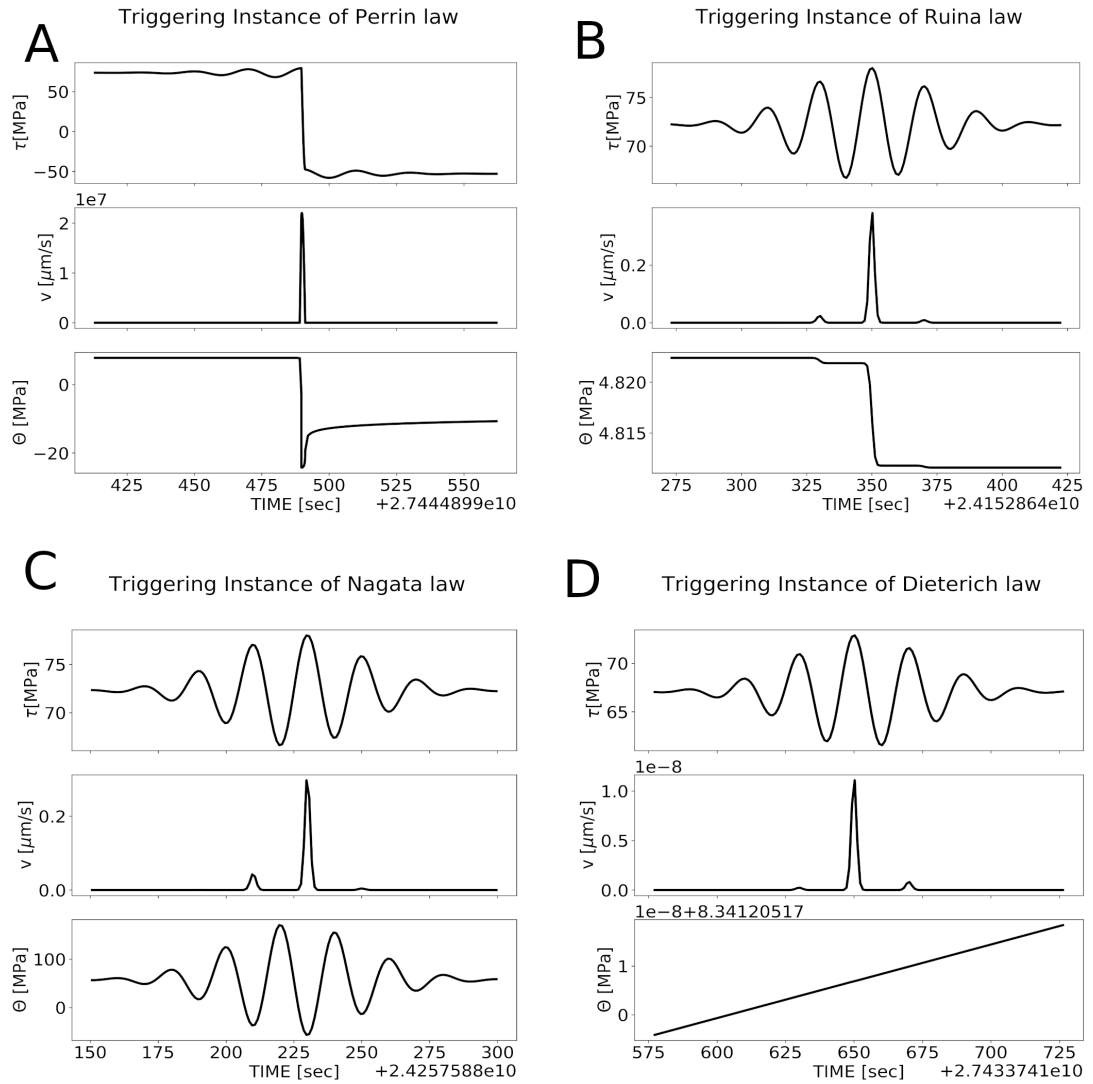


Figure 2.8: The transient triggering instances which are marked in the figure 2.7: A) Perrin law ($T_b = 10$ years) induces an instant triggering. B) Ruina law ($T_b = 5$ years) weakens the state of contact, thus reducing the frictional strength, during the passage of triggering waves. C) Nagata law ($T_b = 5$ years) have a qualitatively different pattern than other state laws, because of the stress weakening effect. As seismic waves pass the state of contact oscillates as well. D) Dieterich law ($T_b = 75$ years) can not cause a stress drop, because the healing term is dominant.

ing, higher amplitude, and lower frequency signals have higher triggering potential. Amplitude and frequency significantly control the triggering process, while duration has a linear effect. We also test the sensitivity to static triggering in the lower right sub-figure of 2.9. Higher amplitude static triggering means higher induced clock advance. Besides, for large values, the T_b value shows a linear triggering dependence.

2.3.2.3 System Parameters

The fault parameters' sensitivity is analyzed by the numerical simulations, with the keeping default parameters in table 4.1 constant, and changing the specific parameter. The time to failure is assumed to be $T_b = 5$ years. Figure 2.10 displays a good agreement with the analytical results. Asperity patch size L , direct velocity effect parameter A , and effective normal stress parameter σ_n are sensitive parameters, and state evolution effect B and d_c parameters display insensitivity. The stress coupling parameter C displays a minor sensitivity that is applicable only to Nagata law.

2.4 CASE STUDIES

Two real cases, shown in figure 2.11, are studied to test for the reliability of the conceptual models and also for comparison between the state laws. The first case is İzmit (M:7.6, 17-08-1999) and Düzce (M:7.2, 12-11-1999) earthquake sequence (Figure 2.11-A) along the North Anatolian Fault Zone. The Düzce earthquake occurred after three months after the İzmit earthquake, showing an example of a large earthquake triggering in near cases. The strong motion record very close to the nucleation point of the Düzce rupture (Figure 2.11-C) indicates that a pulse-like shape and the PGV values exceeding 40cm/s lifts the transient triggering potential. The coulomb static stress change studies reported that the maximum static stress increases can reach as much as 1MPa [78]; [44]. Such a static increase points out according to Coulomb's Static Failure model that the clock advance could be a maximum of 0.8 years with of $\Delta\tau_{CSF} = 1\text{MPa}$ of stress load and stressing rate of $\dot{\tau} = 0.12\text{MPa/yr}$. Therefore, it is either possible that Düzce segment was already at the end of it is cycle (approximately one year was left to failure), or the secondary mechanism, including transient

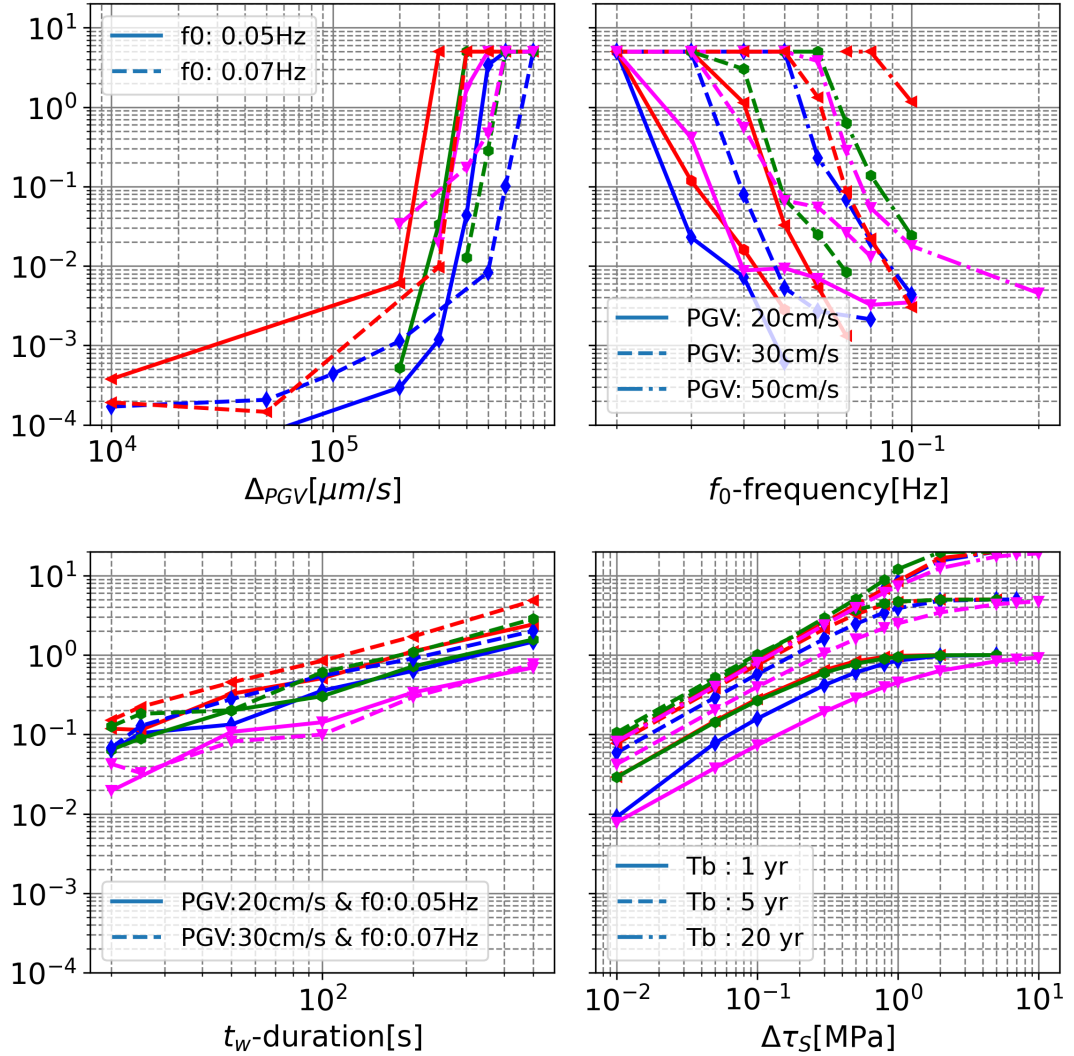


Figure 2.9: Sensitivity to triggering parameters: (Up-left) Amplitude of dynamic signal. (Down-left) Duration of dynamic signal (total duration is $6 \times t_w$). (Up-right) Frequency of dynamic signal. (Down-right) The amplitude of the static triggering signal. The transient triggering signals are applied at $T_b = 5$ years. The parameters are given in the table 4.1. Line colors and marker types are the same as Figure 2.4.

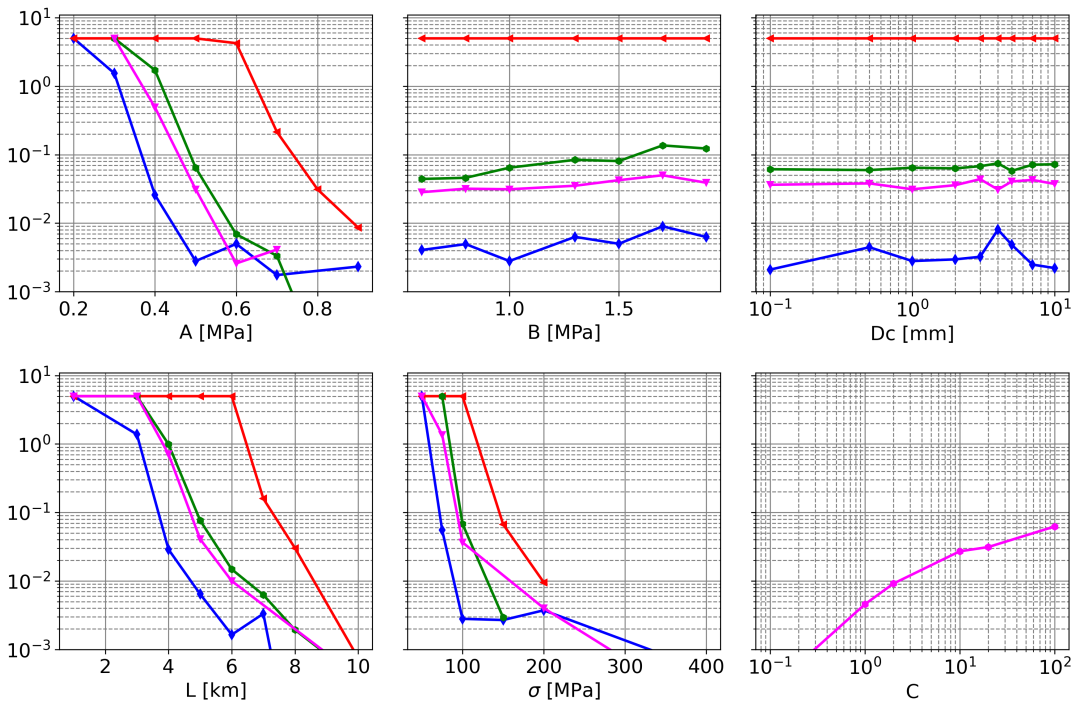


Figure 2.10: Numerically calculated sensitivity to system parameters for transient triggering: Horizontal axes are tuned parameters. Vertical axes are induced clock advances

triggering, accelerated the rupture process.

The second case is the left lateral (M:6.4, 04-07-2019) and right lateral (M:7.1 06-07-2019) earthquake sequences in Ridgecrest. The earthquake sequences provides a valuable example to test the triggering mechanism, because of dense instrumentation of which some closer ones are plotted in Figure 2.11-B. We specifically used the TOW2 station in our combined simulations by testing several scenarios. The maximum static stress release reaches to $0.2MPa$ [79], [80] and [81]. But we also used all possible stations and simulated the frictional strength changes that could affect future earthquakes, using only the transient triggering signals for the given location.

The recorded seismic waveforms are strong motion data. We first applied the station responses and then remove the trend mean value. Then, we integrate the time series using the trapezoidal rule to obtain the velocity time series. Also, low-pass butterworth filtering of order three is applied to eliminate noise in the data. The time series and frequency spectrum of the 8101 (Düzce) are shown in figure 2.11-C.

2.4.1 Simulation Results with possible scenarios

First we analyse Mw7.4 İzmit (07.08.1999)-Mw7.2 Düzce (12.11.1999) case. The RSF parameters are used similarly to from [1] and [47], by setting $b - a = 0.005$ and changing the a . We set asperity patch 5 km for Düzce case [68] and normal stress to $\sigma_n = 100MPa$. The plate velocity is approximately $20mm/y$. This simulation setup generates approximately 250 years, and 30MPa stress drops, similar to characteristic earthquakes along NAF. The coulomb static stress is around $0.3MPa$ close to the hypo-center and reaches up to $1MPa$ after İzmit earthquake [78], [44] within the Düzce rupture segment. We set the minimum static stress change at 0.5 MPa and increase it up to 1 MPa during the simulations. We use the E-W channel of station 8101 approximately in the direction of Düzce rupture, whose PGV reaches $50cm/s$. The triggering delay is used as the indicator, and 1-6 months of triggering delay values are shaded in the plots (figure 2.12). According to the results, static stress change alone is weak to cause three months of triggering delay, unless the system had already a few months to its unperturbed failure (Sc:1). If the combined triggering is applied, a dynamic signal can amplify the triggering effects (Sc:2). If the static triggering signal

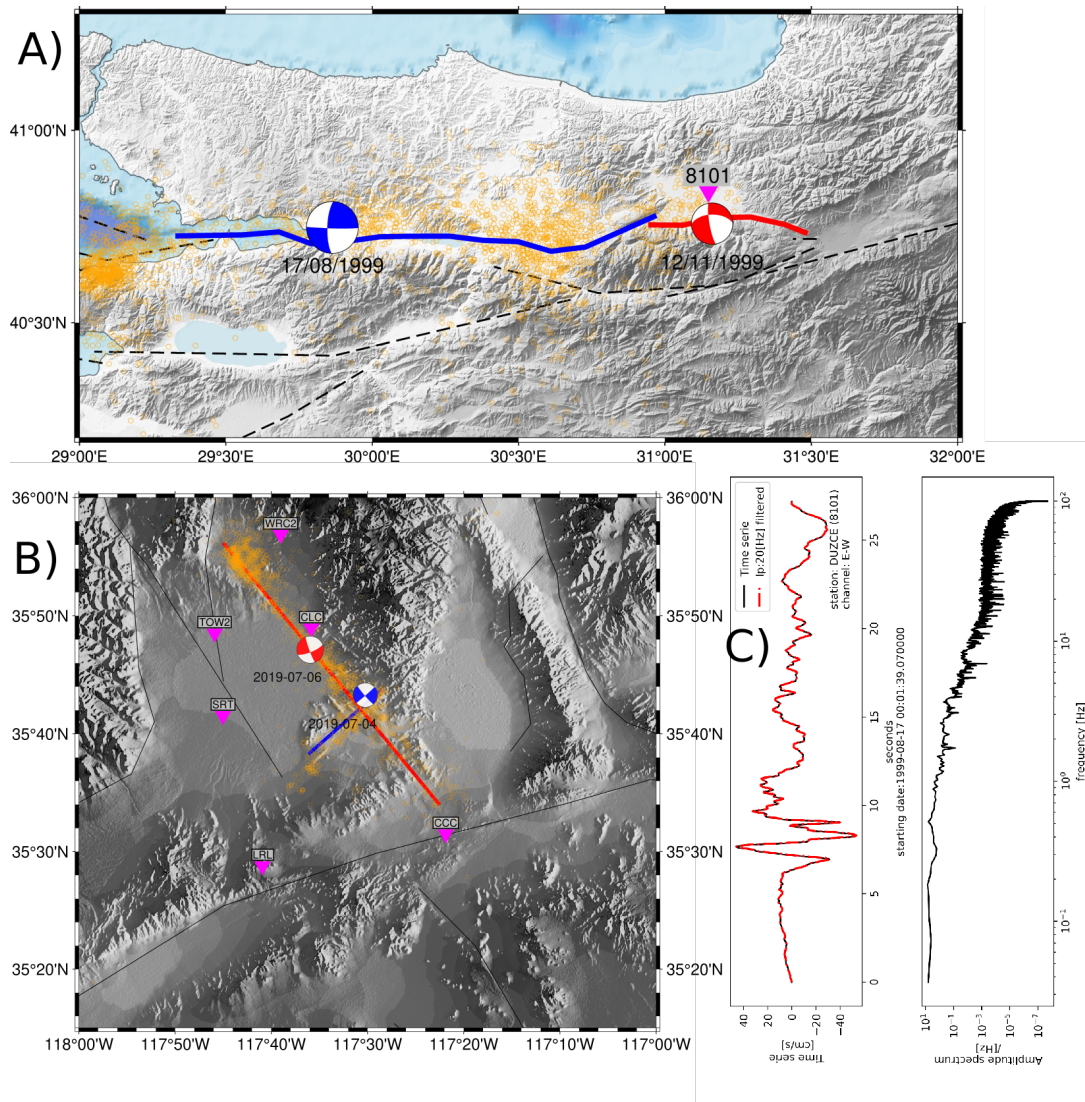


Figure 2.11: Case Study Region A) Mw7.4 İzmit (07.08.1999)-Mw7.2 Düzce (12.11.1999) B) Mw6.4 (04.07.2019) - Mw7.1 (06.07.2019) Ridgecrest earthquake sequences. The aftershocks are plotted with orange circles. Triggering earthquakes are plotted in blue and triggered earthquakes with red. C) Example of a triggering signal belongs to station 8108 near the triggered Düzce fault.

is increased to the upper limit (Sc:3), more solutions lie within the shaded region. In Sc 4 and 5 we decrease the direct velocity effect parameter to $A = 0.3MPa$. While Dieterich and Nagata evolution laws show little sensitivity to the change, Perrin and Ruina laws lie better in the shaded region, when T_b values are less than (10 - 15) years. Perrin law, on the other hand, leads to instant triggering when the T_b value is less than 20 years if transient triggering is also included (Sc:5).

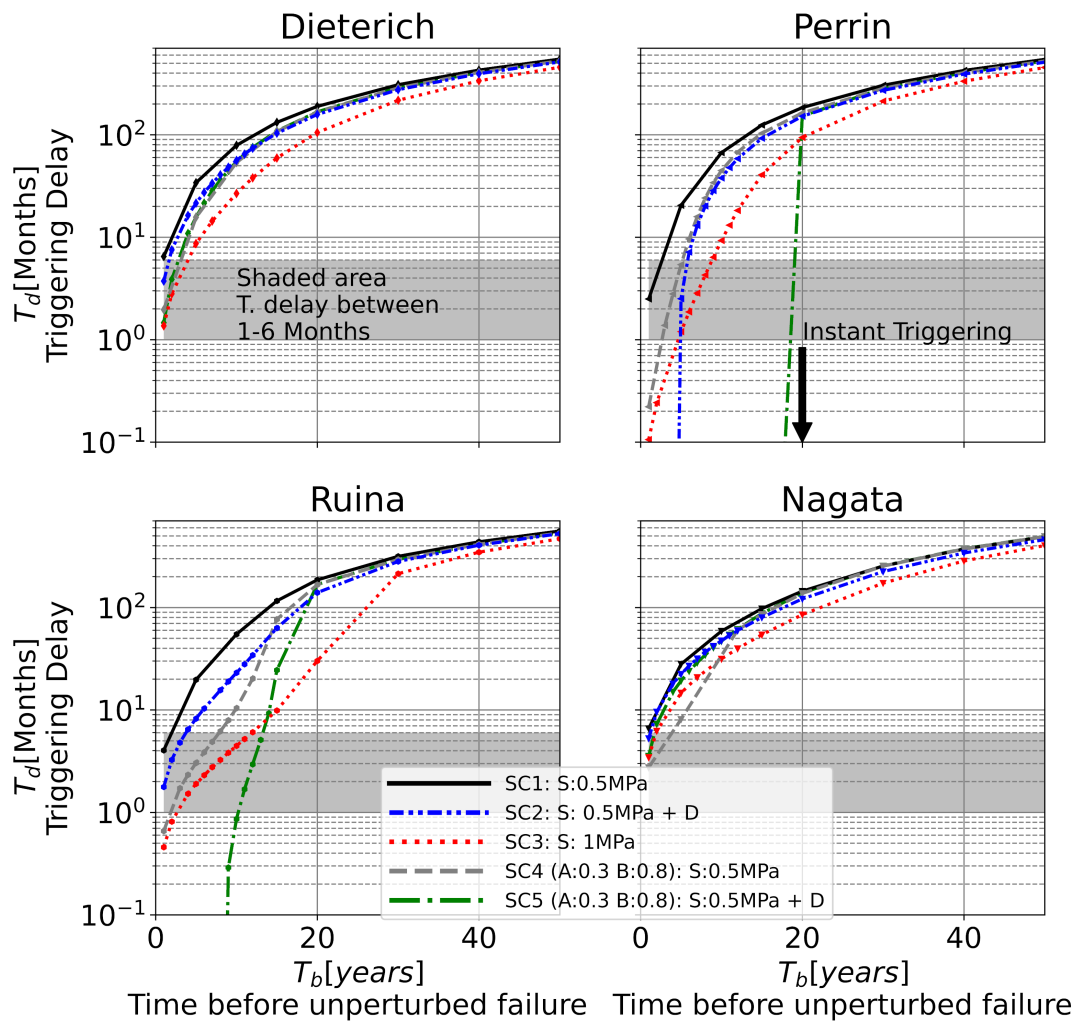


Figure 2.12: Simulation results of the Düzce triggering case: The x and y axes are time before unperturbed failure (years) and triggering delay (months). The results of each state evolution law are plotted as individual subplots. The five scenarios are applied for each law and plotted with different line types. The shaded region shows triggering delay between 1-6 months

In terms of Ridgecrest case scenarios (Case 2), the static stress change is fixed to

Table 2.3: Cases and Scenarios

Sc.ID	St.ID	$\Delta\tau$ [MPa]	$\Delta\sigma_n$ [MPa]	Description
1*	-	0.5	-	Static
2*	8101	0.5	-	Combined
3*	-	1	-	Static
4**	-	0.5	-	Static
5**	8101	0.5	-	Combined
1 ⁺	-	0.2	-	Static
2 ⁺	TOW2	0.2	-	Combined
3 ⁺	TOW2	0.2	-10	Combined - Normal Stress
4 ⁺⁺	-	0.2	-	Static
5 ⁺⁺	TOW2	0.2	-	Combined

CASE 1 (*) : G:30GPa, L:5km, V_{PL} :20mm/y, A:0.5MPa, B:1MPa, d_c :1mm, C:20
CASE 1 (**) : G:30GPa, L:5km, V_{PL} :20mm/y, A:0.3MPa, B:0.8MPa, d_c :1mm, C:20
CASE 2 (+) : G:40GPa, L:6km, V_{PL} :2mm/y, A:0.5MPa, B:0.7MPa, d_c :1mm, C:20
CASE 2 (++) : G:40GPa, L:6km, V_{PL} :2mm/y, A:0.1MPa, B:0.3MPa, d_c :1mm, C:20

0.2 MPa [79], [80], [81]. We also test a possible geothermal interaction by simply decreasing the effective normal stress $-10MPa$. The north channel of the TOW2 station is used as a transient triggering signal, whose PGV reaches $28cm/s$. According to the results shown in figure 2.13, neither a static triggering signal (Sc 1 and 4) nor a decrease in the effective normal stress (Sc:3) is sufficient to lead to a few days of triggering delay. We can reach a few days of triggering delay by decreasing a and including transient triggering (Sc:5). Among state evolution laws, only the Ruina law leads to a few days of triggering delay in Sc:5.

2.4.2 The transient triggering effects around the Ridgecrest

The transient triggering effects of the foreshock Mw6.4 are tested by extending the simulation to the surrounding region with using all possible stations. Since transient triggering effects can only be effective at the end of the seismic cycle, we assumed that there is 5 years left for the next rupture for all locations. The results are plotted

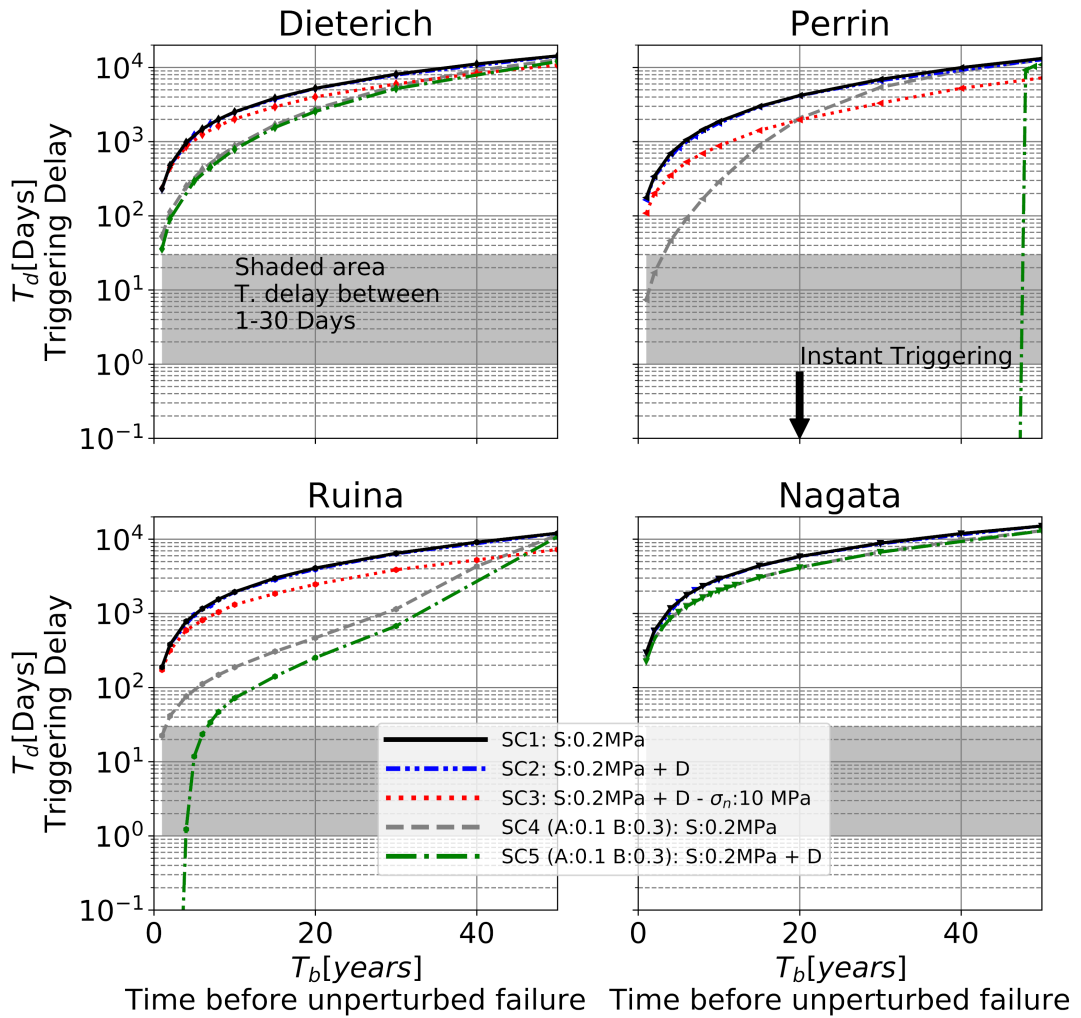


Figure 2.13: Simulation results of the Ridgecrest triggering case: The x and y axes are time before unperturbed failure (years) and triggering delay (days). The results of each state evolution law are plotted as individual subplots. The five scenarios are applied for each law and plotted with different line types. The shaded region shows a triggering delay between 1-30 days

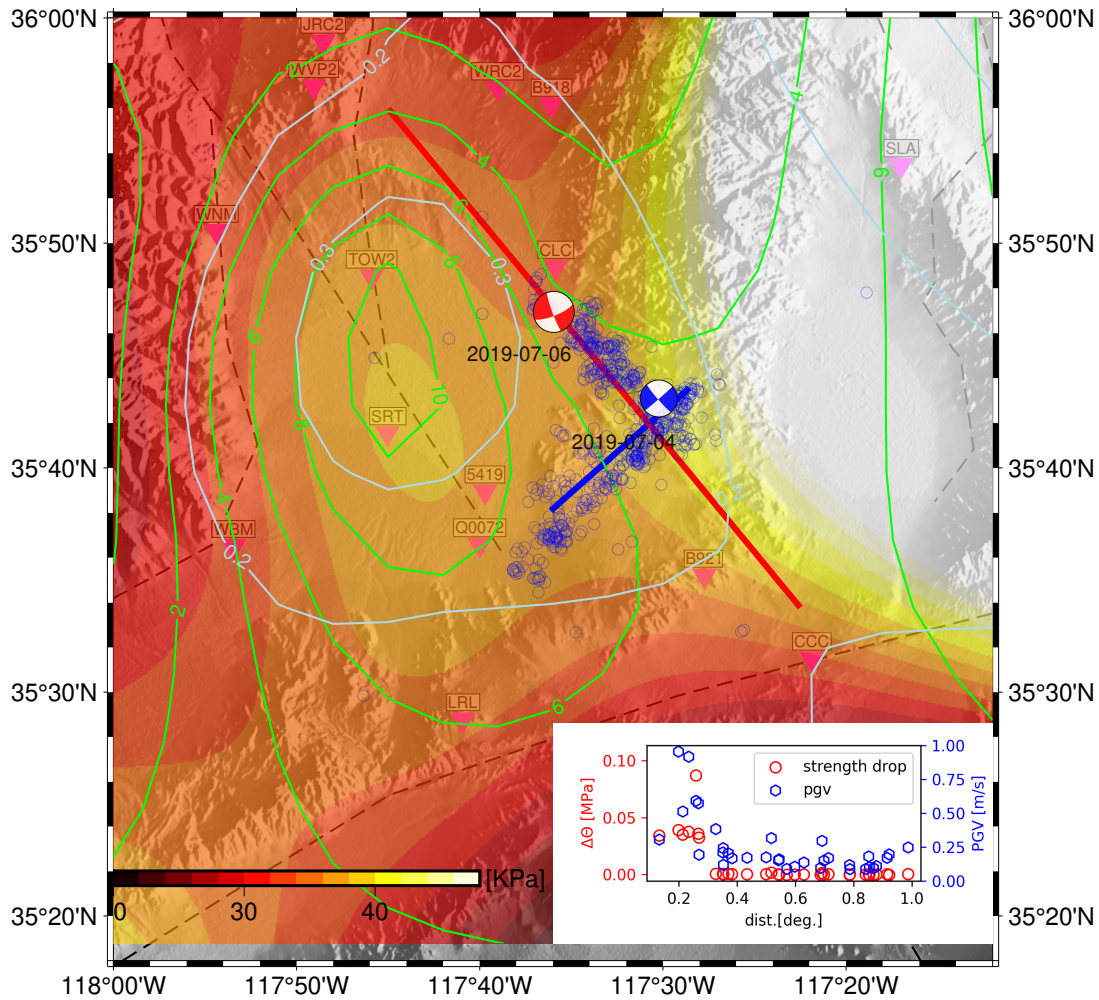


Figure 2.14: Simulation results of the Ridgecrest triggering case: The system with default parameters is simulated with the horizontal components of all available stations. The strength drops values are plotted with colors, given in the color bar. Peak ground velocities and peak ground frequencies are plotted as contours as green and light blue color. In the inset figure, the attenuation of dynamic effects and the PGV values are given.

in Figure 2.14. According to the Figure, the foreshock propagated uni-laterally to the southwest. Transient effects appear to be high at the basins, west and east sides of the ruptured fault. The transient effects are also high at the nucleation point of the M7.1 rupture (plotted with a red star), suggesting that the M7.1 rupture has also been affected by the transient triggering. The inset figure also shows that the dynamic effects attenuates very fast and beyond 0.3 degree.

2.5 DISCUSSION

The primary objective of this study is to identify the most significant features of the mechanism responsible for triggering large earthquakes, rather than to develop a comprehensive model of earthquake triggering. A single degree of freedom model is adopted for the following reasons. Firstly, since the focus is on large earthquake triggering, a model of a large asperity with a stiff fault mechanism that is capable of generating characteristic earthquakes will be more robust against background creeping or complex faulting processes. Secondly, the single degree of freedom model is computationally less expensive compared to continuum formulations, which allows for the exploration of a larger set of parameters and scenarios. Despite its simplicity, the single degree of freedom model has been shown to be in agreement with continuum formulations in terms of earthquake triggering, as demonstrated in previous studies [48, 49].

We begin by revisiting earlier studies on earthquake triggering using spring-slider models [46, 47]. We aim to expand these studies by incorporating all proposed state evolution formulations and evaluating them on a well-developed fault model. The triggering is tested after several numerical cycles to minimize numerical artifacts caused by initial values. The understanding of transient triggering is limited, and therefore, our numerical and analytical analyses concentrate on this aspect. Two real-case scenarios are also analyzed to support the sensitivity analyses and comparison of the state laws. By comparing the numerical results with real observations, we aim to examine the relationship between recurrence time, released stress, and triggering delay.

Our analytical and numerical sensitivity results for transient triggering are in good agreement. The analytical model demonstrates the strong dependence on the amplitude and frequency of an oscillatory transient wave train under specific conditions. The state laws differ in their ability to sustain these conditions, resulting in different conclusions. The state or strength of the locked patch's frictional interface gradually increases with slow loading until a minuscule amount of slip occurs. Once the accumulated slip exceeds a critical slip distance, the frictional state becomes so high that it can no longer heal, and any external perturbation can lead to a sudden increase in velocity and a drop in strength, as described by rate and state friction. Quantifying this weakening term provides insight into how a fault's strength changes in response to mechanical state changes. Due to differences in the critical condition and weakening rate, the results vary significantly, a fact that was not addressed in previous studies [1, 53, 47, 67, 48, 50, 51].

Observations suggest that there is a frequency threshold for the wave train's frequency and amplitude [75]. Our analytical and numerical results clearly show that longer velocity waves have higher triggering potential. However, previous studies using conceptual models have produced conflicting results. Some argue that higher frequency signals are more effective [1], while others claim that frequency is insignificant [50]. In [50], the Nagata-type friction law with $C = 20$ was applied. Our analytical results (Figures 2.3, 2.5) and numerical results (Figures 2.10, 2.9) show that the dynamic effects of the Nagata law flatten out as the stress-state coupling parameter increases. As this value increases, the results become independent of the transient signal's onset time, and a constant clock advance or strength change emerges. This result indicates an insensitivity to the triggering signal's frequency and suggests the difference in the state laws. On the other hand, [1] discussed the frequency dependence on slip and suggested that faster frequencies are more effective. In terms of slip rate perturbations, slower signals accumulate more slips, while faster signals neutralize themselves faster, leading to less effect. We find it more convenient to examine the frequency dependence in terms of velocity perturbation, and our results agree well with observations in nature [75]. Our conclusion is that the effect of transient triggering can be quantified using the peak ground velocity and frequency of the oscillating signal, which can be observed in nature. Further study is needed to explore the impli-

cations of our analytical model for transient triggering.

Finally, we tested Mw7.4 İzmit (07.08.1999)-Mw7.2 Düzce (12.11.1999) and Mw6.4 (04.07.2019) - Mw7.1 (06.07.2019) Ridgecrest earthquake sequences with various possible scenarios. For both cases, when the direct velocity effect parameters are small enough, the results show similar clock advances to what is observed in nature. In terms of comparing the state laws, many simulations using the Ruina state dependence can explain the observed failure time delays, while the Perrin law is too sensitive to triggering and results in instant triggering. The Dieterich and Nagata laws are unable to explain the cases unless the direct velocity effect parameter is less than the typical values of a , as reported in laboratory studies [33]. Based on the results of this study and considering the velocity step test performance from laboratory studies [36], we favor the Ruina law.

2.6 CONCLUSION

In this study, we revisit previous research on earthquake triggering by incorporating the Dieterich, Perrin, Ruina, and Nagata-type state evolution laws. Our findings suggest that the triggering of earthquakes depends on the weakening rate of each state formula in terms of rate and state friction. Our results demonstrate that the response of the state laws can differ, which may help explain the conflicting results observed in previous studies.

The agreement between our analytical and numerical results shows that the process of triggering is largely influenced by the asperity patch size, direct velocity effect parameter, and effective normal stress, while the other fault parameters have less impact. Additionally, our results highlight the significance of peak ground velocities and frequency in determining an earthquake's triggering potential. Our analytical formulation provides a comprehensive understanding of the triggering mechanism under specific conditions. However, further validation with real data is necessary to confirm these findings.

Finally, our simulations of real-case scenarios indicate that the Ruina law provides the best results, outperforming the other state evolution laws in explaining the observed

failure time delays.

CHAPTER 3

IMPACT OF 2019 MW 5.8 MARMARA SEA EARTHQUAKE ON THE SEISMIC CYCLE OF LOCKED NORTH ANATOLIAN FAULT SEGMENT

The Mw5.8 earthquake in the Marmara Sea west of the locked segment of the North Anatolian Fault sparked a debate on whether this event may trigger or advance the expected large ($M_w > 7$) earthquake close to Istanbul in time. Its potential effect on the major earthquake cycle is analyzed using rate-and-state friction (RSF) dependent spring-slider models by considering miscellaneous views of friction and different simulation strategies. Dynamic and static effects are simulated using recorded seismic waveforms and computed static stress change. This chapter has been submitted to Tectonophysics and reviewed on 2th of February 2023. The codes are available at GitHub and zenodo [59]. We only make minor changes to fit the text appropriately in the context of this thesis.

3.1 Introduction

On 26 October 2019, an Mw5.8 earthquake occurred on a secondary fault connecting to the locked Kumburgaz fault segment of the Main Marmara Fault (MMF) [2] (Figure 1). This moderate earthquake heated a debate about triggering a possible large earthquake, which may cause devastating casualties to the metropolitan city İstanbul in Turkey, whose epicenter is approximately 10 kilometers south of the city's shore.

The MMF lies on the western edge of the North Anatolian Fault (NAF). All major segments of NAF have been ruptured with ($M_w > 7$) since the 20th century except for the MMF, with a synchronously west migrating pattern [55]. Thus, considering the earthquake records along NAF and accumulated slip deficit, evaluating the trig-

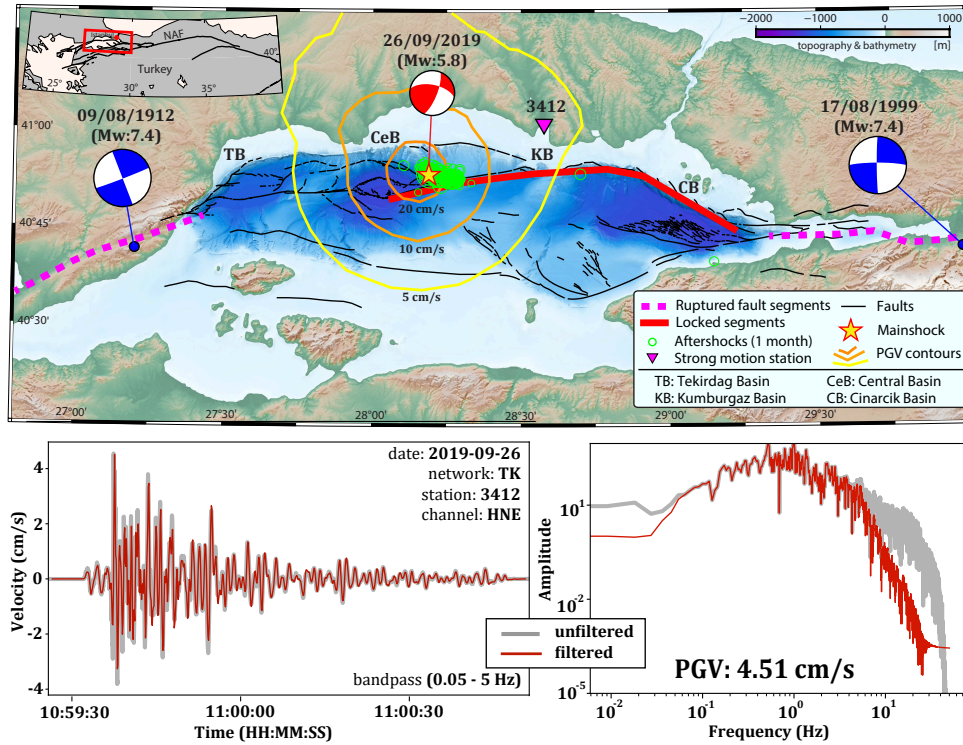


Figure 3.1: The map shows the moderate (Mw:5.8) earthquake, its mechanism and aftershocks [2], and primary/secondary faults along the Main Marmara Fault (MMF) of NAF [3, 4] and mechanism of earthquakes on the adjacent segments with their surface ruptures [5, 6]. The contour lines show the peak ground velocity values estimated after the main shock by USGS (<https://earthquake.usgs.gov/earthquakes/eventpage/us700051kl/map>). The Eastern component of the waveform recorded by the strong motion station TK-3412 (location is shown on the map with the inverted triangle) is plotted below with its spectral amplitudes, which is used as the dynamic triggering signal in the simulations.

gering potential of the moderate earthquake on the locked fault segment is of great importance.

Observational evidence shows that earthquakes can trigger other earthquakes through permanent stress changes, the passage of transient waves, or both simultaneously [39, 64]. Traditionally, the Coulomb stress failure criterion relates the earthquake-caused dislocation to the static stress change and hypothesizes that the positive static stress changes on a receiver fault shorten the failure time [37, 65]. However, in some cases, earthquakes can be triggered with a time delay after seismic waves pass, even if Coulomb's stress is negative [63] or static stress transfer to the triggered events is negligible [39]. Those events are examples of dynamically triggered events that Coulomb fails to demonstrate.

The more realistic way to quantify full earthquake triggering (static and dynamic triggering) is the laboratory-based full constitutive laws called rate-and-state friction (RSF) [29, 30, 58, 32]. Unlike Coulomb's criteria, RSF does not depend on a simple stress threshold, but the frictional resistance is a function of slip rate and a state variable. These empirical laws show many aspects of observed fault properties from pre-seismic slip and nucleation to co-seismic rupture and earthquake after-slip ([33] and references therein).

Using RSF dependent friction, simple spring slider models [1, 47], higher dimensional continuum formulations [48, 49, 50, 82], and laboratory experiments [41, 52] reported roles of static and transient signals on failure time changes, sensitive parameters and implications on nature. However, even if the state laws generate similar results at some level, they differ substantially for certain parameters or external perturbations [36, 54, 83], which should be considered while applying.

Here, we consider the locked patch of MMF (Kumburgaz fault segment) velocity weakening (VW) friction within the framework of RSF on conceptual spring slider models. The static stress increases calculated by conventional Coulomb's law, and seismic waves generated by the moderate earthquake are inserted into the running spring-slider models in a specific onset time, and changes in the large earthquake's failure time are observed. The Mw5.8 moderate earthquake's triggering potential to the pending large earthquake is quantified with different scenarios. Firstly, we con-

sider different state evolution formulas [29, 30, 58, 32] on quasi-static-full-dynamic [84] and quasi-dynamic [85] simulation strategies with single degree freedom spring slider systems. Hence we conduct numerical tests to investigate the inference of numerical methods and state evolution within the framework of rate and state friction without including complexity. Then, we included the expected rheological change with depth by defining a brittle-ductile transition zone with velocity-strengthening (VS) friction and a ductile zone (DZ) with viscous flow below. By defining different degrees of coupling between brittle and ductile deformations and including variable asperity size and shear-normal stress coupling, we investigated the possible effects of fault complexity on the seismic cycle of the locked fault. The results of various simulations using conceptual models provide the moderate earthquake's upper-bound effects which can vary significantly from models using a constant stressing rate and failure threshold, like the Coulomb failure criteria. Moreover, the simulation results offer a complete comparison among the state laws implying similarities and differences depending on the state evolution and numerical strategies.

3.2 Data and Methodology

3.2.1 Data

[2] inverted the finite fault model and estimated Coulomb stress changes near the central base of MMF. The locked Kumburgaz segment of MMF is only several kilometers away (<3 km) from the main shock. Their results indicate a deep slip and a stress increase along the Kumburgaz Fault, which is around 1 bar (0.1MPa) at the 10 km depth. Among the strong motion stations of the Disaster and Emergency Management Presidency of Turkey (AFAD), the maximum PGV (4.51cm/s) is recorded in the east component of TK-3412 located on the southern shore of İstanbul near Büyükçekmece which is 35 km away from the main-shock (Figure 1). The waveforms are publicly available at <https://tadas.afad.gov.tr/>. After trend removal, we use this waveform as the dynamic triggering signal and apply a Butterworth filter at (0.05, 5)Hz to remove noise and possible tilts.

3.2.2 Methodology

A homogeneous VW patch is considered the nucleation point of the pending large Marmara Earthquake and the dynamic equation of motion of the nucleation point is given in equation 3.1 and illustrated in Figure 3.2.

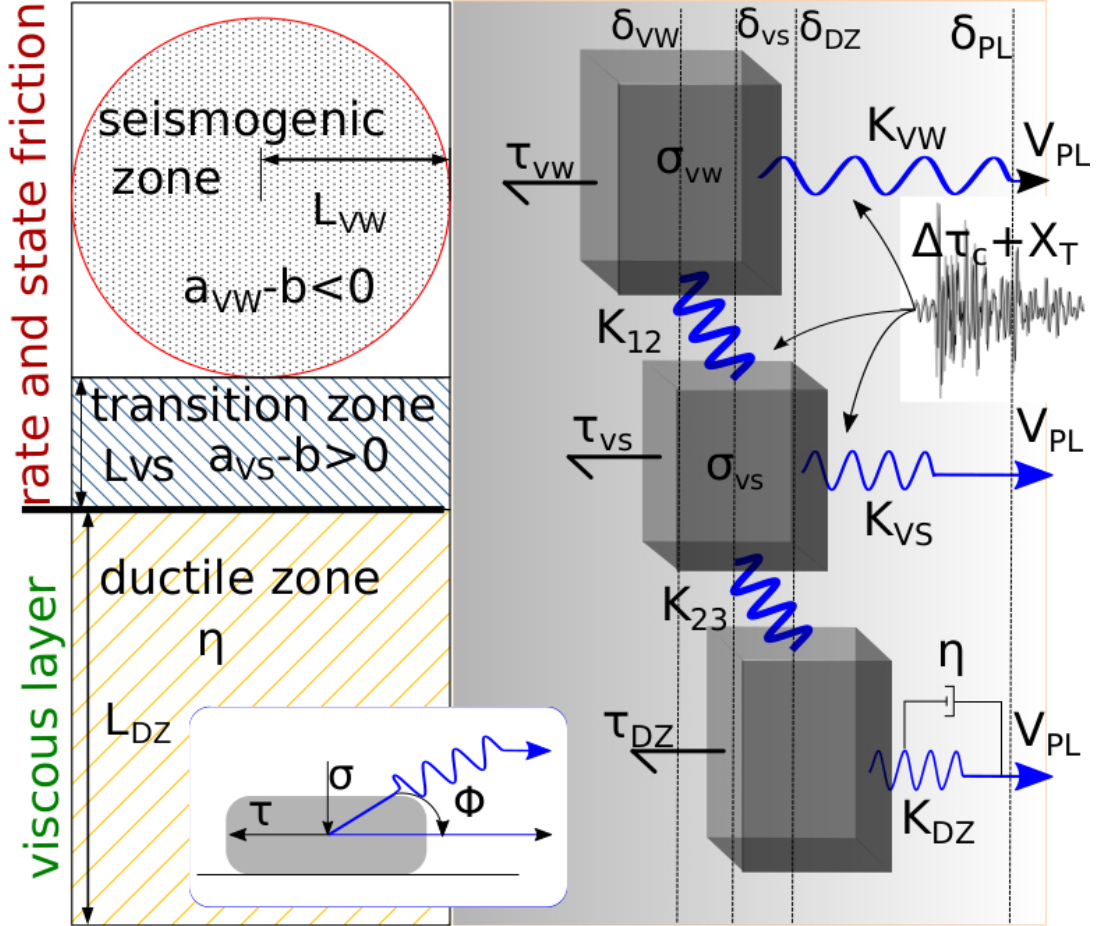


Figure 3.2: The conceptual model used in this study consists of three fault zone, including a velocity-weakening friction circular asperity that is the nucleation point of the next large earthquake, a velocity-strengthening brittle-to-creep transition zone, and a deep ductile zone. Plate velocity is assumed to be constant and moderate earthquake is inserted into the fault system externally.

$$m\ddot{\delta}_{vw} = \tau_{vw}^{(e)} + \Delta\tau_c H(t, t_p) - \tau_{vw} \quad (3.1)$$

On the left side of the equation, m and $\ddot{\delta}$ denote the VW patch's inertia effect and

acceleration, respectively. The approximation of the full inertia effect or the mass is $m = K_{vw}(T/2\pi)^2$, where T is vibration period [86], and K_{vw} is the spring stiffness approximated with the ratio between the shear modulus and a half-length of the VW patch $K_{vw} = \Gamma G/L_{vw}$. The shape of the locked patch is highly ambiguous. Thus, we assume it as a circular asperity patch for simplicity, which sets the scale between elastic properties and a circular asperity shape to $\Gamma \approx 1$ according to [76].

On the right side of equation 3.1, $\tau_{vw}^{(e)}$ denotes the elastic traction computed from the following equation.

$$\tau_{vw}^{(e)} = K_{vw}(\delta_{PL} + X_T(t, t_p) - \delta_{vw}) + K_{12}(\delta_{vs} + X_T(t, t_p) - \delta_{vw}) \quad (3.2)$$

Similarly, K_{12} is the elastic stiffness between the seismogenic (VW) and transition (VS) zones, formulated as $c_d(K_{vw} + K_{vs})/2$, where c_d defines the elastic stress relation controlling the coupling degree which is similar to [87]. δ_{PL} is the average slip accommodated by the fault zone, and $X_T(t, t_p)$ and $\Delta\tau_C H(t, t_p)$ denote the dynamic triggering signal that temporarily changes the loading slip and static stress change computed by Coulomb's failure model [37], that enter to equation 3.1 with a simple Heaviside function $H(t, t_p)$ on the onset time t_p . The last term τ_{vw} defines the frictional resistance, calculated by the Rate-and-State friction (RSF),

$$\tau_{vw} = \sigma_{vw}\mu_{vw} = \sigma_{vw}(\mu_0 + a_{vw} \ln(V_{vw}/V_0) + \Theta) \quad (3.3)$$

where $\sigma = P - \tau \tan \phi$ is the normal stress formulation defined by the change from the normal stress P at $\tau = 0$ with an angle ϕ accounting for slips on non-planar and non-vertical faults [88], an illustration is shown in the inset in Figure 3.2. μ_0 is the steady state friction at the reference velocity V_0 . a_{vw} parameter is the empirical RSF parameter that scales the frictional resistance depending on the velocity change, the so-called direct velocity effect. $V_{vw} = \dot{\delta}_{vw}$ is the velocity variable of the interface. The last term Θ is called the state variable, defining the interface strength and whose time-dependent evolution can be computed by one of the following formulas.

$$\dot{\Theta}^{(d)} = \frac{b}{d_c/V_0} \exp\left(\frac{-\Theta}{b}\right) - \frac{b}{d_c} - \alpha \frac{\dot{\sigma}}{\sigma} \quad (3.4)$$

$$\dot{\Theta}^{(r)} = -\frac{V}{d_c}(\Theta + b \ln(\frac{V}{V_0})) - \alpha \frac{\dot{\sigma}}{\sigma} \quad (3.5)$$

$$\dot{\Theta}^{(p)} = \frac{b}{2d_c/V_0} \exp(\frac{-\Theta}{b}) - \frac{bV^2}{2d_cV_0} \exp(\frac{\Theta}{b}) - \alpha \frac{\dot{\sigma}}{\sigma} \quad (3.6)$$

$$\dot{\Theta}^{(n)} = \frac{b}{d_c/V_0} \exp(\frac{-\Theta}{b}) - \frac{b}{d_c}V - c\dot{\tau} - \alpha \frac{\dot{\sigma}}{\sigma} \quad (3.7)$$

In equations (3.4-3.7), b and d_c denote empirical state effect parameter and critical slip distance. c is the stress weakening effect parameter, available only for the Nagata law. α is the shear-normal stress coupling parameter [88]. The super-scripts (d) , (r) , (p) , (n) denote Dieterich, Ruina, Perrin, and Nagata state evolution laws, abbreviated with the first authors of the studies [29, 30, 58, 32], and hereafter we refer them so for simplicity. We prefer the large state notation $\Theta = b \ln(\frac{\theta}{d_c/V_0})$ rather than their original (θ) notation because it is more convenient to quantify interface or frictional strength decrease $(\mu_0 + \Theta)$ as the triggering signals are applied [36]. Dieterich, Ruina, and Perrin laws use the same constitutive parameters (a, b, d_c) ; however, [32] claimed that the a direct velocity effect parameter was estimated several orders lower in the previous studies and proposed a revised state law called Nagata. [89] found later the identical relation between the parameters of Nagata and the rest, by following relations.

$$\frac{a^{(n)}}{c+1} = a, \quad d_c^{(n)}(c+1) = d_c, \quad (a-b)^{(n)} = (a-b) \quad (3.8)$$

The VS transition zone is assumed to slide steadily, so the VS zone's force balance can be defined with the following relations.

$$\tau_{vs} = \sigma_{vs}(\mu_0 + (a_{vs} - b) \ln(V_{vs}/V_0)) \quad (3.9)$$

$$\tau_{vs}^{(e)} =$$

$$K_{vs}(\delta_{PL} + X_T - \delta_{vs}) + K_{12}(V_{vw} + X_T - V_{vs}) + K_{23}(V_{dz} - V_{vs}) + \Delta\tau_C H \quad (3.10)$$

K_{12} and K_{23} are the elastic stiffness between VW-VS and VS-DZ. We assumed the triggering signal's amplitude and transient signal's frequency and phase do not differ from the VW zone and are applied identically to VS zone. The force balance for the DZ can be written as.

$$\tau_{dz} = \eta V_{dz} \quad (3.11)$$

$$\tau_{dz}^{(e)} = K_{dz}(\delta_{PL} + X_T - \delta_{dz}) + K_{23}(V_{vs} - V_{dz}) \quad (3.12)$$

where the viscosity parameter $\eta = \nu/L_{dz}$ is approximated by the ratio between the viscosity and the size of the DZ [90]. Full numerical simulations can run using the equation 3.1. However, [86] suggested that having two distinct slow and fast regimes causes numerical difficulties. Therefore, instead of directly solving 3.1, a quasi-static approximation is applied by ignoring the left-hand side in equation 3.1 if slip velocities are lower than a certain velocity threshold ($V < V_c = 0.01m$) and the solver switches back to full dynamic approximations otherwise.

The triggering signals are applied when the seismic cycle is at the slow phase ($V \approx 0$). In the quasi-static approximation ($m\ddot{\delta}_{vw} = 0$), a possible inertial influence during triggering is ignored. Therefore, we also apply the same triggering scenarios using quasi-dynamic (QD) approximation [85], which is given by,

$$\tau_{vw}^{(qd)} = \tau_{vw}^{(e)} + \Delta\tau_C H + G \frac{V_{vw}}{2c_s}. \quad (3.13)$$

The last term on the right side is the radiation damping to sustain a solution when velocity reaches high values, and c_s is the shear wave speed. We explicitly solved FD and QD for the VW and VS, and DZ zones from the following formulations.

$$\dot{V}_{vw}^{(fd)} = \frac{\tau_{vw}^{(e)} - \tau_{vw}}{m} \quad (3.14)$$

$$\dot{V}_{vw}^{(qs)} = \frac{\dot{\tau}_{vw}^{(e)} - \sigma_{vw}\dot{\Theta} - \dot{\sigma}_{vw}\mu_{vw}}{a\sigma_{vw}/V_{vw}} \quad (3.15)$$

$$\dot{V}_{vw}^{(qd)} = \frac{\dot{\tau}_{vw}^{(e)} - \sigma_{vw}\dot{\Theta} - \dot{\sigma}_{vw}\mu_{vw}}{\frac{a\sigma_{vw}}{V_{vw}} + \frac{G}{2c_s}} \quad (3.16)$$

$$\dot{V}_{vs} = \frac{\dot{\tau}_{vs}^{(e)}}{a_{vs}\sigma_{vs}/V_{vs}} \quad (3.17)$$

$$\dot{V}_{dz} = \frac{\dot{\tau}_{dz}^{(e)}}{\eta} \quad (3.18)$$

Note that in equations 3.2, 3.10 and 3.12, the dynamic triggering turns to velocity waveforms \dot{X} . Similarly, the Heaviside function for adding the Coulomb's static stress increase is set to a Gauss shape, computed with the following equation.

$$S(t, t_p, \Delta\tau_C) = \frac{\Delta\tau_C}{(2\pi)^{0.5}} \exp(-0.5(t - t_p - 3)^2) \quad (3.19)$$

Also, we use analytical relation to calculate velocity variable using the QS approach by simply rephrasing equation 3.3 as below similar to [1].

$$V_{VW} = V_0 \exp\left(\frac{\frac{\tau_{VW}}{\sigma_{VW}} - \mu_0 - \Theta}{a}\right) \quad (3.20)$$

To sum up the numerical methods, in the quasi-static phase ($V_{vw} < V_c$), we calculate V_{vw} using equation 3.15; otherwise, equation 3.14 is used as a first simulation strategy, which we call quasi-static-full-dynamic (FD). As an alternative to quantifying the possible inertia effect on the results, the quasi-dynamic (QD) strategy is adapted using equation 3.16. To complete explicit formulation, one of the state equations 3.4-3.7 and equations 3.17 and 3.18 are applied, regardless of the simulation strategy. We also considered the single-degree freedom spring slider model by excluding the VS and DZ zones for simplicity, investigating the influence of state evolution and numerical strategies. We use the Runge-Kutta-Cash-Karp adaptive step size method to solve sets of ordinary differential equations [91].

3.2.3 Simulation Set-up

The frictional constitutive parameters beneath the Marmara Sea are highly unknown. Therefore we adapt the parameters previously used by [1, 47], which agree with the laboratory studies, for VW friction. Among them, only the direct velocity effect parameter a_{vw} is sensitive to velocity changes [92]. Thus, we use two sets for a_{vw} keeping the rest constant, given in Table 3.1. Other physical and geometrical parameters of the locked Kumburgaz segment are adapted from studies given in Table 1.

Table 3.1: Simulation Parameters

Parameter	Value	Description	Reference
L_{vw}	1,2,5,10km	Asperity radius	[93]
L_{vs}	5km	Transition zone size	
L_{dz}	30km	Ductile zone size	
c_d	0.05,0.1,1,2	Coupling degree	[87]
σ_{vw}	100MPa	Effect. normal stress	[94]
σ_{vs}	150MPa	Effect. normal stress	[94]
ϕ_{vw}	[-10,...,+10] (deg)	Reverse dip angle	
ϕ_{vs}	[-10,...,+10] (deg)	"	
ν	10^{18} Pa s	Viscosity	[90]
$\dot{\delta}_{PL}$	20mm/yr	Plate velocity	[95]
a_{vw}	0.005-0.001	Direct vel. effect	[1]
b	a+0.005	State evol. effect	"
d_c	1 mm	Crit. slip dist.	"
$a_{vs} - b$	0.001,0.005	VS friction	"
c	20	Stress-weakening par.	[89]
$\Delta\tau_C$	0.1MPa	Coulomb static stress	[2]
$\dot{X}(t)$	waveform \times [2, 5, 10]	Dynamic trig. signal	

$G=30\text{GPa}$, $c_s=3\text{km/s}$, $T=5\text{s}$, $V_c=1\text{cm/s}$, $\mu_0=0.6$, $a_{vs} - b=a_{vw}$, $\alpha=0.5$

Recently, off-shore geodetic observations revealed that the Kumburgaz segment of MMF is storing stress and, thus, locked [95]. Considering the latest rupture in 1766 [55], having an average recurrence time of 250yr, and the cumulative slip deficit exceeding $4m$, the next $Mw > 7$ earthquake may rupture soon at the segment. Earthquake triggering depends non-linearly on time[65]; we insert the triggering signals in a specific onset time that depends on the latest rupture time. We run the simulation that covers several cycles until the recurrence time change becomes negligible to eliminate any artificial effects due to the initial values. Then, the simulation is initiated from the last seismic cycle for various triggering onset times. Hence, we observe the time perturbation within the last cycle in reference to the un-perturbed case, which we call failure time advance or clock-advance.

First, we run simulations using the FD approximation for each of the four RSF state evolution laws with the parameters in Table 1 using the single-degree model to avoid any complexity. We build two fault set-ups by changing the a_{vw} parameter, with similar recurrence times but different triggering sensitivity. Since we assume the Kumburgaz fault segment is at the end of its seismic cycle, we define the onset time for triggering signals before the upcoming failure time ascends from near zero to 50 years. Considering the ambiguity related to the location of the locked section, the waveform is scaled by multiplying $\times 2$, $\times 5$, and $\times 10$. Note that the PGV of the waveform multiplied by $\times 5$ agrees with USGS's PGV map (Figure 1). Hence, we plot the induced failure time advance versus T_b for each set and state law. Next, the same scenarios are applied with QD approximation to test any effect caused by numerical strategies. Finally, we run the simulations by including transition and ductile zones and shear normal stress coupling relations to account for possible fault zone complexities.

3.3 Simulation Results

3.3.1 State Laws

Figure 3.3 displays the simulation results for different state laws on single-degree freedom models. None of the state laws induce instant triggering for this event. Nev-

ertheless, there is a visible failure time advance depending on the onset time of the triggering signals, mainly caused by the static stress increase. All state laws agree with Coulomb's failure model (the model has a $0.12\text{MPa}/\text{yr}$ stressing rate; thus, 0.1MPa stress increase corresponds to 0.83 years of Coulomb's clock advance) if the time before failure $t_b > 20$ years. Otherwise, they deviate from Coulomb's failure, before which ($t_b < 20$ years) the fault becomes sensitive to dynamic triggering and the state evolution, particularly its weakening rate. Moreover, using only dynamic triggering, Figure 3.3 demonstrates a few days to weeks of failure time advance, which is several orders lower than the static triggering (≈ 0.83 years).

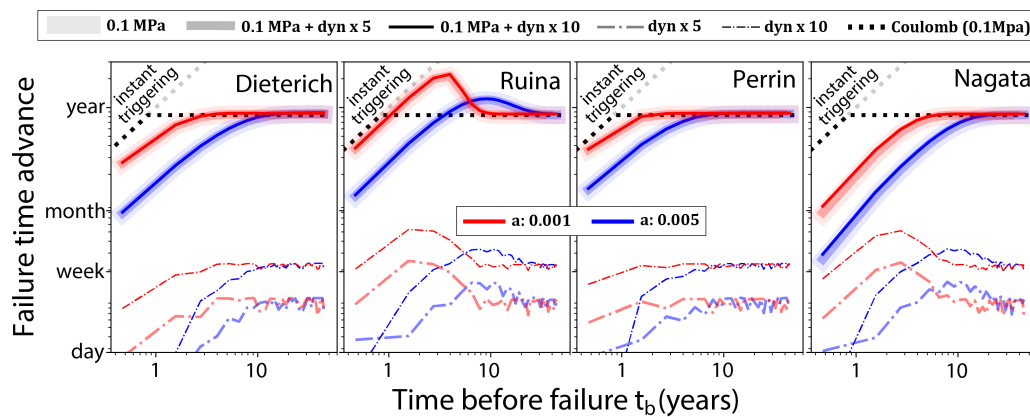


Figure 3.3: The induced failure time advance (vertical) versus triggering time before failure t_b in years (horizontal). Subplots show triggering simulation results of different state laws. Each scenario is plotted with a different line width, type, transparency, and color, as shown in the legend. If applied, static stress is 0.1MPa , and dyn in the legend denotes the dynamic triggering signal multiplied by $\times 5$ and $\times 10$ in the relevant scenarios.

The induced failure-time change curves of Dieterich, Perrin, and Nagata are quite similar for the applied triggering signals. Unlike others, Ruina law shows a large noticeable failure time advance for lower t_b values ($t_b < 20$ years). Otherwise, it closely resembles Coulomb's failure. Nagata law amplifies the dynamic triggering due to its additional stress weakening term, but in the meantime, scaling of the a_{vw} parameter increases the resistance to the velocity change; as a result, it exhibits the least clock advance for full triggering scenarios.

3.3.2 Simulation Strategy

According to our simulation, seismic cycles produced by FD and QD are quite different. Both recurrence time and stress drops of the FD are almost twice that of QD (Figure 3.4). Moreover, the Dieterich and Ruina law's state and velocity evolution patterns are also considerably different. Dieterich's velocity values approximately sustain a truly stationary contact ($v \approx 0$), while Ruina's velocity values are several orders higher. State variables' extreme values are more or less similar, but Dieterich's state evolution reaches higher values right after the slip, while Ruina heals slower in return.

Triggering simulations of FD and QD exhibited similar results even though their natural (un-triggered) recurrence times are distinct. This result implies that the damping term has a negligible effect on the triggering. Hence, the obtained failure time advances are rather robust and independent of simulation strategies.

3.3.3 Fault Complexity

Previous analyses were on the single-degree model, and lack depth-dependent complexity, which assumes the VW asperity exists within a constant creeping rate with the plate's slip rate V_{PL} and constant effective normal stress. Here we added a transition layer with VS friction and a ductile layer beneath, allowing a deep relaxation slip. Moreover, we included the effects of clamping due to normal stress variations to explore fault complexities further.

First, we investigated the recurrence times of the complex conceptual fault model with varying the coupling degree parameter allowing depth-dependent stress interaction and the effects of shear-normal stress coupling. Figure 3.5 displays that the recurrence times for weak and moderate coupling are close to the single-degree homogeneous model. On the other hand, highly coupled cases ($c_d=1$ and 2) shorten the seismic cycle, possibly limiting the characteristic earthquake magnitude and displaying an afterslip in the transition zone extending even to the ductile zone. The negative ϕ angle increases the normal stress in the same direction as shear stress, leading to a

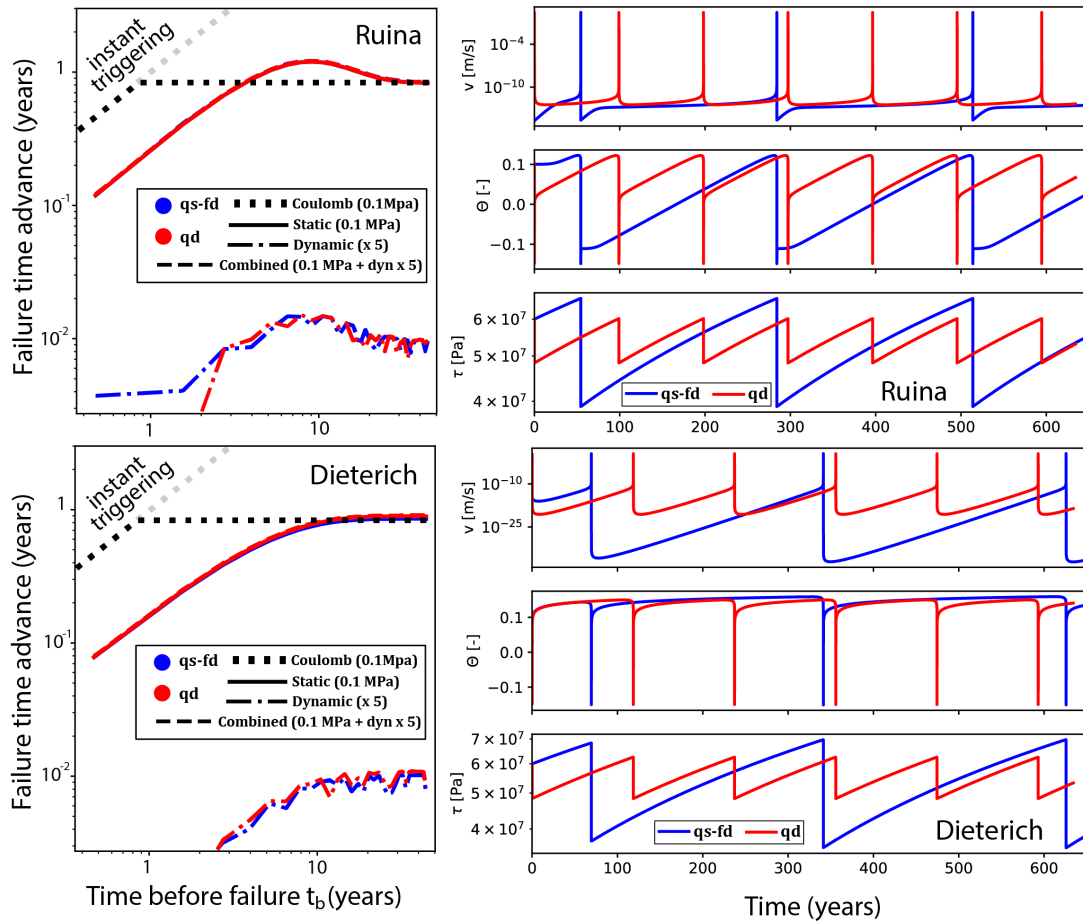


Figure 3.4: The figure compares quasi-static-full-dynamic (FD), and quasi-dynamic (QD) approaches. On the right, velocity v , state Θ and stress τ time series of unperturbed cycles for Ruina (on top) and Dieterich (below) are plotted for FD (blue) and QD (red). On the left, plots of induced failure time advance vs. triggering onset time before failure are shown separately for different scenarios, as given in the legend.

longer recurrence. In contrast, the fault with a positive ϕ angle leads to smaller slips and recurrence time.

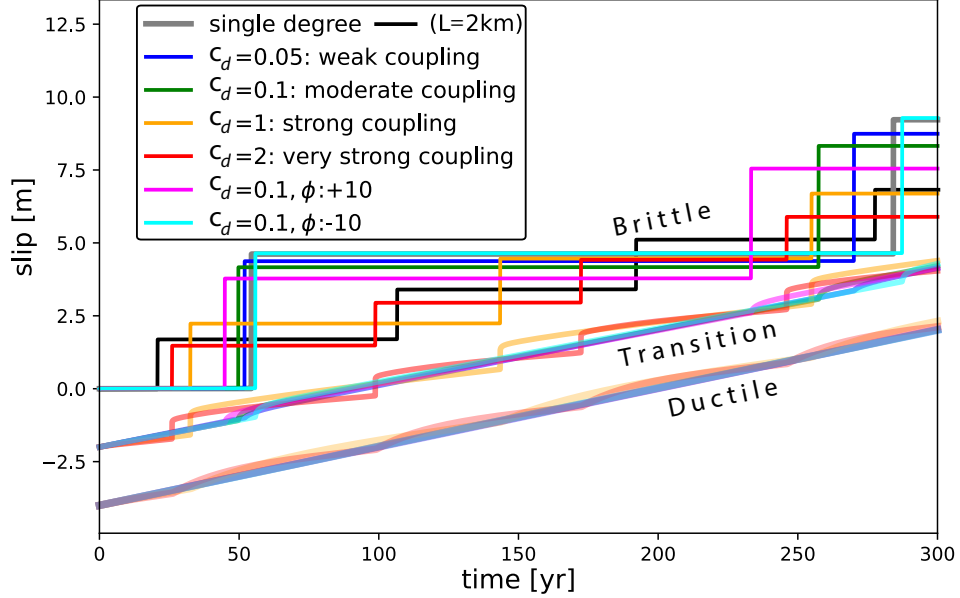


Figure 3.5: The effects of depth-dependent complexity with varying stress coupling control parameter c_d , and ϕ angle on the recurrence time are plotted. The horizontal and vertical axes are the time and slip, and colors are defined in the legend. The Ruina law is applied with the FD simulation strategy for $a_{vw} = 0.005$. Note that to sustain better visualization, transition and ductile zones are shifted.

Recent studies suggest the Kumburgaz fault is locked and has been loading stress [95]. However, the locations of stress loading and fault segmentation are highly ambiguous. Therefore, we also investigated the triggering effects for various asperity size that, in part, correlates with recurrence interval and, thus, upcoming earthquake's magnitude.

Figure 3.6 displays distinct responses depending on the onset time. The dynamic clock advances occur mainly when the onset time is less than 5% of the recurrence interval; otherwise, they are static like Coulomb failure. None showed instant triggering but resulted in normalized peak clock advances when fault failure is close

(1-3%). If fault failure is imminent ($<1\%$), normalized clock advances become similar regardless of asperity size or coupling degree, if not reduced asperity size and stronger coupling increase the clock advances (Figure 3.6).

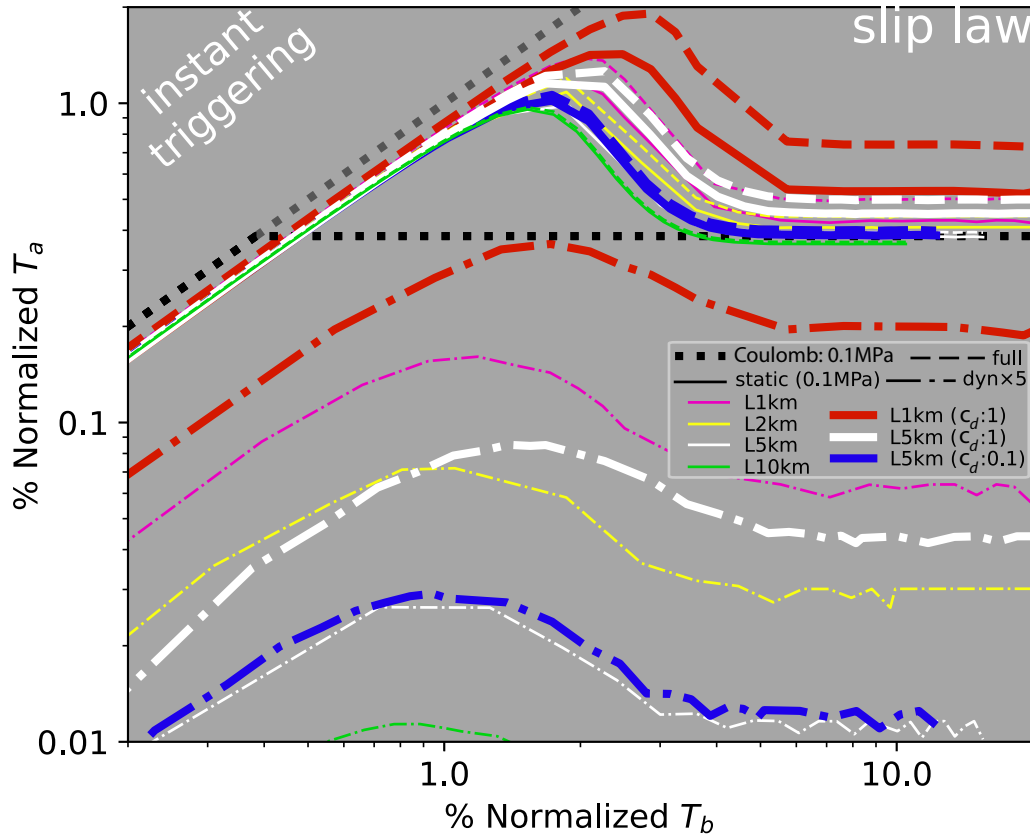


Figure 3.6: Figure shows how the VW asperity size and the stress coupling affect the of fault's sensitivity. The horizontal and vertical axes are the onset time of the triggering signal before its failure and the induced clock advances in normalized percentage. Dynamic, static and full (static and dynamic simultaneously) triggering signals are applied with size (asperity half length L_{vw}) and control coupling c_d parameter, defined in the legend. The Ruina law is applied with the FD simulation strategy for $a_{vw} = 0.001$.

Especially strongly coupled cases, including deeper relaxation slips that modify the stressing rate due to dynamic oscillation, lead to the largest clock advances and differ from conventional Coulomb failure predictions even though the failure is not expected soon. In this respect, our results indicate that the long-term static clock advance

produced by a nearby earthquake may be well over the predictions of Coulomb law that neglects temporal increase in the stressing rate (Figure 3.6).

On the other hand, Figure 3.7 displays that the inclusion of ϕ angle leads to minor differences from the single-degree model. The negative $\phi < 0$ angles lead to the same sign of shear and normal stress change, it causes a clamping type of effect on the fault patch, which displays a shorter clock advance (Figure 3.7). The positive values of $\phi > 0$ ease the effective normal stress on the locked interface, and the clock advance increases. However, in comparison to the effect of strong coupling, the inclusion of shear-normal stress with ϕ angle and additional α parameter on the state evolution (equations 3.4- 3.7) have a minor effect on the clock advance (Figure 3.7)

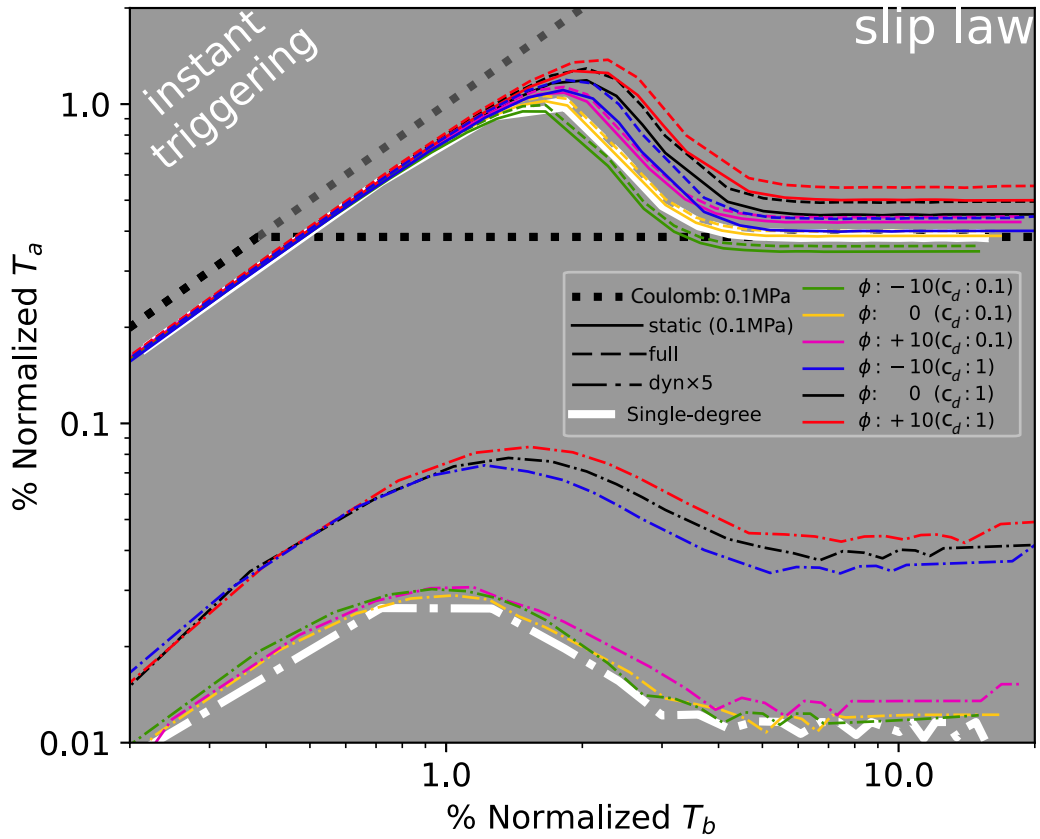


Figure 3.7: Figure shows how ϕ angle between the stressing direction and fault interface affect the triggering. The horizontal and vertical axes are the onset time of the triggering signal before its failure and the induced clock advances in normalized percentage. The Ruina law is applied with the FD simulation strategy for $a_{vw} = 0.001$.

3.4 Discussion and Conclusion

$M_w > 7$ characteristic earthquakes on the 1500 km long NAF have been migrating from the Eastern end towards the Marmara Sea since 1939. Therefore identifying fault segments of the Main Marmara Fault (MMF), their kinematics, initial stress state, rock properties, and faulting mechanisms has been of great importance [3]. The frictional behavior of the Kumburgaz fault segment in both lateral and vertical directions is highly ambiguous, mainly due to its undersea location [96, 95]. A suspicious seismic gap over the Kumburgaz fault segment on MMF was previously accounted for a creeping motion [97]. More recent observations agree that the Kumburgaz fault segment within the MMF is locked, forming a seismic gap and will likely break soon with a pending $M_w > 7$ earthquake [95, 98, 96, 95]. In addition, observations suggest creeping areas often surround locked fault patches [27]. The moderate $M_w 5.8$ earthquake ruptured along a secondary fault connecting to the Kumburgaz segment, changing the stress level in the vicinity [2]. In such cases, earthquake triggering including, including both instant and delayed, have been observed in different earthquake sequences such as Ridgecrest [99, 71], İzmit-Düzce [92], Denali [100].

Since a strong consensus has been established on the locked behavior of the Kumburgaz segment, we conceptually assume a homogeneous circular fully-locked patch that is the nest of a future large earthquake with velocity-weakening friction. We allowed the conceptual model with velocity-strengthening friction beneath and a viscous flow in down-dip to account for brittle-ductile coupling, including slower relaxation that may be higher than the plate velocity with external perturbations. We trigger the springs that account for the elastic stress accumulation with the moderate $M_w 5.8$ earthquake's static and transient signals and observed system responses. Since the location of the velocity-weakening patch is highly unknown, we scale the observed waveform corresponding to the PGV values in map 3.1. If the locked patch is adjacent to the moderate earthquake's rupture extend where it stops at the 10-12km down-dip, then the PGV values could exceed 20cm/s according to Figure 3.1 and stress load could reach 0.1 MPa [2]. We also discussed the asperity sizes, the coupling with the transition zone, and the change in the effective normal stress.

Considering the previous studies describing the locked Kumburgaz fault segment as a

pure strike-slip fault with relatively simple geometry [101], we think our simple conceptual model can indicate the essential triggering effects of the moderate earthquake and impact on the seismic cycle of the locked fault segment. However, we should underline that the proposed conceptual model does not aim to give absolute quantities but rather to reveal possible upper bounds of the moderate earthquakes' triggering potential. We could reasonably mimic the instant and delayed triggering observed after the Mw7 Samos earthquake using simple slider simulations [102].

We applied four different state laws to test their triggering responses. Ruina displayed a better performance on velocity test [36, 89] and was also the favored form of nucleation on the natural faults [83]. Therefore, we elaborate on the Ruina law, which showed the maximum failure time advance that is almost twice of the conventional Coulomb's failure model. Also, we tested inertial effects on the triggering simulations by comparing QD and FD numerical strategies, which showed no sensitivity to the inertial damping and thus resulted in a very similar clock advance.

The rupture extent of this moderate event is only a few kilometers away from the locked Kumburgaz fault segment [2]. At such a close distance, nesting of static and dynamic effects is possible [64, 50]. Since there were no near-field recordings at the sea bottom near the rupture, the waveform recorded 35 km away from the source is multiplied by various scales ($\times 2$, $\times 5$, $\times 10$) to account for amplitude change with distance. The selected waveform that displayed the largest amplitude among available stations has a PGV of 4.51 cm/s and has dominant frequencies around 1 Hz. Scaling wave-forms by multiplying ($\times 5$ and $\times 10$) would result rather large PGV values (≈ 22 cm/s and ≈ 45 cm/s, respectively). Sensitivity analyses conducted using synthetic data and field observations indicated that longer periods and greater amplitude velocity perturbations have higher triggering potential [92, 75]. On the contrary, the dynamic effects are still negligible, even though the waveform amplitude is multiplied by 10 in our simulations. Hence, it is supposed to be a frequency threshold along with the amplitude, justifying the observations [75]. In this respect, the absence of low frequencies in the used waveform likely limits the dynamic triggering potential, and no instant triggering is possible in our simulations.

Aseismic transients can trigger large earthquakes as well [103]. The frictional het-

erogeneity can explain the shallow triggered creep events that are more sensitive to dynamic triggering than Coulomb-like static triggering as observed in Southern California [104]. The shallow creeping areas are more vulnerable to dynamic triggering due to lower effective static stress [105]. We considered three layers for the VW zone of large earthquake nucleation similar to characteristic earthquakes on NAF, a VS transition zone with RS friction, and a viscous layer at the down-dip to investigate the creeping effects. We did not consider the shallow creeping region because the locked fault segment of MMF has not displayed any shallow creeping motions; hence, it is suggested to be fully locked [95]. We tested various brittle-ductile coupling degrees to explore their effect on the seismic cycle. According to our results, strong coupling shortens the seismic cycle and amplifies the normalized clock advances suggesting dynamic triggering of deep aseismic zones, further promoting failure. When onset time is far from failure time ($>5\%$), observed clock advances become static but exceed Coulomb failure predictions during strong coupling, possibly due to the permanent effect of deep slip.

Segmentation of a fault system can control maximum earthquake magnitude [106, 107]. Previous studies indicate that discontinuities can act like barriers and prevent entire locked fault sections from rupturing during a single large earthquake [108, 109]. We vary the asperity size during simulations to mimic cases with effective fault segmentation. The reduced asperity size increased the earthquake frequency while decreasing the event size and produced mainly similar but slightly larger normalized clock advances implying limited sensitivity.

The source mechanism solutions of aftershocks suggested significant thrust components along the MMF [2], which can generate clamping along the fault. The Coulomb solution also points out normal stress decreases could initiate a large earthquake, which was observed on NAF before [2]. Therefore, we investigated the possible effects of shear-normal stress coupling by allowing the normal stress change by incorporating the formulation by [88]. Since shearing dominates the motion along the main fault segment, a more limited shear-normal stress coupling ($\phi \pm 10$) is tested, which indicates minor deviance in the resultant clock advances only detectable if fault failure is not close. Since the Kumburgaz fault segment is more likely at the end of its seismic cycle, we may suggest that the clamping will not significantly change its

state. In simulations, $\phi < 0$ raises the normal stress with the shear stress on the fault, increasing the fault strength and vice versa. The simulation result justifies the laboratory experiment, suggesting that the shear-normal stress coupling increases the healing rate [110]. Note that the reduced clamping ($\phi > 0$) can produce higher static time advances as pointed by [2] but can even exceed Coulomb failure predictions noticeably in cases where ϕ is significantly high.

Note that we conducted the simulations assuming ground shaking at the locked depth is similar to seismic recordings at the surface. This assumption would have maximized the ground shaking at the locked depth, which otherwise would be more limited. Thus, the result obtained from using waveform multiplied by $\times 5$, which is consistent with predicted PGV values by USGS, should be treated as the worst-case scenario for the triggering potential.

Rupture directivity can effectively amplify ground shaking. Especially directivity effects may form a pulse-like shape with a longer period and high amplitude, which can raise the triggering potential of nearby segments (e.g., [99]). For this event, [2] suggested a bi-lateral rupture with an asperity close to the locked Kumburgaz fault segment. If the rupture had displayed a high degree of directivity, the amplitude and triggering potential of the transient signal could also be more significant.

In conclusion, this moderate earthquake, near the Kumburgaz fault segment, was not strong enough to induce instant triggering. Many studies agree that the time left for a large earthquake within this segment is likely to be less than a few decades if not overdue (e.g., [55, 95]). Our simulation results stress out two different clock advance behavior depending on the onset time. Realistic simulations utilizing Ruina state law which favors earthquake triggering resulted in greater failure time advance ($\approx 1\%$ of the recurrence interval) than the other state laws and conventional Coulomb failure models suggest, within the shorter onset time window to failure. In general, the shape of the resultant clock advance curves are similar regardless of the degree of brittle-ductile coupling, asperity size, normal stress variations, or even used numerical strategies and thus robust, indicating that the failure time of locked fault is more imminent than before beneath the Marmara Sea.

CHAPTER 4

SIMULATION OF SEISMIC TRIGGERING AND FAILURE TIME PERTURBATIONS ASSOCIATED WITH THE 30 OCTOBER 2020 SAMOS EARTHQUAKE (MW 7.0)

In this chapter, we conduct numerical simulations to mimic the instant and delayed seismic triggering observed after MW7.0 Samos earthquake (30.10.2020). A few days after the earthquake off-fault small earthquakes showed a clustering at the south-east of the rupture plane. Those are examples of delayed triggering events. Also to investigate a possible triggering of large events on the surrounding faults faults near İzmir, where amplified ground motions caused heavy damage, we tested possible scenarios by considering different fault mechanisms. This chapter based on the work [102],

- SOPACI, EYÜP and ÖZACAR, ATILLA ARDA (2021) "Simulation of seismic triggering and failure time perturbations associated with the 30 October 2020 Samos earthquake (Mw 7.0)," Turkish Journal of Earth Sciences: Vol. 30: No. 5, Article 7. <https://doi.org/10.3906/yer-2104-6>
- Sopaci, E. and Özacar, A. A.: Simulation of Instant and Delayed Seismic Triggering Observed After the 30 October 2020 Samos Earthquake at Nearby Faults, EGU General Assembly 2021, online, 19–30 Apr 2021, EGU21-13090, <https://doi.org/10.5194/egusphere-egu21-13090>, 2021.
- Sopaci (2022). eyupsopaci/singledegreearthquaketriggering: v1.0.0 (v1.0.0). Zenodo. <https://doi.org/10.5281/zenodo.6964892>

We only make minor changes to fit the text appropriately in the context of this thesis.

4.1 Introduction

The 30 October 2020 Samos earthquake (Mw 7.0) ruptured the North dipping normal fault located North of the Samos Island [7]. Previous time-dependent seismicity studies using probabilistic approaches suggested the region being a nest for a not-too-distant-future large earthquake [111, 112]. The ground shake felt in Turkey and Greece caused fatal casualties in the Metropolitan city İzmir and Samos Island. Nevertheless, the most mattering question afterward was if the Samos rupture brings the surrounding faults close to failure, increasing seismic risk. Previously, Coulomb static stress changes are commonly used to assess seismic triggering [37]. Recently, the two-day apart Ridgecrest earthquakes (Mw6.4 followed by Mw7.1) on 4 and 5 July 2019 revive the efforts to understand large earthquakes' triggering [69]. In Turkey, such triggering of damaging earthquake was also proposed for the 17 August 1999 İzmit (Mw 7.4) and 12 November 1999 Düzce (Mw 7.2) earthquakes that ruptured neighboring segments of the North Anatolian Fault several months apart [113]. The traditional belief for earthquake triggering is that permanent stress transfer increases stress level in the vicinity of a rupture and triggers faults in short distances. In contrast, dynamic effects reach far distances and trigger small earthquakes. This definition is not entirely false but rather incomplete. Kilb and co workers [39] showed the first evidence to the best of our knowledge that the dynamic triggering causes asymmetry patterns in the seismicity rate. This asymmetry disappears when only static triggering is responsible for triggered seismicity. Today we know that not only static stress loadings advance (or delay) the clock of an earthquake in nearby faults, but transient signals alter the frictional state and lead to a further clock advance. A useful approach to understanding the static and dynamic triggering is the rate-and-state friction (RSF) [29, 30]. Many numerical simulations were conducted on single-degree-of-freedom (SDF) models [1, 46, 47, 114] and in a 2D continuum models [48, 49, 50, 82]. Besides, laboratory works contributed to understanding the physical mechanisms and dominance of static and dynamic effects individually [13, 41, 52]. We previously tested the miscellaneous views of friction on a pure vertical strike-slip fault triggered by static and dynamic signals [115].

The Samos earthquake occurred in a complex region where both strike-slip and nor-

mal faults indicate an ongoing transtensional tectonic regime. The observed almost instant triggering of neighboring strike-slip fault in the west and two-day delayed triggering of a seismic cluster at the SE side of the Samos Island provided much-needed observational data to analyze seismic triggering (Figure 1). In this study, we first computed the Coulomb static stress changes using a homogeneous slip model to reveal stress loading at nearby fault segments. Next, relocated aftershocks are analyzed both in space and time to establish the nature of seismic triggering at different aftershock clusters. Then, the seismic triggering cases observed after the Samos earthquake are simulated using RSF dependent SDF model with normal-shear stress coupling relation [88]. Unlike previous studies, both static and dynamic effects are considered during numerical simulations by utilizing computed Coulomb static stress changes and recorded strong motion waveforms as triggering signals simultaneously, which provided a unique opportunity to evaluate their relative role in a given triggering scenario. The results shed light on the conditions favoring instant and delayed seismic triggering, which are crucial to realistically evaluate the seismic triggering potential of an earthquake at nearby and far away fault segments.

4.2 Coulomb static stress changes

Coulomb static stress changes (ΔCSS) associated with an identified earthquake rupture are useful to evaluate stress loading at nearby faults and commonly correlates spatially well with the aftershocks [37]. In this study, the ΔCSS during the Samos earthquake is calculated with the Coulomb 3.3 software [116] by assuming an elastic half-space with uniform isotropic elastic properties. Since seismic triggering at nearby faults is considered, slip heterogeneity which can result in large variations within the rupture, is beyond our scope, and thus a homogeneous slip model derived by [7] is utilized. According to this model, the North dipping W-E trending fault segment with a length of 32 km and width of 15 km is ruptured during the Samos earthquake (Mw7.0) with an average slip of 2.5 m and a normal mechanism (strike : 270, dip : 45, rake : -89). The rupture initiated at the hypocenter (8.2 km depth) close to rupture bottom depth (11.2 km) and expanded up to ≈ 0.5 km depth beneath sea bottom. This simplified source model is compatible with geodetic (InSAR and GNSS)

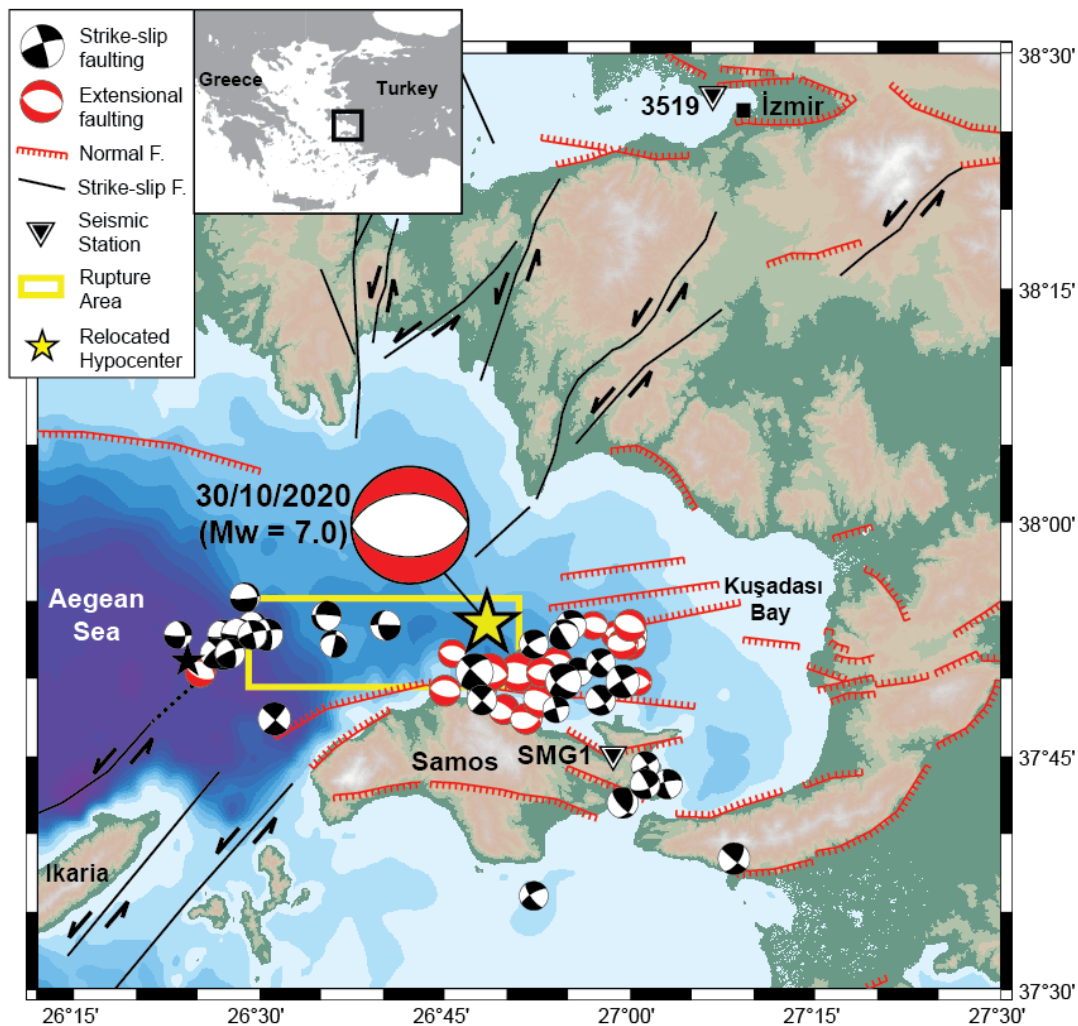


Figure 4.1: Topography and bathymetry map showing relocated hypocenter (star), rupture area (yellow outlined rectangle) and focal mechanism solution of the 30 October 2020 Samos Earthquake identified from regional waveform modeling [7] along with regional moment tensor solutions of aftershocks [8] and active fault segments (compiled from the Neotectonic map of Greece by [9, 10, 11, 12]). Two strong-motion stations near Samos (SMG1) and İzmir (3519) which are used during simulations are also plotted in the map.

and seismic (teleseismic, regional and strong motion) data [117, 118, 119, 120, 121]. Poisson's ratio and shear modulus are taken as 0.25 and 3.3×10^5 bar for the earth's crust. In the absence of data related to pore fluid pressure, we adopt 0.4 for the apparent friction. In a transtensional tectonic setting like this one, maximum stress direction may vary significantly, especially in terms of plunge amount. In this respect, plausible regional stress tensors are tested, revealing only minimal variations in amplitude used during simulations. Therefore, the regional stress tensor is not defined, and thus ΔCSS shown in Figure 2 is calculated for receiver faults with kinematics similar to the mainshock.

At 8 km depth, resultant ΔCSS indicates stress loading towards West and East and stress release towards North and South. Relocated aftershocks taken from [7] correspond spatially well with the positive ΔCSS where stress loading occurs. In this respect, strike-slip fault west of the Ikaria Island merges with aftershocks with strike-slip nature (Figure 4.1), and faults located within Kuşadası Bay and SE side of the Samos Island are subjected to static stress loading. Aftershock cluster that formed almost instantly in the western tip with dominantly strike-slip mechanisms is located where stress increase reaches up to 10 bars (Figure 4.2). On the other hand, the delayed aftershock cluster that emerged two days after the mainshock on the SE side of the Island display stress loading is only around 1 bar (Figure 4.2). Note that the identified positive ΔCSS at these two aftershock clusters will be adopted later in the numerical simulations as static triggering signals.

4.3 Aftershock evolution in time and space

The spatial and temporal distribution of the relocated aftershocks is shown in Figures 4.3. The minimal seismic activity observed between longitudes 26.5E and 26.8E matches well with the largest slip identified by finite fault models [7, 120, 121] and implies efficient stress release in this part of the rupture. The cluster in the western tip (Western cluster) emerges almost instantly, with the largest aftershock (Mw 4.1) appearing ≈ 2 h after the mainshock (star in Figure 4.3). In contrast, a cluster centered at the SE side of the Island (SE cluster) first emerges ≈ 50 h after the mainshock and reactivated again at ≈ 80 h (Figure 4.3). This pattern suggests a delayed triggering,

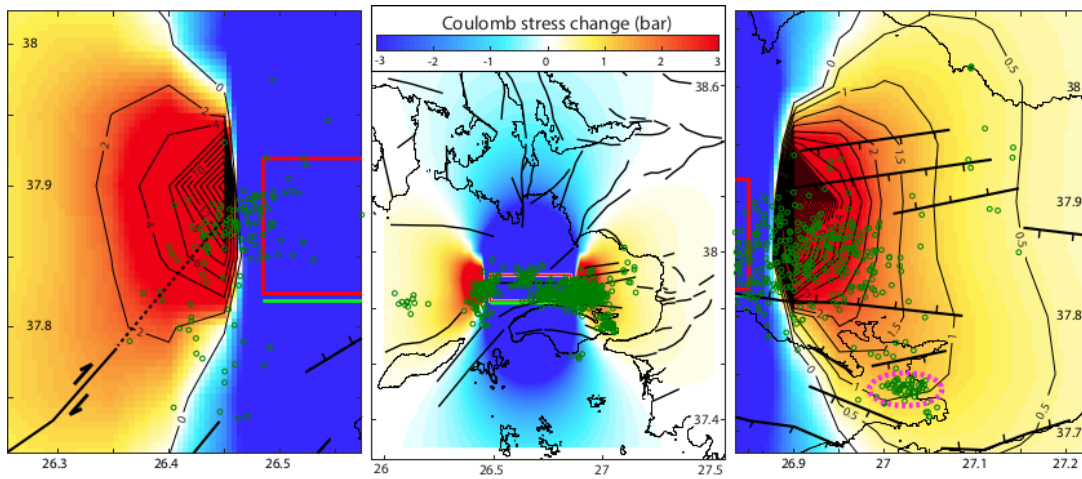


Figure 4.2: Coulomb static stress changes at a depth of 8 km. The large-scaled map is in the middle, and rupture edge close-ups with contour lines are given on the sides. The red rectangle and green line represent the projected rupture plane and fault trace at the surface, respectively. Solid lines represent faults. The relocated aftershocks shown by green circles are from [7] which are available online at http://www.geerassociation.org/administrator/components/com_geer_reports/geerfiles/TableS1.cat (accessed on 9.7.2021). The dashed magenta ellipse outlines the location of the SE cluster displaying delayed triggering.

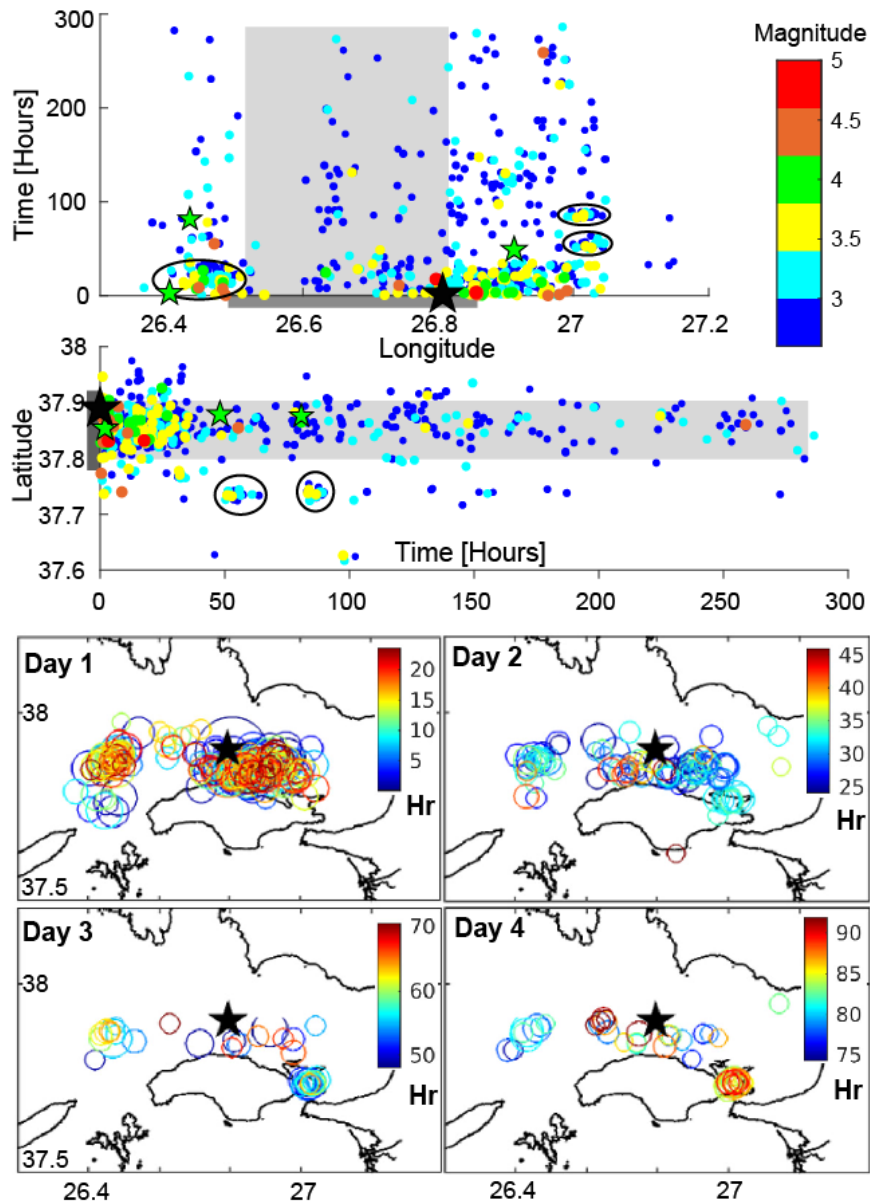


Figure 4.3: Time versus longitude and latitude plots (at the top) and daily maps (bottom) of relocated aftershocks taken from [7] (available online, web address is given in the caption of Figure 4.2). The grey area and ellipses outline the rupture area and aftershock clusters showing almost instant and delayed triggering. The black stars represent the mainshock and large aftershocks (green) within the western cluster and preceding SE cluster at $t \approx 50$ and 80 h. Note that aftershock data is color-coded according to magnitude (top) and hour of the day (bottom).

such that the Samos earthquake does not instantly lead to fault failure but advances their failure time significantly and thus resulted in time-lapse. In order to assess the effect of large aftershocks besides the mainshock on the observed delayed triggering, larger magnitude events preceding the SE cluster are examined and plotted (green stars in Figure 3). At $t \approx 50$ h, the preceding largest event (Mw 4.1) occurred at the eastern edge of the rupture, further North of the SE cluster. The maximum static stress loading associated with this rather low magnitude aftershock that occurs 20 km away from the SE cluster is calculated using an analytical approximation from [122], given by,

$$\Delta CSS = M_0 / (6\pi r^3) \quad (4.1)$$

where M_0 and r denote scalar seismic moment and radius of the asperity patch. According to equation 1, the static stress load is around only 12 Pa. Thus, its role in triggering is neglected. At $t \approx 80$ h, the preceding large aftershock (Mw 3.9) is located at the western edge more than 50 km away from the SE cluster and suggests no direct relation with delayed triggering. Besides, even the cumulative effects of aftershocks would not significantly change the SE cluster's stress load. Furthermore, observations suggest an amplitude-frequency threshold for dynamic triggering to be effective [75]. Our previous study shows that velocity amplitudes higher than 20–30 cm/s and lower frequency content dominance increase the triggering potential for large earthquakes [115]. In this respect, we reasonably assumed that the mainshock's static and dynamic impact instantly triggered the Western cluster and caused delayed triggering at the SE cluster.

4.4 Numerical simulation

4.4.1 Methodology and Data

We simulate strike and normal type faults using SDF spring slider systems with RSF dependent quasi-dynamic approximation [85]. The fault analogies for the vertical and inclined type faults are given in Figure 4.4. Of course, the SDF models in Figure 4.4

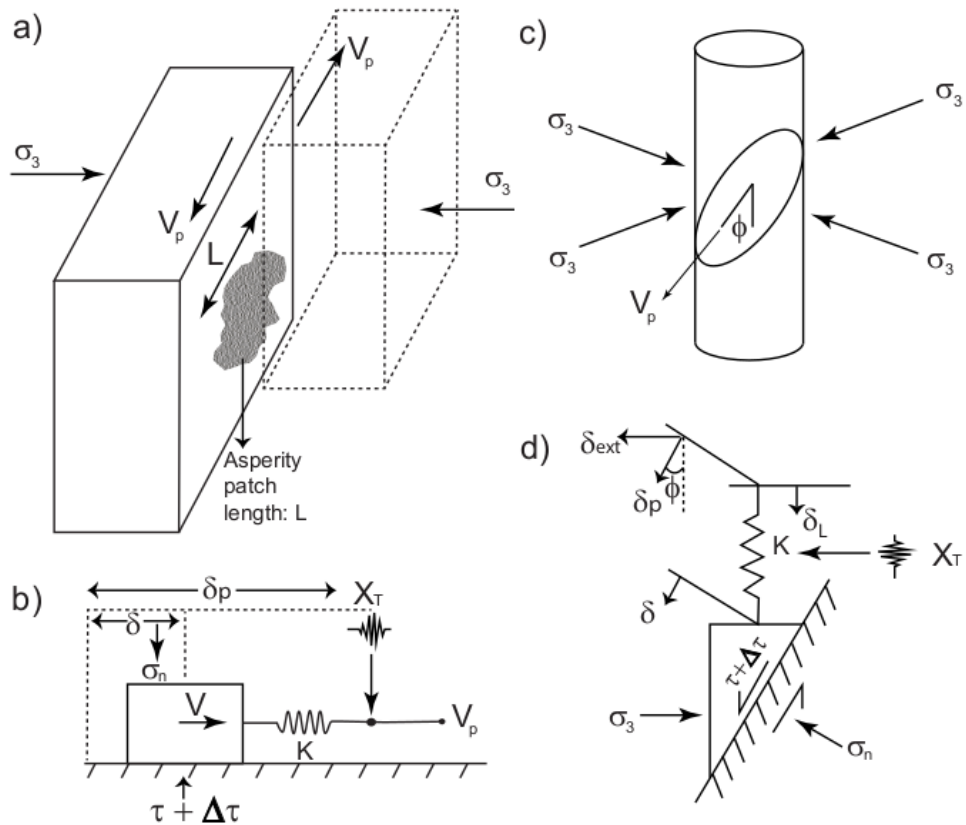


Figure 4.4: The fault analogies using single-degree-of-freedom (SDF) models. a) vertical strike-slip fault with a single asperity patch, b) spring- slider representation of vertical strike-slip faulting, c) a normal fault with an inclination angle (ϕ), d) spring- slider representation of inclined normal faulting. The figures are redrawn from [1, 13] for vertical and inclined faults, accordingly.

are oversimplified approximations and cannot manifest many complex properties of faults. However, as [48] inferred, SDF results do not differ significantly from a 2D continuum formulation in earthquake triggering works. Besides, complex knowledge beneath the seismogenic region, such as frictional heterogeneity and asperity barrier interaction, etc., are highly unknown. Therefore, we reasonably adopt SDF models to simulate observed triggering events after the Samos rupture. The quasi-dynamic approximation of the equation of motion is given in Equation 4.2.

$$K(\delta_{PL} + X(t) - \delta(t)) + \Delta_{CSS}H(t, t_p) + \eta v(t) = \tau(t). \quad (4.2)$$

$\tau, K, \delta_{PL}, \delta, \eta$ denote frictional stress, fault stiffness, driving plate's slip, block's slip, radiation damping, respectively. We insert permanent static $\Delta_{CSS}(t)$ and dynamic ($X_T(t)$) perturbation to the system at a specific time. The fault stiffness parameter is approximated with $K = G/L$, where G and L denote shear modulus and asperity patch length. The radiation damping is approximated by $\eta = G/V_S$ formula, where V_S denotes maximum shear velocity that the slipping block can reach. The RSF law for frictional stress is given in Equation 4.3.

$$\tau(t) = \sigma\mu(t) = \sigma(\mu_0 + a \ln(v(t)/v_0) + \Theta(t)) \quad (4.3)$$

where $\mu, \mu_0, \sigma, a, v, v_{PL}$ denote friction, friction constant, effective normal stress, RSF constitutive parameter for direct velocity effect, block's slip rate ($\dot{\delta}(t) = v(t)$), and the driving plate's slip rate ($\dot{\delta}_{PL} = v_{PL}$) accordingly. The state variable Θ defines the state of contact history between the frictional surfaces. In this study, we apply the Ruina type state evolution law in Equation 4.4 [30] because it provides better performance for dynamic transient effects [36, 115].

$$\dot{\Theta}^{(r)}(t) = -\frac{v(t)}{d_c}(\Theta(t) + b \ln(\frac{v(t)}{v_0})) - \alpha \frac{\dot{\sigma}_n(t)}{\sigma_n(t)} \quad (4.4)$$

In Equation 4.4, b denotes the RSF constitutive parameter for the state evolution effect, and d_c is the critical slip distance for renewing a contact between frictional surfaces. We also apply a shear-normal stress coupling relation proposed by [88] for

Table 4.1: Simulation Parameters

Parameters	Definition	0.005
a	Direct velocity effect	0.01
dc	Critical slip distance	1mm
α	Shear-normal stress coupling	0.5
σ_3	Principle stress	60MPa
μ_0	friction coefficient	0.4
G	Shear Modulus	33GPa
V_S	Shear velocity	3.5km/s
v_{PL}	slip rate on fault plane	1,3,5 mm/yr
L	Asperity patch length	Characteristic: 5km, Mw \approx 4: 1.25km, Mw \approx 3.5: 0.64km, Mw $<$ 3.5: 0.50km,
β	Dip angle ($\pi/2 - \phi$)	Strike-slip fault:90, Normal fault:60
ΔCSS	Coulomb static stress change	SE-cluster:1bar W-cluster:[1,3,5,7,10]bar

Default values for simulations, unless otherwise stated

normal type faults scaled with a constant α . When shear-normal stress coupling is applied, effective normal stress is computed with Equation 4.6.

$$\sigma_n(t) = \sigma_3 + \tau \tan(\phi) \quad (4.5)$$

where σ_3 is the minimum principal stress, and ϕ is the inclination angle as sketched in Figure 4. For vertical faults, $\sigma_3 = \sigma_n$, since $\phi = 0$. The parameters utilized during simulations are listed in Table.

The main parameters that control fault's stiffness and earthquake magnitude are asperity patch length and RSF parameters (a and b) [123]. In this study, the RSF pa-

rameters are kept identical to the [1, 47] and rock friction laboratory works. Instead, we varied the asperity patch length to test the triggering effect on different magnitude earthquakes. For events with $M_w < 5$, patch length (L) is calculated using the empirical relation between scalar seismic moment (M_0) and circular rupture area (A) from [93], given by.

$$M_0 A^{1.5} \quad (4.6)$$

For earthquakes with $M_w < 3.5$, ≈ 3.5 and 4, L which is equal to the diameter of circular patch is assigned as ≈ 0.5 , 0.64 and 1.25 km, respectively (Table). On the other hand, large crustal earthquakes are limited in rupture width and may display a high level of slip heterogeneity, and thus, L of characteristic large events are not empirical scaled with seismic moment (M_0) but kept fixed to 5 km following previous simulations works [93, 115]. By considering the present ambiguity associated with triggered fault, the range of slip rates ($1 \sim 5 \text{ mm/yr}$) are tested on both vertical strike-slip and 60° dipping normal faults. During simulations, static and dynamic triggering signals are applied simultaneously to represent the nearby fault segments' combined effect. A modified Coulomb's stress change for static triggering on RSF based model is used ($\Delta CSS = \Delta \tau (\mu_0 - \alpha) \Delta \sigma_n$) where $\Delta \tau$ and $\Delta \sigma_n$ represent shear and normal stress changes obtained from the Coulomb's solution near the aftershock clusters [124, 49, 51]. In this formulation, α , which defines the shear stress change's sensitivity to the normal stress, is taken as 0.5 following [88]. On the other hand, we use real seismic waveforms for dynamic triggering signals. For this purpose, strong motion data recorded by the closest seismic station (SMG1) at Samos Island is used as the dynamic triggering signal. Furthermore, the potential of a far-field dynamic triggering at faults near the İzmir metropolitan area is simulated using the strong motion record of seismic station (3519) near İzmir Bay which displays the largest recorded ground motions. The selected acceleration records are integrated numerically after trend and mean correction, and then low pass filtered with a cut-off frequency of 20 Hz to eliminate noise in velocity waveform. The resultant velocity waveforms used as dynamic triggers in the simulations and their unfiltered amplitude spectrum displaying attenuated high frequencies at distant recording (3519) near İzmir in comparison to the one (SMG1) near Samos are presented in Figure 5.

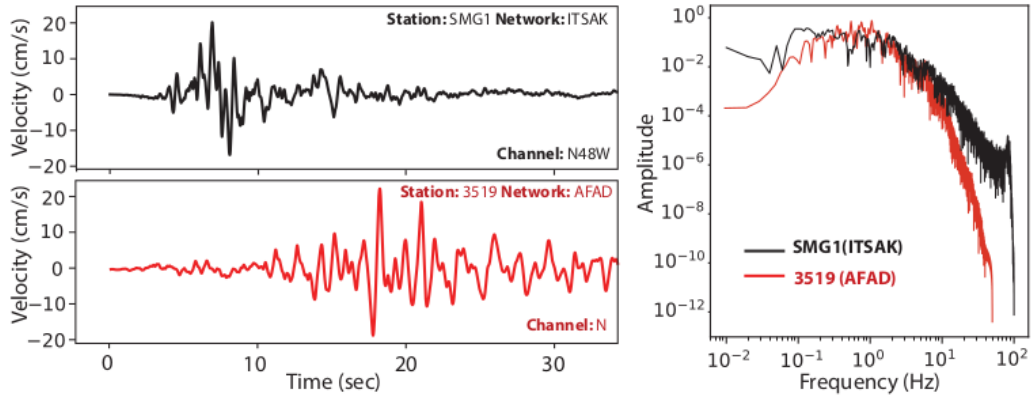


Figure 4.5: The seismic waveforms (on the left) are used for dynamic earthquake triggering and their unfiltered amplitude spectrums (on the right). Station SMG1, located in Samos Island, is operated by the Institute of Engineering Seismology & Earthquake Engineering (ITSAK), and station 3519, located in Karşıyaka, İzmir, Turkey is operated by the Disaster and Emergency Management Presidency of Turkey (AFAD). Check Figure 4.1 for station locations.

4.5 Simulation results

At first, scenarios analogous to the observed delayed triggering SE side of the Samos Island are established. Centroid solutions of aftershocks within the SE cluster display mixed mechanisms, including normal and strike-slip faulting (Figure 4.1). Therefore, simulations are constructed for both faulting types using a vertical fault analogy for strike-slip and inclined fault analogy with a dip amount of 60° for normal faulting (Figure 4.4). During simulations, we applied the shear- normal stress coupling relation of [88], in which normal stress evolves with shear stress at inclined normal faults and is fixed for vertical strike-slip faults. At the SE cluster where noticeable static stress loading is identified (Figure 4.2), ΔCSS is defined according to the modified Coulomb's solution as ≈ 1 bar using observed shear and normal stress changes of 0.8 and 1.4 bars, respectively. To evaluate the effect of fault slip rate, which is not well known in this case, we have also tested slip rates of 1, 3, and 5 mm/year.

For each scenario, an undisturbed seismic cycle is established with their recurrence intervals through numerical simulation. Then both static and dynamic triggers are

applied simultaneously at different times before failure. The simulation results revealed induced clock advances (simply the difference between the unperturbed and perturbed failure time). The measured clock advances are plotted concerning the triggering signals' onset time in Figure 6a. Since the slip velocity, fault type, and asperity patch length change the stressing rate and, therefore, the recurrence time, the absolute times are normalized by converting the observed clock advance and triggering signals' onset time into percentages with respect to the recurrence time. Owing to the normalization, we visualize results of multiple scenarios comparably (Figure 4.6 b).

According to the simulation results, earthquake triggering is a highly time-dependent process. The dynamic effects become pronounced when a fault is close to fail and result in a remarkable peak in clock advance (Figure 6). If the time to failure is more than 20 percent of the earthquake recurrence time (if a fault is not close to failing), the clock advance becomes linear. Hence, it displays only static effects comparable to the stress loading associated with ΔCSS (Figure 6). For the SE cluster, simultaneously simulated static and dynamic triggers do not produce instant seismic triggering at any onset time but rather lead to delayed triggering comparable to the observations when failure time is close.

Moreover, minimal variations identified in normalized clock advance imply that the seismic triggering is not much sensitive to fault slip rate and asperity patch lengths analogous to earthquakes with $M_w \geq 4$ (Figure 4.6b). On the other hand, normal faults display higher normalized clock advance due to static triggering effects suggesting that normal faults are more prone to static stress loading for strike-slip faults. Interestingly, as the dynamic triggering becomes pronounced, simulation results become independent from fault type, and similar values are observed for both strike-slip and normal fault types (Figure 4.6b). In absolute time frame, higher clock advances are identified for normal faults characterized by longer recurrence times (Figure 4.6a). For example, when ≈ 10 percent of the seismic cycle remains for normal fault failure, clock advance can exceed seven years for triggering a large characteristic earthquake with a recurrence time of over 500 years, which may apply to the faults located SE side of the Samos Island. Next, scenarios are constructed for vertical strike-slip faulting triggered almost instantly west of the rupture (Figure 4.1). Considering the observed minimal sensitivity, we fixed the fault slip rate to 3 mm/year. However, a

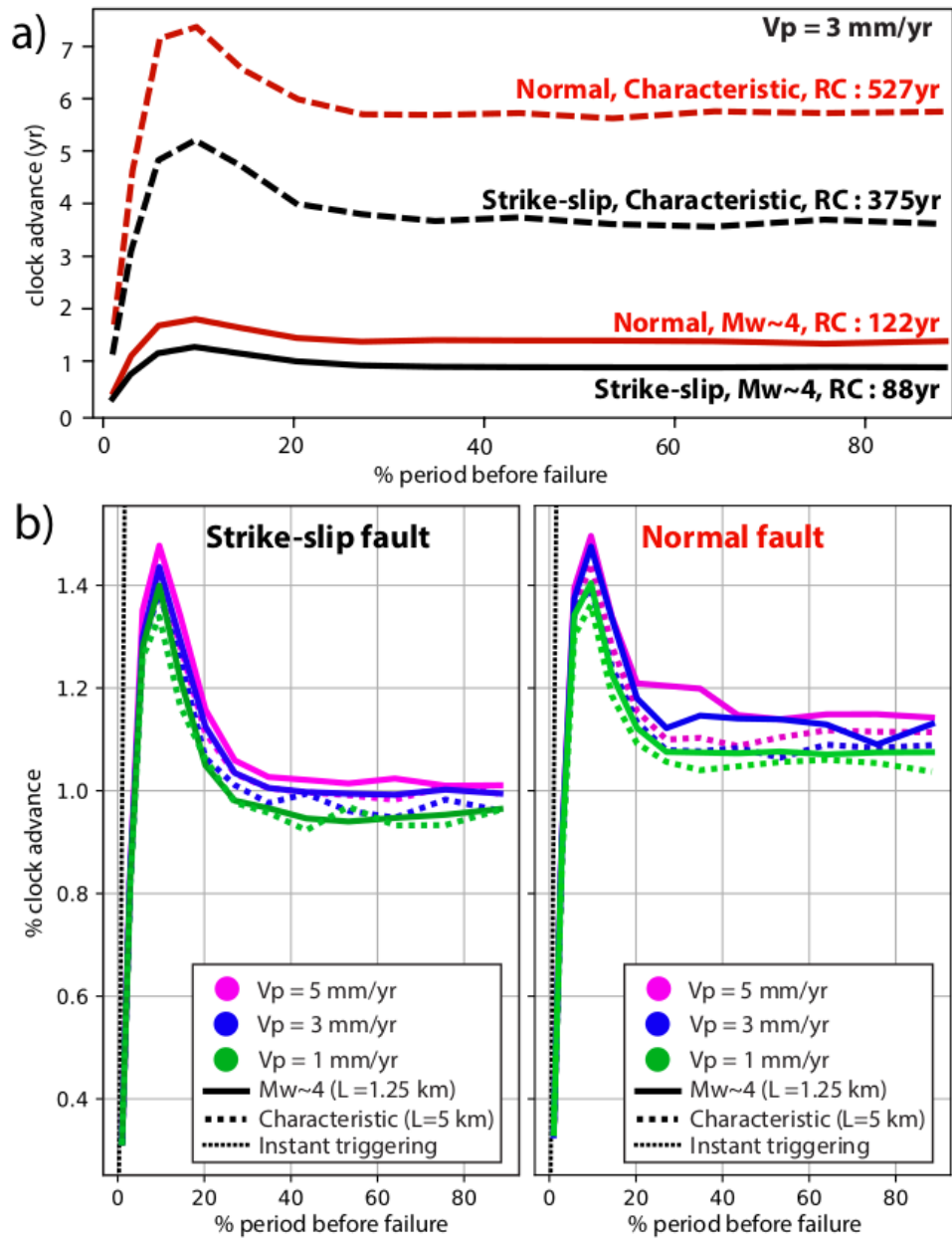


Figure 4.6: Triggering simulation results of large characteristic and $M_w \approx 4$ earthquakes with different recurrence times (RC) on normal and strike-slip faults analogous to the delayed triggering observed SE side of the Samos Island. a) absolute clock advance plots for fixed fault slip rate V_{PL} of 3 mm/year. b) normalized clock advance plots for variable V_{PL} .

wide range of ΔCSS from 1 to 10 bar is tested to represent stress loading right next to the rupture and slightly further away in agreement with the Coulomb solution (Figure 4.2). The normalized results are presented together for variable asperity patch lengths and ΔCSS values in Figure (Figure 4.7). According to our results, small earthquakes with $M_w < 3.5$ instantly trigger regardless of their position in the seismic cycle, while events with $M_w \approx 3.5$ instantly trigger depending on the given ΔCSS and triggering signal's onset time. Specifically, instant triggering occurred at ΔCSS of 1, 3, 5, 7, and 10 bars when 10, 15, 20, 27, and 35 percent of the seismic cycle is left to fault failure, respectively (Figure 4.7). The triggering potential of characteristic large earthquakes is also tested by increasing the asperity patch length to 5 km. Results reveal a significant increase in clock advance but do not lead to instant triggering except for very high ΔCSS values (≈ 10 bar). Finally, the far-field dynamic triggering effect of the Samos earthquake is evaluated on the normal faults located near the İzmir metropolitan area. For this purpose, seismic data of station 3519 located at the İzmir Bay (Figure 4.1), which displays the largest ground motions recorded in the region (Figure 5), is chosen as the dynamic triggering signal. Although the maximum peak ground velocity of 3519 is comparable to the SMG1 Samos Island station, the simulation analogous to normal faults near İzmir revealed no significant triggering effect on earthquakes' seismic cycle with $M_w \geq 4$ (Figure 4.8).

4.6 Discussion and conclusion

The seismic triggering potential of an earthquake on nearby or far away faults is hard to quantify due to the present high-level uncertainty associated with friction, fault zone parameters, and onset time of a triggering signal within the seismic cycle. Thus, triggering phenomena have been studied commonly employing laboratory experiments [13, 42, 41] and numerical simulations [1, 46, 47, 50]. It becomes even more challenging at close distances with the nesting of static and dynamic triggering effects [39, 50]. After the 30 October 2020 Samos Earthquake, two distinct off-plane clusters with maximum $M_w \approx 4$ are identified, which provided a unique opportunity to study the triggering mechanism of recorded small and moderate-sized earthquakes.

Western cluster associated with strike-slip faulting at the rupture edge is triggered

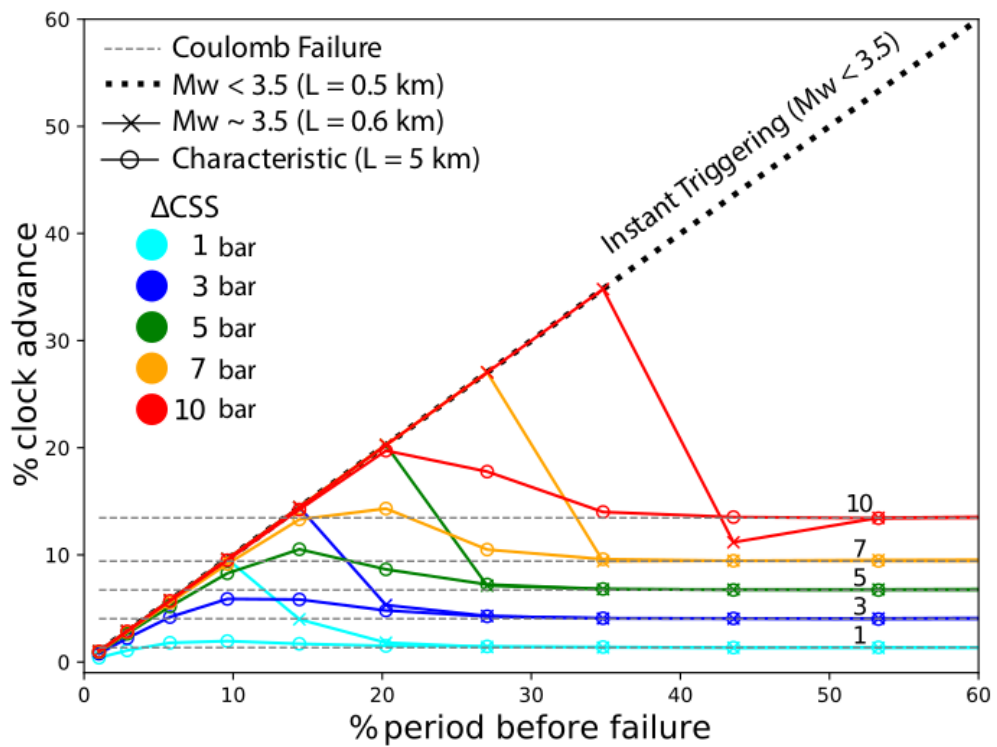


Figure 4.7: Triggering simulation results of large characteristic, Mw 3.5 and Mw < 3.5 earthquakes on a vertical strike-slip fault for variable Coulomb static stress change analogous to the almost instant triggering observed west of the rupture.

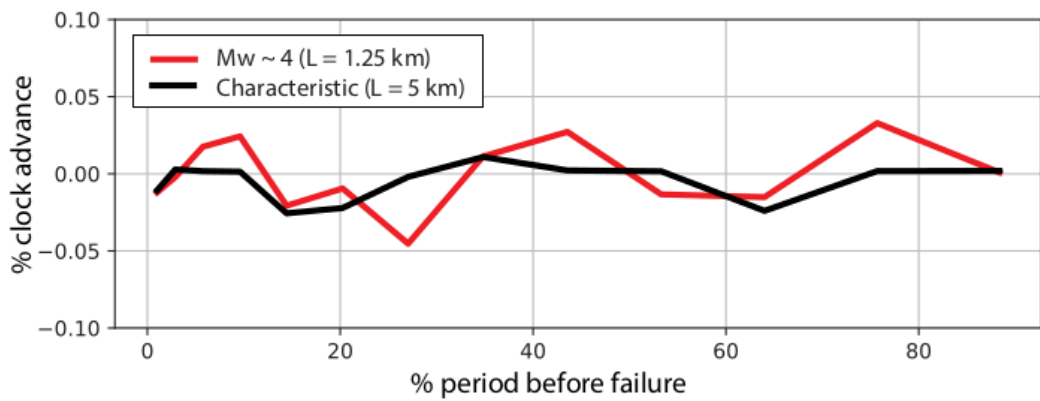


Figure 4.8: Far-field dynamic triggering simulation results showing normalized clock advance plots of large characteristic and Mw 4 earthquakes on normal faults analogous to faults nearby İzmir.

almost instantly. In contrast, the SE cluster has emerged two days after the mainshock further away from the rupture area. The resultant ΔCSS distribution correlates well with the relocated aftershocks. It indicates significant stress loading on the rupture edges that reach 10 bars around the Western cluster and is close to 1 bar across the SE cluster (Figure 4.2). During simulations, computed ΔCSS values and recorded seismic velocity waveforms are applied simultaneously as static and dynamic triggers for an SDF fault model governed by the RSF law of [30].

According to the sensitivity analysis among available RSF laws [115], the chosen Ruina law performs better dynamically but note that usage of alternative views of friction may alter the simulation results. For a particular target fault segment where fault parameters' depth and lateral variations are well known, more complex 2D-3D continuum formulations can be viable [28, 125]. However, for laterally uniform fault models, SDF and 2D simulations produce rather similar results [49]. Due to the lack of data associated with target faults and limited magnitudes of triggered events, complex fault models are kept beyond this study's scope. Nevertheless, our simulations can reasonably mimic the triggered events observed after the Samos Earthquake.

The uniform slip model adopted for the rupture excludes complex static stress changes that may occur within the rupture due to slip heterogeneity and thus not suitable for triggering assessment of aftershocks located within the rupture plane. It is also worth noting that the assumption of rupture with constant slip may result in artificially higher ΔCSS at close distances to the rupture edge. Similarly, the surface ground motion recorded at nearby seismic stations may exceed the actual motion on the locked deep section of the target faults due to the amplification of seismic waves at the surface. Therefore, dynamic effects may be slightly exaggerated. In this respect, the resultant failure time advances should be treated with caution as the likely maximums.

In general, our results suggest a nonlinear relation to the triggering onset time, compatible with the previous studies [1, 46]. Dynamic triggering becomes effective only when a fault is closer to fail and significantly increases the clock advance. Otherwise, static triggering effects lead to a rather constant clock advance due to stress loading comparable with ΔCSS . Our simulations also reveal a sharp decrease in clock ad-

vance when failure time is very close, limiting instant triggering (Figure 4.6). This nonlinear response is associated with the RSF based model, which is different from Coulomb failure models utilizing a constant stress threshold [46]. In this respect, the rare occurrence of instantly triggered moderate or large earthquakes in nature may support its existence.

For small earthquakes ($M_w \leq 3.5$), dynamic triggering is more effective and controls the triggering process. The dynamic signals recorded by the seismic station at Samos Island instantly trigger the events with $M_w < 3.5$ regardless of the onset time. For earthquakes with $M_w \approx 3.5$, static effects become more noticeable, and instant triggering is favored by increasing ΔCSS and/or decreasing time to failure (Figure 7). In contrast, the triggering scenarios for $M_w \geq 4$ earthquakes result in a significant clock advance but almost always produce delayed triggering events analogous to the SE cluster (Figure 6). However, if ΔCSS takes high values (≈ 10 bar), instant triggering events may occur at the rupture edges like the Western cluster (Figure 4.6).

Not surprisingly, small earthquakes ($M_w \leq 3.5$) are more prone to seismic triggering. Scenarios tested for asperity patch lengths 1.25 and 5 km analogous to $M_w \approx 4$ and large characteristic earthquakes, respectively, result in surprisingly similar triggering responses (Figure 6). This finding may suggest that earthquakes with $M_w \geq 4$ display self-similarity during seismic triggering for a wide range of magnitude. Moreover, the fault slip rate, which defines the recurrence time interval of earthquakes in the target fault, produces a minimal change in normalized clock advances. In other words, the slip rate's uncertainty is not much critical for seismic triggering simulations.

In order to evaluate the effect of target fault type on seismic triggering, both normal and strike-slip analogies are tested. Both fault types reveal very similar responses when a fault is close to failing but differ when stress build-up on the fault is limited (Figure 6). Based on our results, normal faults with inclined fault geometry are more prone to static triggering and display noticeably higher normalized clock advance than strike-slip faults. The applied normal-shear coupling as a function of the dip angle [13] causes such an effect. A change in slip velocity across a dipping fault plane varies normal stress along with shear stress while normal stress remains constant at vertical faults. Unlike here, strike-slip faults can be exposed to normal stress change

due to clamping effects that depend on the source and receiver fault positions [126] which cannot be included in our SDF model. Moreover, local fluctuations caused by dynamic transient waves may change fluid pore pressure [127] and affect normal stress beyond our scope.

According to our results, simulations indicate that the dynamic effects are less pronounced than static effects for earthquakes with $M_w \geq 4$. In general, dynamic triggering requires higher amplitude signals to have an equal clock advance with the static triggering [1, 47, 50]. According to [115], the signals that exceed peak velocity of 30 cm/s produce remarkably more pronounced dynamic impact. At the SMG1 station displaying the largest ground motions recorded nearby, the maximum seismic velocities are around 20 cm/s, limiting the observed dynamic triggering responses in the simulations. Moreover, the dominance of dynamic triggering is highly dependent on the direct velocity effect parameter "a" (Sopaci and Özacar, 2020), which is kept constant according to the previous simulation and laboratory works [1, 47]. Therefore, lower values of the "a" parameter may significantly increase the dynamic triggering effects [70], or vice-versa [32].

After a damaging earthquake, public living where damaging earthquakes are expected commonly asks whether this event can trigger a large earthquake at faults near to them. The Samos earthquake caused heavy damage concentrated in the İzmir metropolitan area and a high level of public anxiety. Across the Bornova plain, ground motions were amplified anomalously by the thick basin bounded by normal faults from both North and South [11]. Static stress changes associated with the Samos earthquake are negligible across İzmir, which is ≈ 70 km away but observed dynamic effects can alter the frictional state of faults with large earthquake potential. In order to provide insight on the far-field dynamic triggering potential of the Samos earthquake, the seismic velocity waveform recorded near İzmir is applied as a dynamic trigger for earthquakes with $M_w \geq 4$ on a normal fault. Simulations indicate no significant frictional state change due to dynamic triggering, leading to clock advance (Figure 8).

In conclusion, both instant and delay triggering of earthquakes with $M_w \leq 4$ were observed after the Samos earthquake are successfully simulated. Faults adjacent to

the rupture are more likely to trigger, particularly the NE-SW trending strike-slip fault bounding the Ikaria Island from the West, producing a large earthquake. In contrast, faults near İzmir remain unaffected by the dynamic triggering of the Samos Earthquake.

CHAPTER 5

SIMULATION OF LARGE EARTHQUAKE SYNCHRONIZATION AND IMPLICATIONS ON NORTH ANATOLIAN FAULT ZONE

In this chapter, the synchronized behavior along North Anatolian Fault (NAF) Zone is examined on a continuum model, consisting of three strong asperity patches using the pseudo-spectral FFT method and Rate-and-State (RSF) dependent friction. The historical data exhibits quasi-regular rupture times and clusters of large events in space where nucleation and arrests of characteristic ruptures at the locations of step-overs, and indicate velocity-strengthening barriers. The main challenge to studying such phenomena is that the recurrences of large characteristic events are rare in nature, suffering adequate and reliable data. In the scope of this study over 275 scenarios analogous to NAF, generating over 30000 earthquakes were examined. The results suggest that a transient triggering mechanism mainly controls the synchronization behavior, unlike the traditional belief which states permanently raising or lowering stress on the asperity patch, which is called static triggering and is often quantified by Coulomb's stress failure criteria. The direct velocity effect a in the framework of RSF shows the highest sensitivity for synchronization, by altering two distinct processes on asperities, where earthquakes nucleate, and on barriers, where relaxation oscillation of loaded stress takes place. Particularly by changing the a parameter, and/or also depending on other factors including the barrier's length and its frictional properties, the coupling effect between the asperities can drastically change. An over-coupled stress interaction between asperities causes premature partial ruptures which leads to more "complex" earthquake recurrences, and prediction of triggered next earthquakes is extremely challenging. If the coupling is extremely weak, then the characteristic events are more regular and more predictable, with no synchronization pattern as it is labeled as "independent". On the other hand, the adequately cou-

pled systems show synchronization analogous to NAF. The different "state" laws or contacting properties of interfaces in the framework of RSF resemble each other at the velocity-strengthening barrier, but they drastically differ in generating dynamic ruptures, hence the results also depend on the type of state definition significantly. The classified results as "complex", "independent", and "synchronized" offer distinguishable contrasts in rupture wave speeds, ground motion observable of pre-seismic, co-seismic, and post-seismic duration, and extents, which can be readily observed in nature. The study indicates that rupture wave speeds, peak ground velocity and tracking post-seismic slips are of great importance to define synchronization behavior and hence the predictability of the next large earthquakes in nearby faults.

Some parts of this chapter are presented at the EGU conference 2022, received the Roland-Schlich travel cost award, and participated in the Outstanding Student and Ph.D. candidate Presentation Contest [128]. The full manuscript is also prepared for the Journal of Geophysical Research-Solid Earth, yet to be submitted. We only make minor changes to fit the text appropriately in the context of this thesis. The code is also publicly available in GitHub [60].

5.1 Introduction

The North Anatolian Fault Zone (NAF) has a historical record of large earthquakes ($M_w > 7$) that exhibit clusters in space-time [18, 17, 14]. The ruptures tend to initiate and arrest at the edges of these clusters, which has been observed to occur at step-overs as shown in Figure 5.1 [16, 19, 20, 57]. This clustering pattern has been attributed to the presence of "velocity-strengthening" barriers at the cluster edges, which can prevent ruptures from spreading from one segment to another or mitigate the transfer of stress [27, 24]. This raises the question of what conditions can lead to the triggering of neighboring segments, thereby increasing the seismic risk.

Studies of rock friction have established that a fault segment can undergo stick-slip motion if it is velocity weakening (VW) or tends to creep if it is velocity strengthening (VS) [29, 30]. The type of motion is determined by the critical elastic stiffness relation within the framework of rate and state friction (RSF) [30].

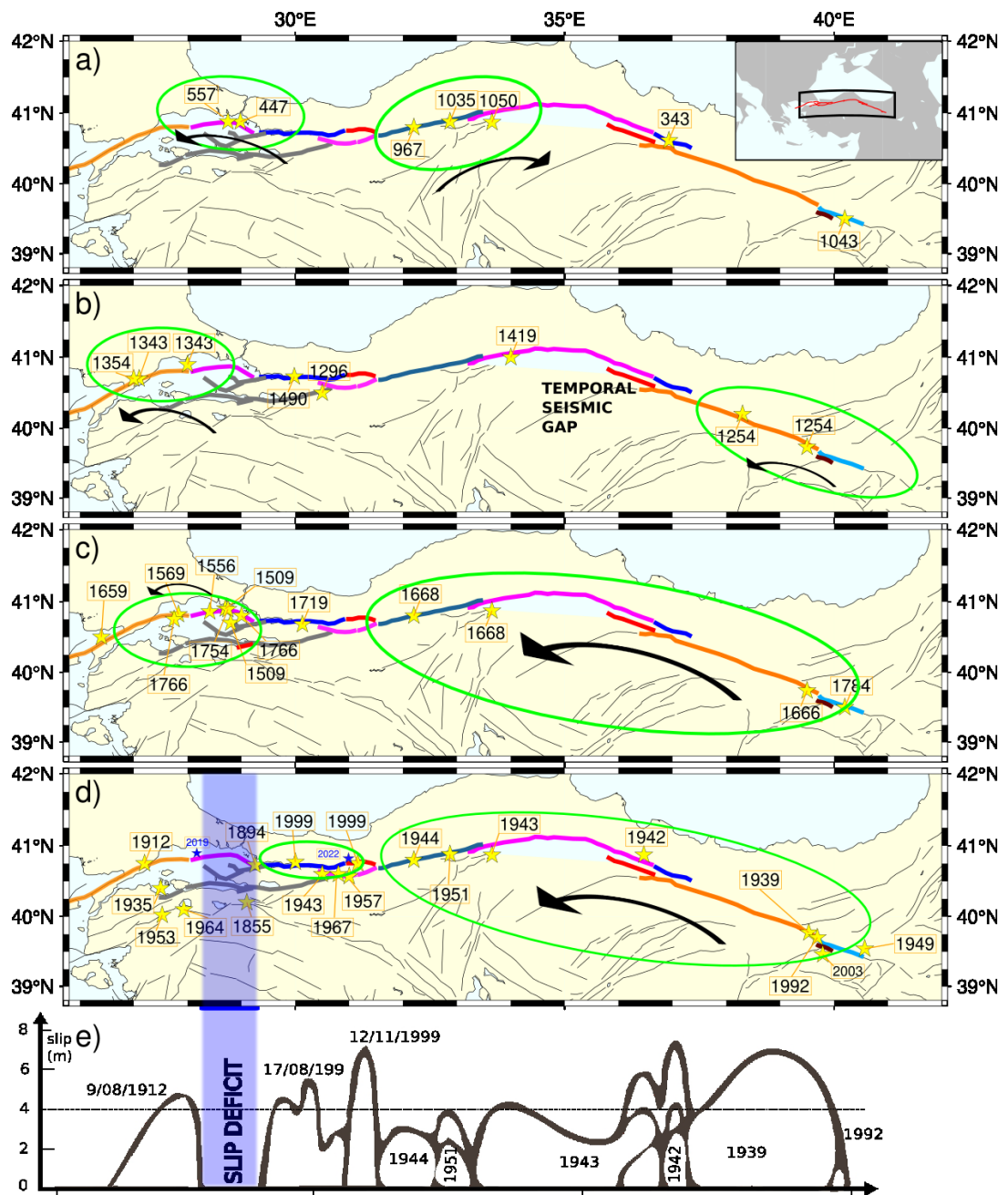


Figure 5.1: Map showing the historical earthquakes along North Anatolian Fault zone (a-e) and synchronized clusters, and its approximate recent situation (f). The historical earthquake catalog is compiled from studies [14, 15, 16, 17, 18]

$$k_{cr} = \sigma_n(b - a)/d_c \quad (5.1)$$

If the stiffness is lower than the critical value $k < k_{cr}$ (corresponding to RSF parameter is $0 < a - b$ and the VW size is larger than a critical length [35, 129]), the patch can nucleate earthquakes. The terms VW and VS patches refer to asperities and barriers, respectively. Numerical simulations assuming that the frictional stress on the fault is RSF have revealed various aspects of earthquakes, particularly concerning the role of barriers in affecting fault interaction and earthquake triggering and synchronization.

The study by [26] found that the size of the VW patch relative to the critical size and the frictional properties of the VS barrier is important for synchronization. The time delay between failures of two VW patches increases as their distance increases, and they may eventually become independent. [27] proposed a non-linear barrier efficiency parameter that depends on the VW asperity size, VS barrier size and barrier frictional property to control the probability of joint generation of a large earthquake. [28] found that the critical density of asperities and the frictional properties of the barriers form a threshold that determines the simultaneous failure of asperities and destabilization of the creeping region.

Analog models by [130] investigated the synchronization patterns of megathrust earthquakes in nature, finding that the ratio of the barrier and VW patches (Db/Da) determines the barrier's effectiveness. [131] extended the study by considering strength contrasts and longer simulations, proposing a stress coupling relation (based on the ratio of Coulomb static stress transfer and static stress) that controls synchronization. Both studies emphasize the importance of the ratio between the VW asperity and VS barrier, similar to the findings of [27].

Recently, Wei et al. (2021) conducted simulations to mimic the synchrony observed at Oceanic transform faults in the East Pacific Rise, which consisted of two asperities and a separating barrier with initial heterogeneous stress. They found that co-seismic static stress changes can lead to synchronization, contrary to Scholz (2010), who explained that synchrony in coupled oscillators could occur only if intrinsic velocities are similar. They also concluded that barrier width is more sensitive to synchronization than its frictional strength.

On the other hand, Lambert (2021) warned that simplifications could influence the outcomes of physics-based simulations in inertial effects and numerical discretization. Many studies use a simplified quasi-dynamic (QD) approach for lower computational costs. However, full-dynamic (FD) effects can generate different results, such as changes in slip rate and wave speed, affecting the jumping rate of ruptures between asperities. Additionally, laboratory and numerical methods can produce different velocity perturbations. These differences should be considered seriously in numerical studies.

Here, we explore the issue of long-term spontaneous segment failures using a physics-based model that is designed to be analogous to the North Anatolian Fault (NAF). Our numerical setup includes three strong vertical asperities (VW) separated by two barriers (VS) within the Rate and State Friction (RSF) framework. Two asperities have the same stress level, while the third has a slip deficit. This initial stress contrast simulates the recent pendency of a large earthquake at the western edge of NAF.

We use a numerical method described by [22] with the spectral FFT code [60] and apply two state laws for frictional weakening, namely aging and slip state evolution (Dieterich 1979, Ruina 1983). These two state laws are chosen for their distinct differences in large perturbations (Nakatani 2001, Bhattacharya 2015) and nucleation and propagation patterns (Ampuero 2008). The slip law performs better in triggering and synchronization (Nakatani 2001). Nevertheless, all previous studies have used the aging state law (Dieterich 1979), except Kato et al. (2004) used a composite law. Moreover, the QD simulations with slip law demonstrate the wave propagation speed can reach shear wave speed, while the aging law displays slower wave propagation, and the inclusion of FD can increase the speed to the shear wave speed level. We conducted analyses with QD for computational efficiency. A comparison of full-elastodynamic effects is in the appendix, but a more comprehensive comparison will be left for future work.

The main objectives of this study are to:

- Determine if synchronization of large earthquakes, similar to NAF, can be simulated using physics-based numerical models.

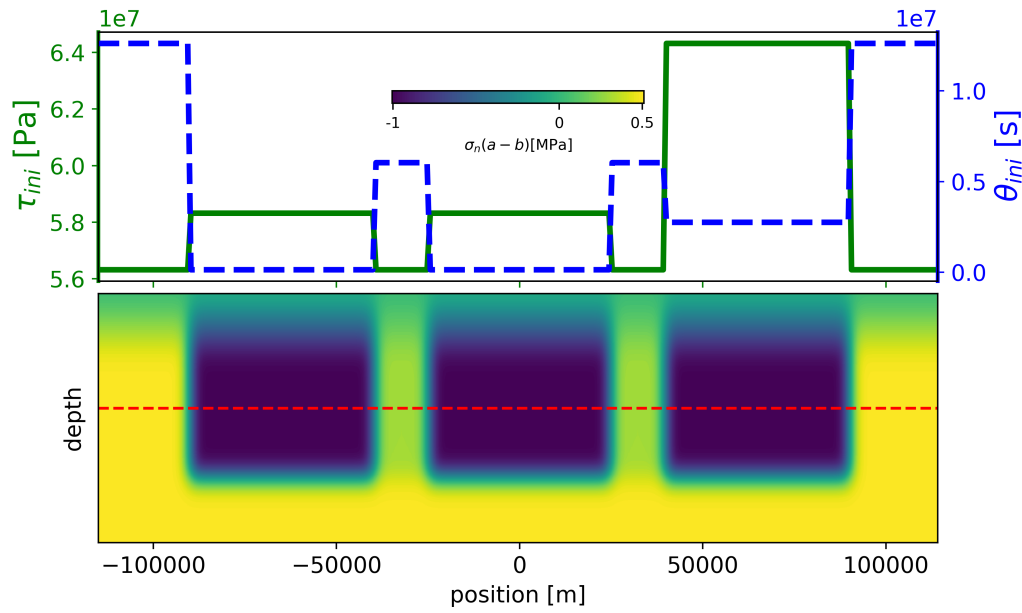


Figure 5.2: Simulation set-up: a) Initial values, b) a representation fault model.

- Investigate the underlying physical mechanism behind this synchronization.
- Assess the implications for NAF and other major fault zones.
- Identify natural indicators for rupture triggering and synchronization potentials.
- Better understanding of large earthquake synchronization is limited by scarce data and poor resolution. The results can improve seismic hazard assessments.

5.2 Simulation Set-up

We assumed three large asperities in a 2D medium, where simulations correspond only to the red dashed line in Figure 5.2, and the width information is added with [132]. The shear stress on the interface τ is assumed to be Rate and State friction computed by:

$$\tau = \sigma_n \mu = \sigma_n \left[\mu_0 + a \ln \left(\frac{v}{v_0} \right) + b \ln \left(\frac{v_0 \theta}{d_c} \right) \right] \quad (5.2)$$

where σ_n denotes the effective normal stress, μ and μ_0 are the friction and reference friction at the reference velocity v_0 . The second and third terms on the right-hand side (5.2) contributes as velocity v (dynamic) and state θ (static) dependence of friction, where d_c is the critical slip distance. a and b are constitutive parameters for direct velocity and state evolution. Two empirical state evolution formulas for θ to complete equation 5.2, namely aging and slip laws, are given by [29, 30].

$$\dot{\theta} = 1 - \frac{v\theta}{d_c} \quad (5.3)$$

$$\dot{\theta} = -\frac{v\theta}{d_c} \ln \left(\frac{v\theta}{d_c} \right) \quad (5.4)$$

The elastic stress is defined by:

$$\tau(x, t) = \tau^0(x) + f(x, t) - \frac{G}{2c_s}(v(x, t)) \quad (5.5)$$

where τ^0 is the loading stress, assuming no displacement discontinuity on the fault plane [22]. The last term in equation 5.5, $G/2c_s(v(x, t))$ is the radiation damping [85] to sustain a solution during rupture, where G and c_s are shear moduli, and speed [85]. The second term is the stress transfer functional $f(x, t)$, for which we applied the spectral FFT method [58, 22]:

$$\begin{aligned} \delta(x, t) - v_{PL}t &= \sum_{n=-N_{ele}/2}^{N_{ele}/2} D_n(t) e^{ik_n x} \\ f(x, t) &= \sum_{n=-N_{ele}/2}^{N_{ele}/2} F_n(t) e^{ik_n x} \\ k_n &= \frac{2\pi n}{\lambda} + \frac{2\pi}{W} \end{aligned} \quad (5.6)$$

where k_n is the spatial frequencies along the periodic domain λ and W is the width of the fault (depth) and N_{ele} is the number of elements over space domain. D_n and F_n are the complex Fourier coefficients of slip $\delta(x, t) - v_{PL}t$ and stress transfer functional $f(x, t)$, where v_{PL} is mean driving plate velocity. The Fourier coefficients of the stress transfer function are computed by:

$$F_n(t) = -\frac{G|k_n|}{2}D_n(t) + \int_0^{Tw} W(|k_n|c_s t')\dot{D}_n(t-t') dt' \quad (5.7)$$

The first term is the so-called "static" term that contributes most during the slow phase. The second term contributes as the dynamic term, computed with truncated convolution integral within a window $(t_i, t_i - Tw)$ over coefficients history of $(dD_n(t)/dt)$ [22]. In this study, we conducted most analyses by ignoring the second "dynamic" term for computational efficiency corresponding to QD approximation. We solved the equation of motion explicitly using adams' multi-step predictor-corrector method by setting equations 5.2 and 5.5 equal and using a state evolution formula 5.3 or 5.4 [133]. We searched for synchronization patterns using the following simulation parameters.

Table 5.1: Simulation Parameters

Params	min	max	default
a_{asp}	0.005	0.015	0.01
$a - b_{bar}$	0.000	0.005	0.005
$d_c[mm]$	8	24	8
$L_{asp}[km]$	30	100	50
$L_{bar}[km]$	5	20	15

$$v_{PL}=0.02m/yr, G=30GPa, c_s=3km/s, \mu_0=0.6$$

$$W=50km, \sigma_n=100MPa, a - b_{asp}=-0.01$$

As mentioned, the simulation outcomes obeying RSF depend drastically on the spatial resolution, called length scales. We set the minimum number of cells per the cohesive zone to $\Lambda_0/dx \geq 9$ for $a_{asp} \geq 0.01$ and $\Lambda_0/dx \geq 12$ for $a_{asp} < 0.01$, where a_{asp} and dx denote minimum direct velocity effect parameter at the asperity and cell size. The cohesive zone is computed by:

$$\Lambda_0 = C_1 \frac{Gd_c}{b\sigma_n} \quad (5.8)$$

where C_1 is a constant around 1 [134]. The setting resolution according to equation 5.8 makes $h^*/dx \gtrsim 20$ according to [22], which is necessary to prevent cells from becoming unstable and failing independently where critical cell size h^* is computed

by.

$$h^* = \frac{\pi}{4} \frac{Gd_c}{(b-a)\sigma_n} \quad (5.9)$$

5.3 Simulation Results

5.3.1 Classification of Results

We perform sensitivity analyses on parameters listed in Table 5.1 using initial conditions shown in Figure 5.2.

The fault zone is considered synchronized if all asperities fail in a coupled manner within a critical value, defined as the failure time differences between ruptures. We first identify full ruptures (complete slipping of asperities). Then, we calculate the failure time difference between neighbor asperities during full ruptures and normalize them using the mean recurrence time for comparison. If the normalized difference converges to a value less than 10% of the mean recurrence time, the status is set to synchronized (status=1). If not, it is labeled as complex (status=0). If the normalized difference converges to a value higher than 10% of the recurrence time, the status is labeled as "independent" (status=-1).

A fitting of the failure time differences to the earthquake cycle count allows a unique comparison by obtaining synchronization rate and stability. We applied a third-order polynomial model with a constraint Gauss-Markov model [135] if a synchronization pattern exists. The constraint is applied to force the fit to pass through the tangent line, corresponding to the failure time difference between the successive events becomes stably short enough. Then the residuals of the constraint fit are fitted to an exponential model $\beta_0 \exp(\beta_1 x)$, where parameter β_1 represents the convergence rate [136]. Let us now present examples of converged, complex, and independent cases.

Figures 5.3 and 5.4 demonstrate a gradual decrease in time differences between neighboring asperities, leading to fault segment synchronization. Both setups have the same parameters, except they use different state laws. Although synchronization patterns are similar (as seen in Figures 5.3-c and 5.4-c), the dynamics of the state laws are vastly different. The wave propagation speed of the slip law is twice as fast as

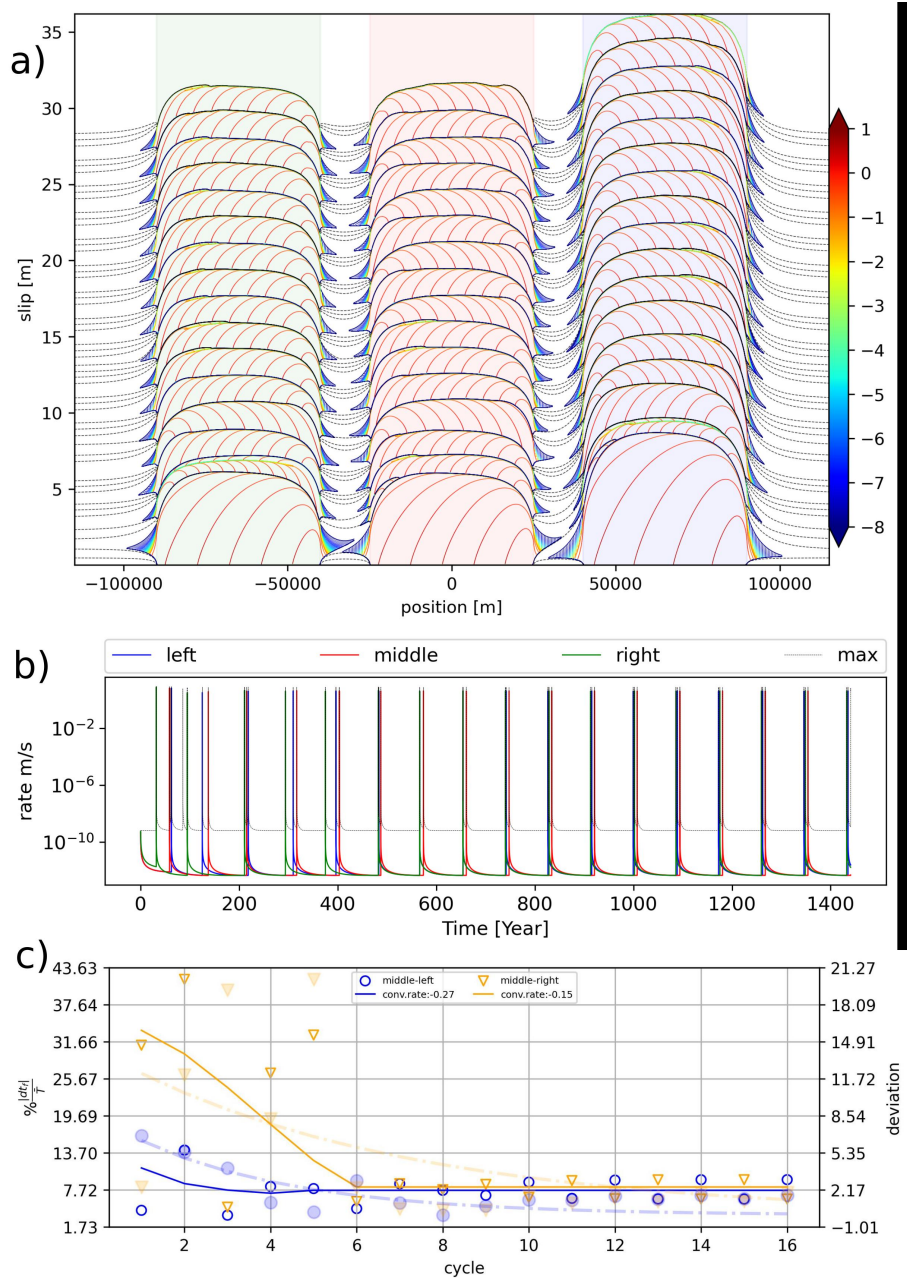


Figure 5.3: A synchronization example using slip law and default parameters in Table 5.1. a) slip profile: slip velocities are plotted in the logarithmic scale defined in the color bar on the right side. The dynamic rupture is plotted in two-second intervals, and post- or pre-seismic events are plotted with scatter plot until they reach a critical value $v_c = 10^{-8} m/s$. The inter-seismic times are plotted with black dashed lines every 20 years interval. b) time series of the middle of each asperity. The colors are given in the legend. c) Synchronization status of adjacent segments. Solid thin lines and scatters without face color denote constraint fit to normalized adjacent segment's failure time differences. The filled color scatters and bold dashed lines denote the deviations from the constraint fit.

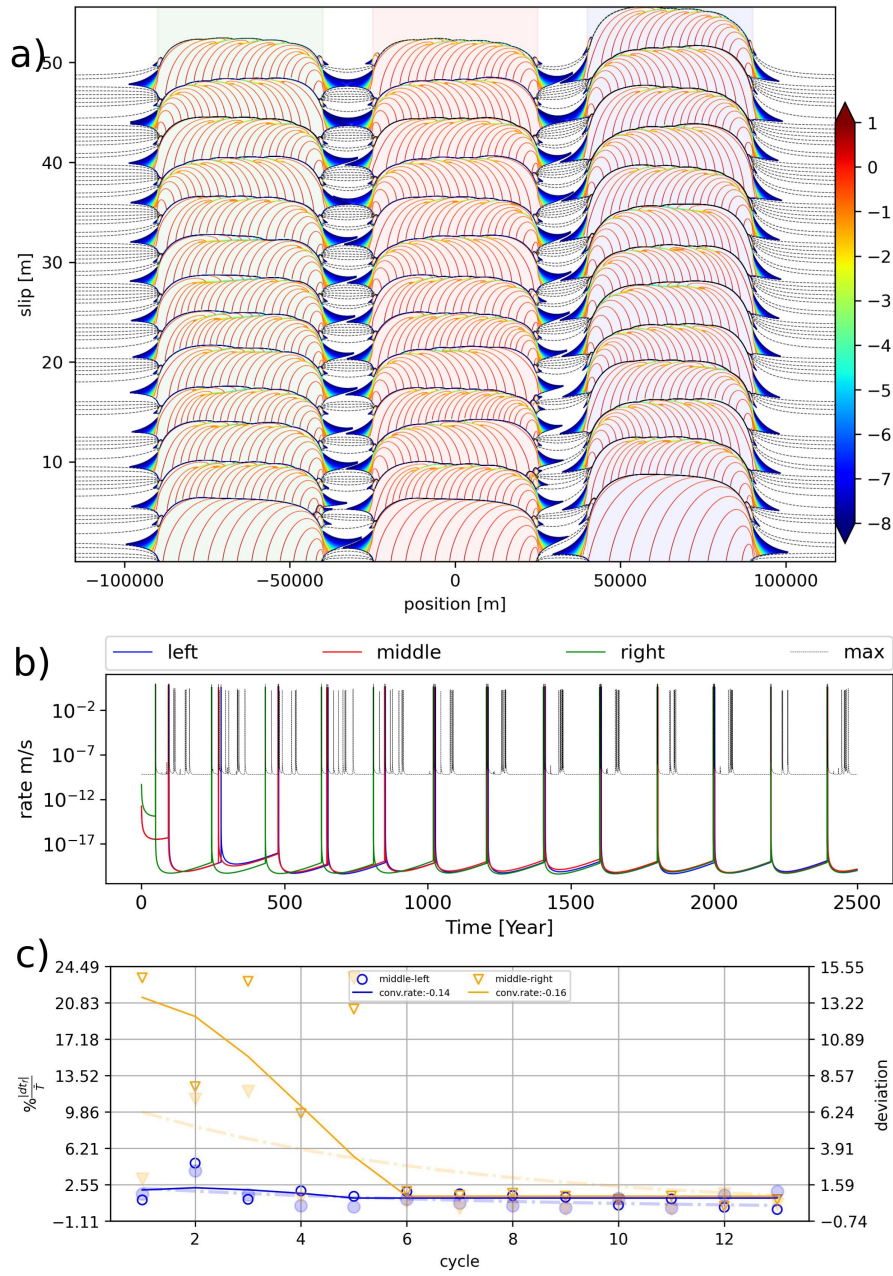


Figure 5.4: A synchronization example using aging law with default parameters in Table 5.1. a) slip profile: slip velocities are plotted in the logarithmic scale defined in the color bar on the right side. The dynamic rupture is plotted in two-second intervals, and post- or pre-seismic events are plotted with scatter plot until they reach a critical value $v_c = 10^{-8} m/s$. The inter-seismic times are plotted with black dashed lines every 20 years interval. b) time series of the middle of each asperity. The colors are given in the legend. c) Synchronization status of adjacent segments. Solid thin lines and scatters without face color denote constraint fit to normalized adjacent segment's failure time differences. The filled color scatters and bold dashed lines denote the deviations from the constraint fit.

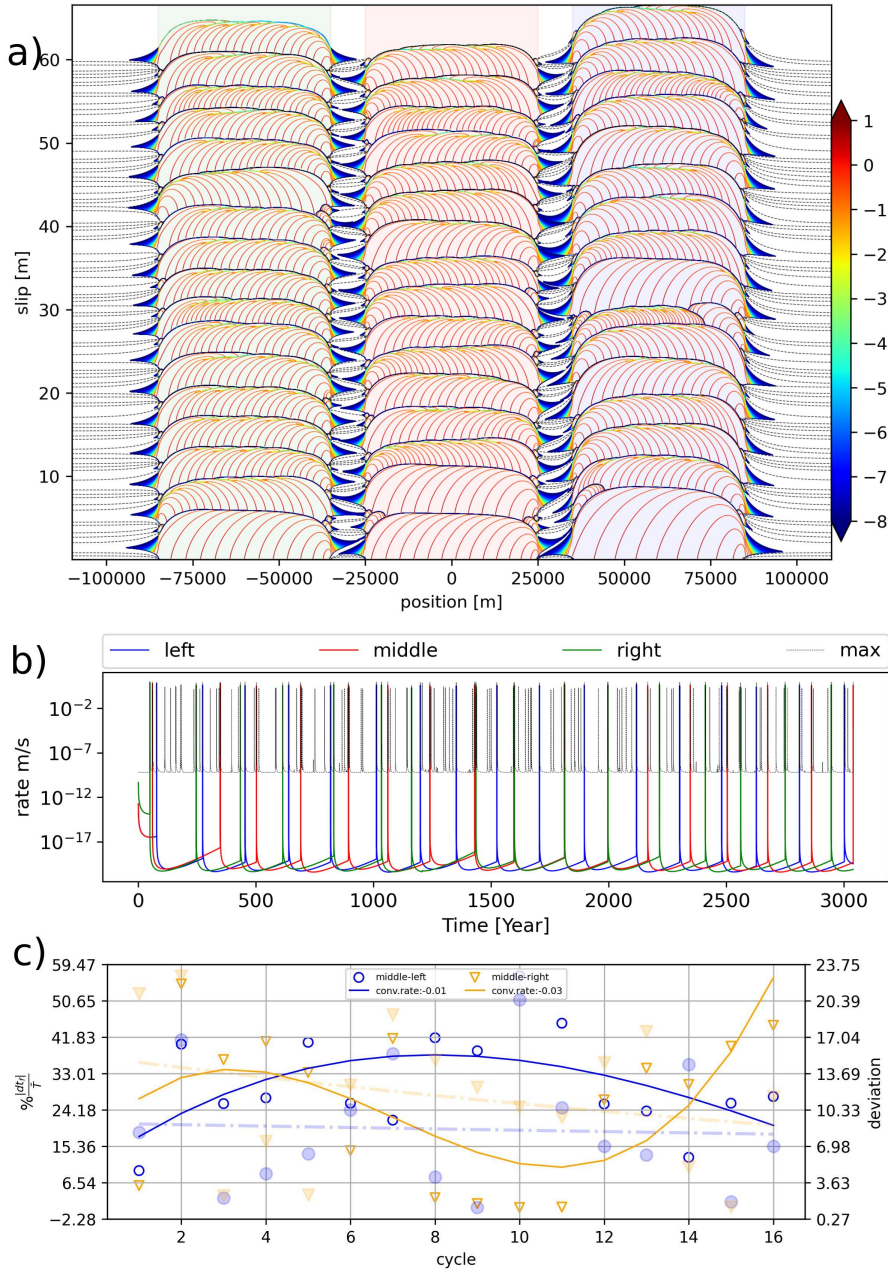


Figure 5.5: A complex example using aging law with default parameters in Table 5.1, except the barrier length decreased to 10km. a) slip profile: slip velocities are plotted in the logarithmic scale defined in the color bar on the right side. The dynamic rupture is plotted in two-second intervals, and post- or pre-seismic events are plotted with scatter plot until they reach a critical value $v_c = 10^{-8} m/s$. The inter-seismic times are plotted with black dashed lines every 20 years interval. b) time series of the middle of each asperity. The colors are given in the legend. c) Synchronization status of adjacent segments. Solid thin lines and scatters without face color denote constraint fit to normalized adjacent segment's failure time differences. The filled color scatters and bold dashed lines denote the deviations from the constraint fit.

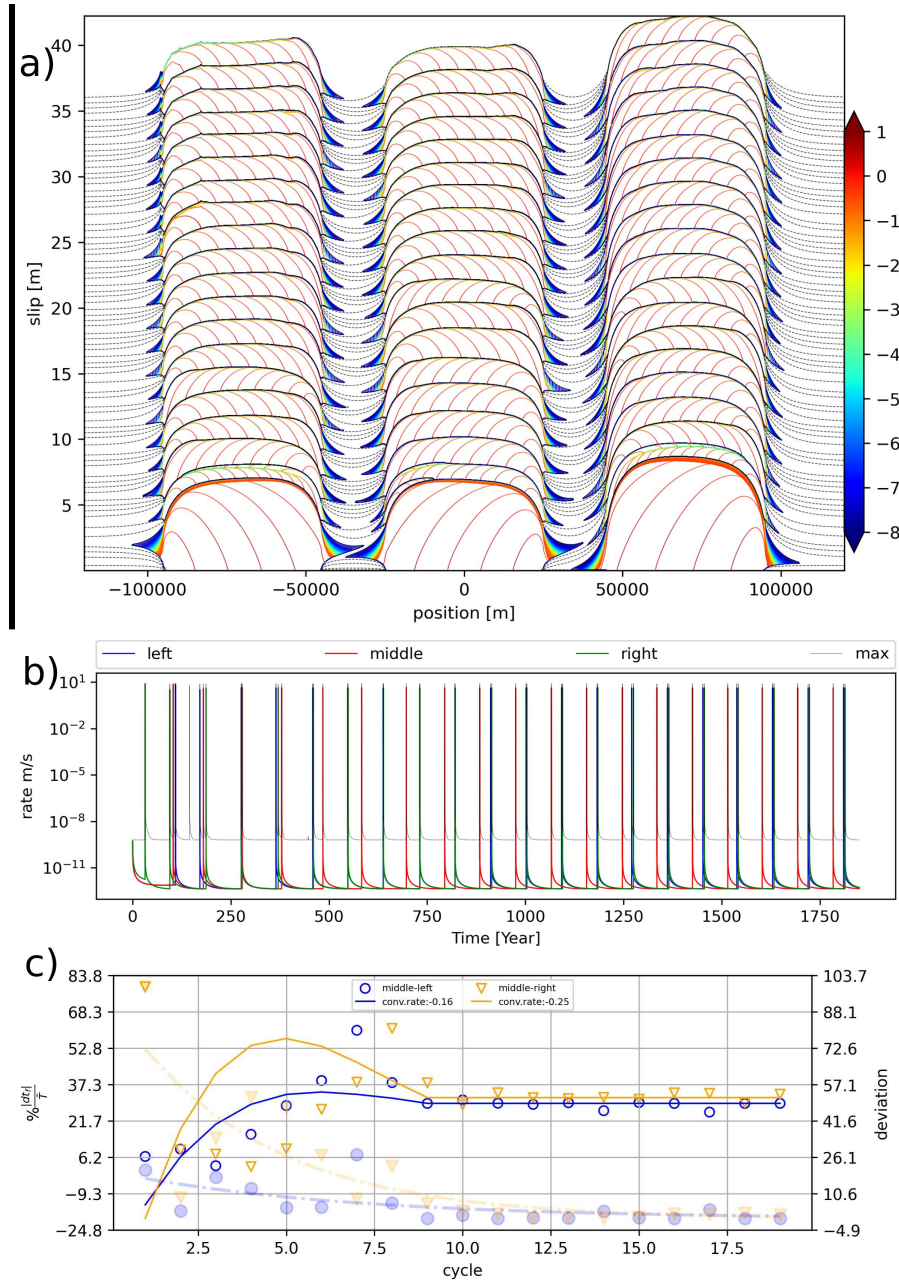


Figure 5.6: An independent status example using slip law with default parameters in Table 5.1, except the barrier length increased to 20 km and $a_{bar} - b = 0.003$. a) slip profile: slip velocities are plotted in the logarithmic scale defined in the color bar on the right side. The dynamic rupture is plotted in two-second intervals, and post- or pre-seismic events are plotted with scatter plot until they reach a critical value $v_c = 10^{-8} m/s$. The inter-seismic times are plotted with black dashed lines every 20 years interval. b) time series of the middle of each asperity. The colors are given in the legend. c) Synchronization status of adjacent segments. Solid thin lines and scatterers without face color denote constraint fit to normalized adjacent segment's failure time differences. The filled color scatterers and bold dashed lines denote the deviations from the constraint fit.

the aging law (Figures 5.3-a and 5.4-a). The aging law sustains quasi-true stationary contact during slow loading with near-zero slip rates and twice the recurrence times and slip amounts per cycle compared to the slip law. The slip profiles (Figures 5.3-a and 5.4-a) also show that the aging law has a longer post-seismic total slip extension (represented by the green to blue colors) compared to the slip law. Additionally, the aging law can produce smaller events at the asperity tips, while the slip law rarely does.

Our results contradict the credited idea that barrier efficiency positively correlates with its size [27, 130]. Decreasing the barrier size from 15 km (as seen in the synchronized example in Figure 5.4) to 10 km disrupts synchronization, leading to the emergence of variable-sized events (as seen in Figure 5.5). Post-slip effects barely reach a neighboring asperity with a 15 km barrier size (as plotted in the slip profiles until slip rates decrease below $10^{-8}m/s$). However, Figure 5.5-a shows that significant after-slip effects can reach the neighbor asperity if the barrier size is 10 km, causing early triggered localized slips that cannot propagate as a full rupture, leaving stress heterogeneity on the asperity, affecting future events and eventually leading to a loss of long-term synchronization. Weakly-coupled asperities better synchronize, but too weakly-coupled asperities cannot synchronize, and the asperities slip independently, as seen in Figure 5.6.

Our simulations show that over-coupling can break synchronization. The aging law has almost twice as strong slip and stress transfers compared to the slip law. However, our results indicate that few simulations using the aging law sustain synchronization, while the slip law is more inclined to synchronization. Figure 5.7 shows that the slip law is more inclined to synchronization, as it is more sensitive to dynamic triggering [92]. Conversely, fewer synchronized examples are observed using the aging law based on the parameters in Table 5.1. If the aging law sustains synchronization, the delay times are either very short or very long compared to the slip law in Figure 5.7.

5.3.2 Sensitivity Analyses

Simulation results in Figures 5.3 to 5.6 display the effect of barrier properties on synchronization behavior. Figure 5.8 examines the impact of barrier length and frictional

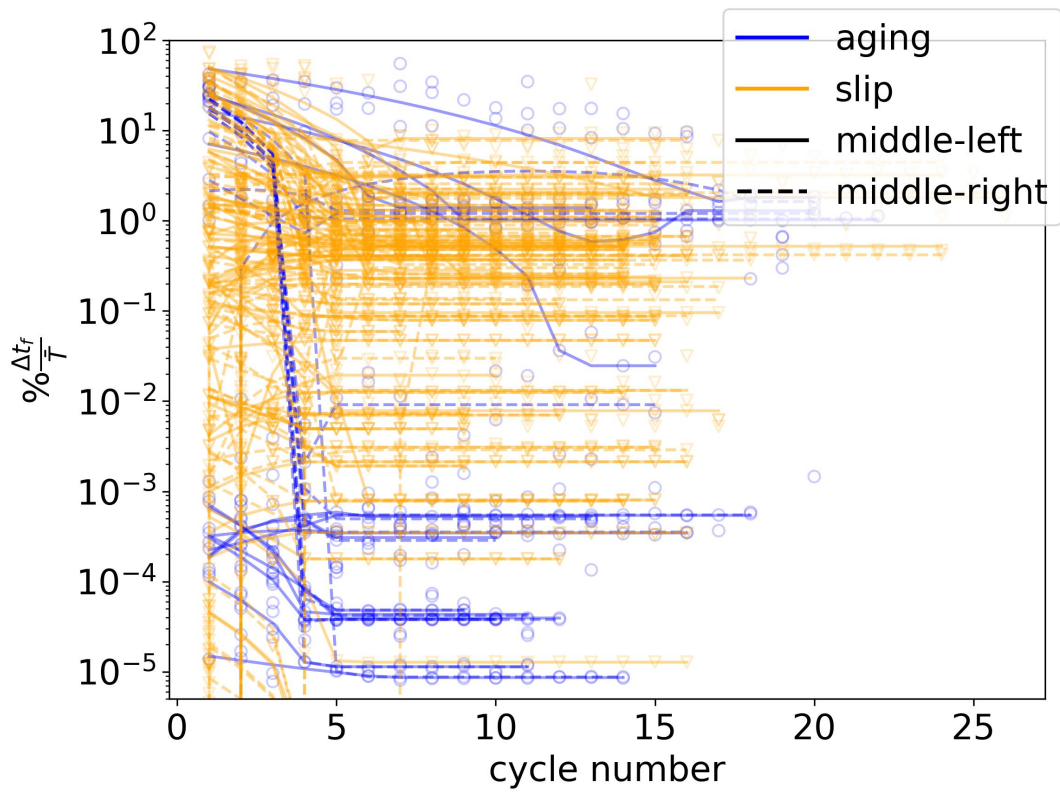


Figure 5.7: Figure showing all examples labeled as "synchronized" in this study. The color and line codes are given in the legend.

strength on synchronization. Two distinct changes in synchronization are observed based on barrier length and frictional strength. The extremely short (5km) and weak barrier ($a_{bar} - b < 0.003$) synchronizes, justifying [137]. For $a_{bar} - b = 0.003$, all cases show the complex distribution for the aging law (Figure 5.8 upper sub-figures). But a further increase to $a_{bar} - b = 0.005$ shifts the synchronization order. In this case, shorter and weaker barriers display complex failures, while longer and stronger barriers synchronize (Figure 5.8 upper-left sub-figure). The slip law (below row in Figure 5.8) typically shows a more synchronized pattern, regardless of the barrier's strength, 5 -10km length barriers always synchronize. Nevertheless, a similar behavior emerges for the slip law if the barrier is extremely weak ($a_{bar} - b = 0$ is set to conditionally stable) and a longer barrier synchronizes (Figure 5.8 lower-right sub-figure, red line), while a shorter barrier (Figure 5.8 lower-right sub-figure, orange line) displays complex ruptures.

Figure 5.9 analyzes the parameters related to asperity. Decreasing the direct velocity effect parameter induces a more prone asperity to trigger. For the aging law (Figure 5.9 upper-left), all simulations display complex failure times as a_{asp} changes for the default barrier strength $a_{bar} - b = 0.003$. However, in the inset Figure 5.9 upper-left, a stronger barrier ($a_{bar} - b = 0.005$ leads to synchronization for lower a_{asp} . A similar pattern emerges for the slip law as well (Figure 5.9 lower-left), the barrier's strength change has a vast impact on the synchronization behavior. The slip law displays a synchronization pattern that the fault zone is more inclined to synchronization as a_{asp} increases. In the inset figure of 5.9 (lower-left), setting a stronger barrier $a_{bar} - b = 0.005$ abruptly changes the synchronization order. In an opposite way to the previous case, the fault zone synchronizes better as a_{asp} decreases. The results on sensitivity to a_{asp} indicate how vital the barrier's frictional strength is.

The critical slip distance d_c (the middle sub-figures of 5.9) displays separate effects on two state laws. The smaller d_c has a smaller nucleation radius R_{inf} , necessitating smaller grids to prevent numerical artifacts. At the same, large earthquakes can nucleate only for the sufficiently large R/R_{inf} , where R is the radius of a 2D circular asperity [129]. Otherwise, large values of R/R_{inf} can lead to partial ruptures, or large values of $R < R_{inf}$ can lead to aseismic creep, despite $a - b > 0$ for the aging law. In our sensitivity analyses, we could not observe a direct influence of d_c on the syn-

chronization using the aging law. However, as shown in the appendix, increasing the d_c generates more variable rupture sizes and types. For example, with $d_c = 24mm$, a rupture can nucleate anywhere on the asperity and propagate bi-laterally. The lower values of d_c nucleate at the VS-VW transition and propagate uni-laterally without a vast difference in the nucleation and propagation pattern. Moreover, the larger d_c also increases the propagation length of post-slip on the barrier, increasing the interaction between the asperities. On the other hand, changes in d_c do not induce a significant change in the slip law, yet higher d_c leads to a smoother failure time difference.

The asperity size L_{asp} (right sub-figures 5.9) displays a weak influence on synchronization. The asperity length is changed from 30km to 100 km using the aging law and shows a deviation after the third or fourth cycle, but their general behaviors do not change. Slip law, however, shows no differences due to asperity length change. These results conflict with the studies, which formulate barrier efficiency with asperity barrier length ratios [27, 130]. In our study, the change in asperity size does not influence the synchronization of the slip law.

Next, we order the convergences in Figure 5.10. The parameters that are sensitive to synchronization are grouped (the horizontal axes of Figure 5.10), and the results are compared for the β_1 parameter, the convergence value, and the converged cycle (the vertical axes of Figure 5.10). According to the exponential model, the convergence is faster and more stable for negative values of β_1 because it deviates less from the fitted model to residuals. The smaller converged value means the failure time difference is shorter, and lower converged cycles indicate a quicker synchronization. Figure 5.10 demonstrates that the slip law sustains a better synchronization than the aging law. The mean converged values (the difference between the full ruptures on the adjacent asperities) are similar for both laws, quite similar unless the barrier is extremely large or strong ($L_{bar} = 20km$, $a_{bar} - b = 0.005$). The first column in Figure 5.10 demonstrates that lower barriers lead to faster synchronization, closer failure times, and higher deviations due to the strong coupling between asperities. Increasing critical slip distance from $d_c = 8mm$ to $d_c = 16mm$ first leads to fewer deviations for both state laws, but a further increase to $d_c = 24mm$ leads to higher deviations. The weaker barrier ($a_{bar} - b$) generally sustains better synchronization. The aging law shows a better synchronization for larger a_{asp} , which leads to a weaker triggering po-

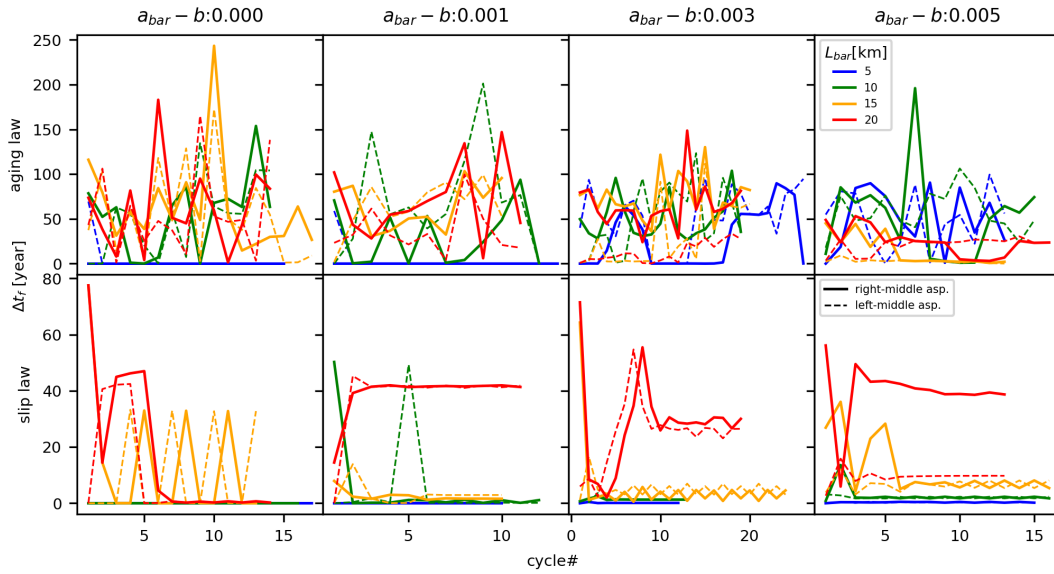


Figure 5.8: Figure shows the effects in barrier length and its frictional properties change on the synchronization. The horizontal and vertical axes are the earthquake cycle and the failure time differences between adjacent asperities. The effects of a change in the barrier’s frictional properties ($a_{bar} - b$) and state types are plotted in vertical and horizontal orders, respectively. The failure time differences between right-middle and left-middle asperities are plotted with solid and dashed lines, and their colors indicate barrier lengths, given in the legends. Unless otherwise stated, the parameters are set to the default values in table 5.1.

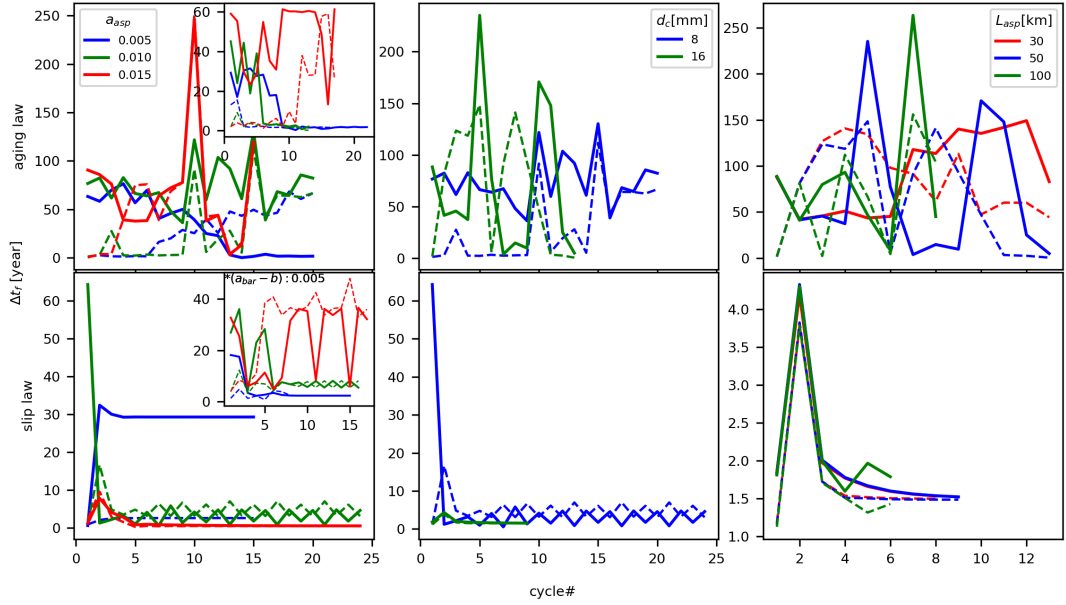


Figure 5.9: Figure shows the effects of asperity's frictional properties, size, and critical slip distance changes on the synchronization. The horizontal and vertical axes are the earthquake cycle and the failure time differences between adjacent asperities. The effects of a change in the asperity's direct velocity effect parameter a_{asp} , critical slip distance d_c , and asperity length L_{asp} are plotted vertically for aging and state laws, respectively. The failure time differences between right-middle and left-middle asperities are plotted with solid and dashed lines, and changes in parameters are plotted with different colors, given in the legends. The barrier's frictional property is set to $a_{bar} - b = 0.003$ as default in this figure. In inset figures, this parameter is set to $a_{bar} - b = 0.005$. The rest of the parameters are set to the default values in table 5.1.

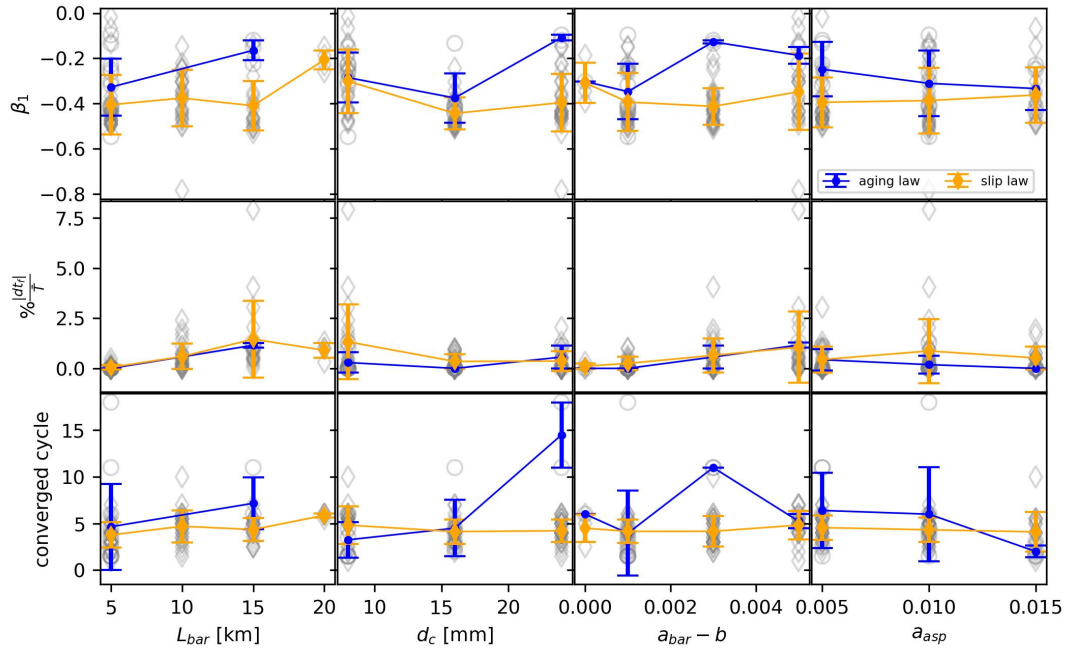


Figure 5.10: The plot shows how fast the faults are synchronized with changing certain parameters. The so-called convergence rates (β_1 of fitted deviance) are plotted on the top. The middle row shows the converged values, defined by the failure time differences in percentage between two successive large earthquakes of adjacent faults normalized by mean recurrence time. The lower row is the converged cycle defined, after which cycle faults synchronize.

tential. On the other hand, the slip law shows less significance in its synchronization rate to the asperity's frictional properties.

5.3.3 The roles of static and dynamic triggering

Figure 5.11 displays the five full rupture events on the middle asperity and their propagation over time. The state laws differ significantly during co-seismic ruptures but resemble each other in the post-seismic phase. The aging law results in twice as much stress on the barrier as the slip law. Hence, the aging law lasts longer along the barrier and increases the chance of post-slip waves reaching the next asperity compared to the slip law. The pattern suggests that post-slip travels as a wave, much slower than the co-seismic wave, and slowly fades within the barrier and stabilizes stress. Close ruptures can amplify each other during propagation over the barrier, leading to longer post-seismic effects.

Figure 5.12 shows that larger magnitude waves result in complex ruptures. Three full ruptures on the middle asperity for both laws with different synchronization statuses demonstrate that larger stress loads lead to more complex ruptures. The propagation on the asperity is the same, but stress waves on the barriers for complex cases are several orders of magnitude higher than in the synchronized case.

Asperities surrounded by barriers may not sustain synchronization through static triggering but rather through transient triggering from stress loads and relaxation oscillation. Our simulations show that a coupling relationship takes place as the barrier stabilizes. The post-slip waves reaching the next asperity can change its state and trigger an early failure. Strong barriers reduce the amplitude of post-slip waves, leading to independent occurrences. On the other hand, if the barrier is too strong, it won't affect the state enough, resulting in independent occurrences.

5.3.4 Indicator of synchronization and predictability of large earthquakes

Our simulation results indicate that peak ground velocity (PGV) values are a predictor of fault synchronization. Higher PGV values indicate a higher likelihood of

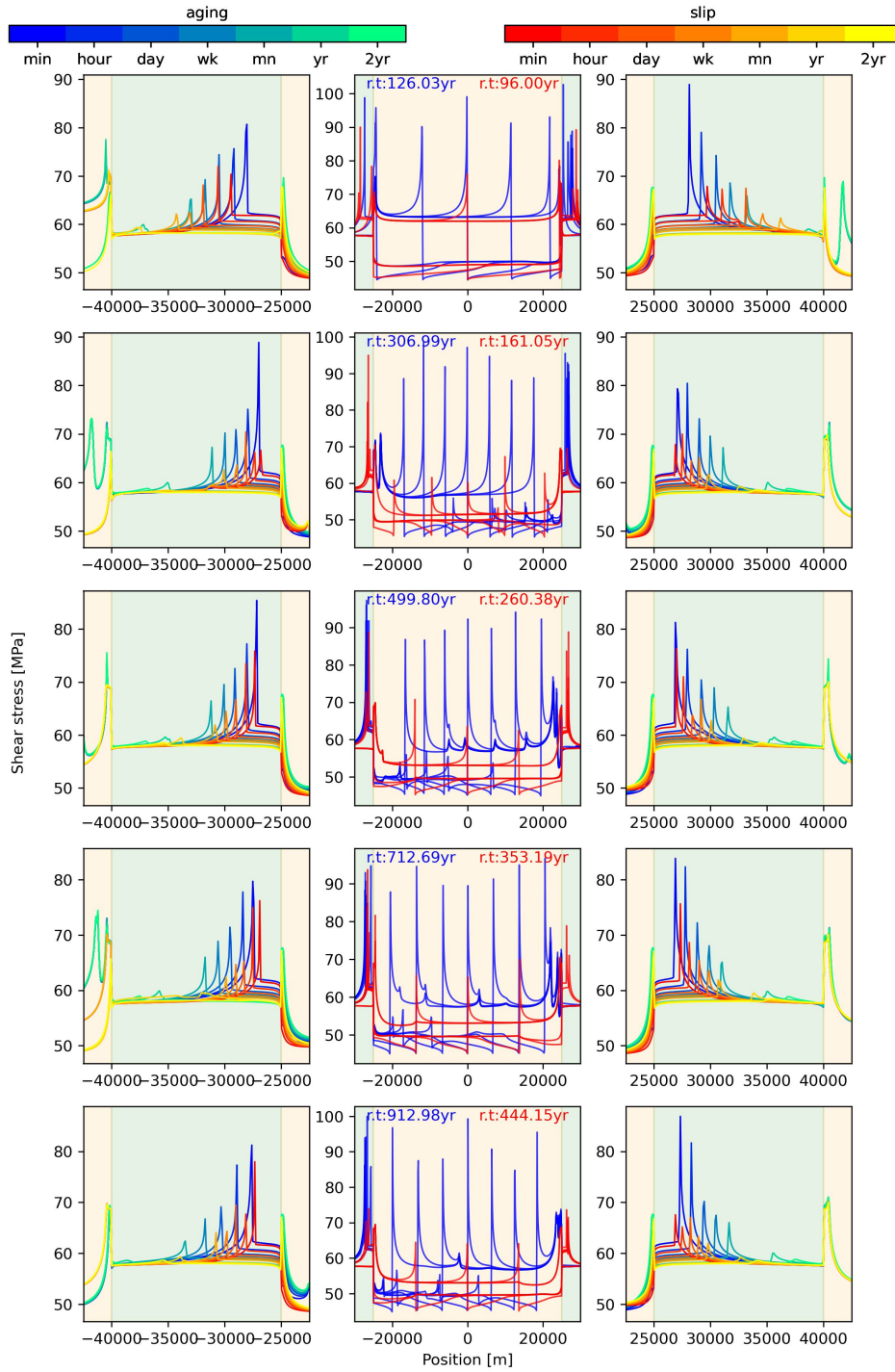


Figure 5.11: 5 full successive full ruptures and post-seismic propagation of middle asperity are plotted. The default parameters in table 5.1 are used, except $a_{bar} - b = 0.003$. On the left and right, the propagation on the barrier is plotted with colored lines that define the time and state law, given in the color bar. In the middle subplots, the propagation on the middle asperity is plotted with 5 seconds intervals. Rupture times are written in the middle plot for each state law with the color code defined in the color bar.

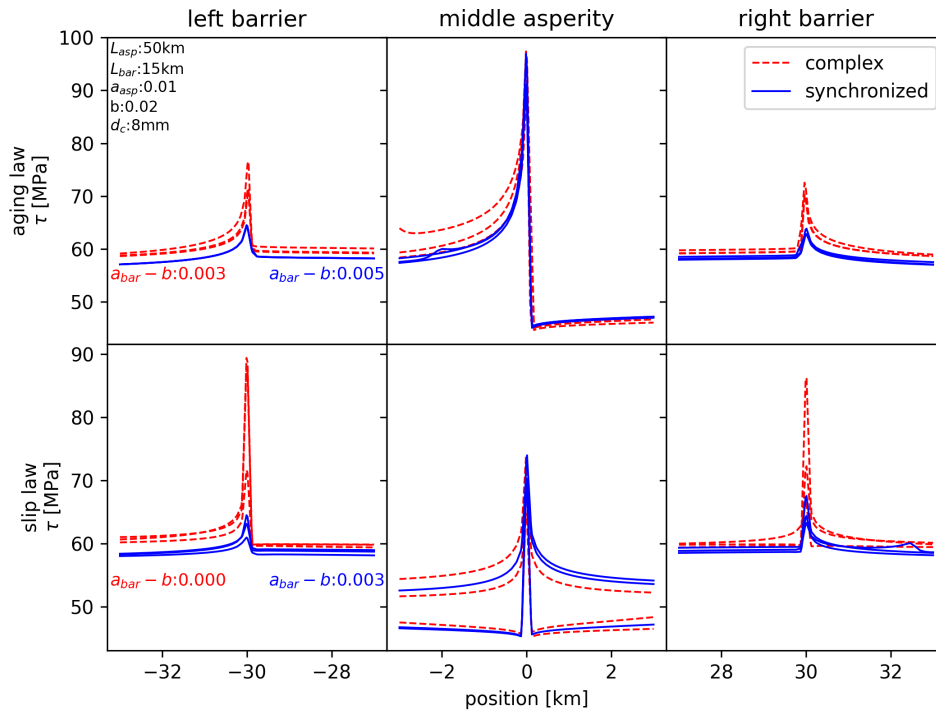


Figure 5.12: The stress propagation of complex and synchronized simulations are plotted for full ruptures on the middle asperity and continuation on the left and right barrier. The plotted waves correspond to the highest amplitudes of the first-fourth ruptures on the middle asperity and 5km away from it. The parameters for simulation are written on the first sub-plot (upper-left) and plotted with a color code for the synchronization status given in the legend. For both aging and slip law, complex and synchronized status simulations correspond to different $a_{bar} - b$ values given in the first column.

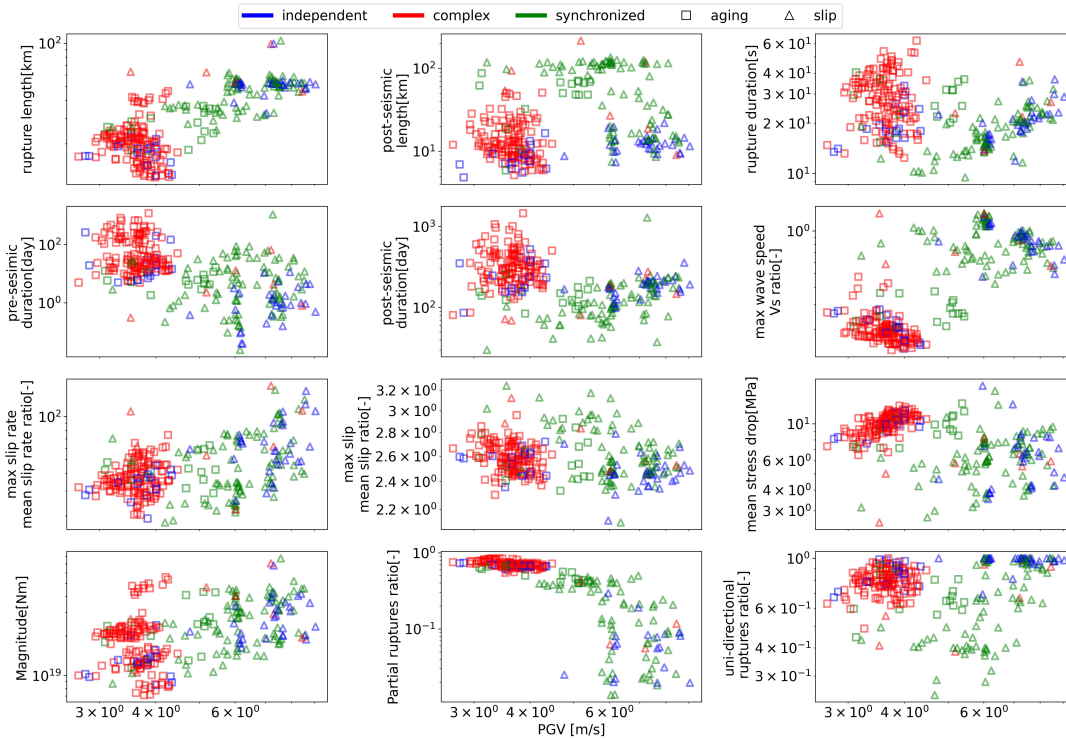


Figure 5.13: Distribution stats of slip event vs Peak Ground Velocity (PGV)

synchronization and predictability, especially in heterogeneous stress conditions that weaken slip rates and propagation speed. Another promising indicator is the length of post-seismic deformation, as longer deformations suggest a coupling between asperities. Distinct or weakly coupled faults may also have high slip rates and propagation speeds, but their post-slip waves do not overlap and fade faster. Tracking post-seismic deformation is, therefore, a valuable tool for evaluating seismic risk.

5.4 Discussion On Synchronization

We analyzed three strong asperities interaction mechanisms in many possible scenarios. The setups are specifically decided to be analogous to the North Anatolian Fault (NAF) zone. Nevertheless, results will also shed light on other major fault zones similar to NAF.

5.4.1 The State laws

The simulation results suggest that the dynamics of the applied state law significantly influence fault synchronization. The slip law shows a higher inclination to synchronization compared to the aging law. This can be attributed to the slip law's ability to propagate with lower fracture energy [138], and its linear dependence on the slip rate increases triggering potential [36]. On the other hand, the aging law generates higher amplitude triggering signals and leads to more variable-sized complex failures, resulting in less synchronized events. However, both state laws have their own advantages and limitations, and the question of which is more suited to nature remains open. Further laboratory studies are needed.

5.4.2 Static or Transient triggering?

Our results disagree with the failure models such that static stress changes increase the stress and lead to synchronization [38]. Firstly, our simulations point to a transient-like triggering mechanism rather than a coulomb-like static stress increase. We could not explore the cases in which the rupture on an asperity jumps over the barrier with a small loss of its strength and is arrested within the asperity. In most of our examples, the stress on the asperity is released in tens of seconds, and the waves weaken on the barrier with several orders longer time scale. Sometimes, the post-slip waves reach the next asperity and permanently alter the state of the hitting edge. That section of the asperity is generally the nucleation point of the next asperity. But such static-type effects do not lead to synchronization, in contrast, they lead to more complex failure time distribution.

5.4.3 Sensitive parameters

The stress transfer through the post-seismic relaxation waves to the neighbor asperity depends on the barrier's size and properties. The long and strong barriers prevent segment coupling between asperities, and more quasi-periodic characteristic independent earthquakes are observed. The barriers that allow large stress transfer (either small $a_{bar} - b$ or short barrier size) lead to variable-sized events with complex failure times.

The stress transfer via post-slip waves should be neither too strong nor too weak to sustain large fault synchronization. [137] concluded that the barrier's size is more effective than its strength. However, our results indicate the opposite. Figure 5.9 demonstrate how changing the barrier's $a - b$ parameter significantly alters the synchronization behavior. On the other hand, the barrier's length has a linear influence on synchronization.

Secondly, the direct velocity effect parameter a controls the synchronization process. We consider two distinct processes of a affecting the fault zone to account for this two-fold. First, lower values of a_{asp} cause weaker resistance to velocity changes at the asperity, increasing dynamic triggering sensitivity. Second, higher values of a_{bar} increase the stress or velocity response on the barrier [33]. The larger the response, the longer it takes to resettle.

Third, sensitivity to critical slip distance d_c change shows complicated simulation results. The nucleation radius depends strongly on critical slip distance, which is the most ambiguous parameter. The change in d_c can lead to drastically different nucleation and propagation pattern. We observed more jumping rates over the barrier if d_c is large enough and nucleation could be anywhere along the VW zone for the aging law. Oppositely lower d_c leads to smaller localized events at the VW-VS transition zone. We did not observe such deviance using the slip law. Further simulations and laboratory studies are needed for this issue. Also, simulations with smaller critical slip distances complying with the laboratory values [33] increases the CPU time significantly, which restrains the typical values for simulations several orders higher.

Fourth, the length of asperity does not show a sensitivity to synchronization. We tested 30,50 100 km of asperities, and after 8 successive cycles, they do not deviate significantly (Figure 5.9) for the slip law. The aging law with different asperity sizes starts deviating after the third and fourth cycles, which could also be an account for the accumulation of numerical errors. The studies considered the asperity barrier size an important parameter to quantify barrier efficiency [27, 130, 131]. However, we do not observe a significant impact by increasing the asperity size from 50km to 100km or decreasing it to 30 km. We reasonably argue that the asperity size does not affect synchronization, at least for our simulation setup.

5.4.4 Observable Indicators for synchronization and predictability of large Earthquakes

Generally, independent faults generate higher amplitude slip and slip rates in our simulations. Coupled faults' slip/rates are lower because of interaction; asperities may be forced to fail earlier, generating smaller earthquakes than their potential. Faults forced to fail earlier can also generate a slip deficit, leading to wave speeds and magnitude deviation during the rupture. The stronger the deviation is, the more complex and unpredictable the large earthquakes become. According to our analyses, the "synchronized" labels lay between these complex and independent labels (see Figure 5.13). Our inference from the simulations is that the frictional parameters and barrier sizes generating over-coupling or too-weak coupling lead to either complex or independent type synchronization.

The mean rupture wave speed and slip-rate amplitudes are the most obvious observable in separating complex and other types of status (synchronized/independent). The propagation speed at the asperity highly deviates depending on the slip deficit. The propagation speed exceeds shear wave speed on the spatially smooth faults (similar stress level along the asperity), showing super-shear examples. The duration and extent of the post-seismic slip are also valuable indicators to separate further independent and synchronized type status. This information can easily be tested in nature, but the topic is beyond our scope, and we leave it for a further follow-up study.

5.4.5 Simplified inertial effects on numerical simulations

Here a question may arise regarding the simplified inertial effects. The numerical simulations with full inertial effects lead to faster wave propagation and higher amplitude slip rates [23, 24, 139]. Including such effects generates similar results, which we suggest as indicators for earthquake synchronization. We look through the inclusion of full inertial effects using type three kernel [22] by applying a double half-step adaptive time-stepping algorithm [139]. The simulation results in the supplementary figure do not show full inertial effects leading to better synchronization; instead, more partial ruptures emerge. Increasing slip rates, rupture speeds, and narrowing down

the cohesive zone through applying full inertial effects will not change its intrinsic "over-coupling" nature and prevent generating variable-sized slip events for the aging law. Thus, it will not change our conclusion on the framework of large earthquake synchronization either.

5.5 Implications On NAF

We identified three locations where most large earthquakes nucleate, or arrest can act as a barrier in Figure 5.14. First, we discuss the Main Marmara Fault (MMF), where a large earthquake is expected soon (Figure 5.14(b)- MMF: solid red line). The previous M7.4 (17.08.1999) devastating earthquake stopped at the border of this highlighted section (yellow circle in Figure 5.14(b)). A normal mechanism fault ties the endpoint of the last large M7.4 earthquake and fault segment that exhibits a seismic gap argued to be the next large earthquake that will hit the metropolitan city of Istanbul. This normal mechanism fault segment's length exceeds 30 km and accounted for the failure time discreteness along NAF [56, 16].

The next highlighted section is where progressive west-migrating earthquakes between 1939-1444 stopped (Figure 5.14(c)). M7.4 Izmit earthquake ruptured (left side at Figure 5.14(c) panel) on 17.08.1999, approximately three months later, M7.2 Duzce (12.11.1999) earthquake ruptured, showing an explicit example of delayed triggering. However, studies often fail to explain the three months of late triggering using co-seismic static stress change based Coulomb model [140]. The velocity strengthening visco-elastic afterslip mechanism is more agreeable [141, 140, 142], supporting our simulation results.

Finally, we highlight the section where the M7.8 Erzincan (1939) and M7.1 Erbaan-Niksar (1942) earthquakes are separated with approximately 10km long releasing step-over [19]. This section of NAF also served as a barrier to at least four historical earthquakes in 1035, 1254, 1666-1668, and 1939-1942 [143, 19].

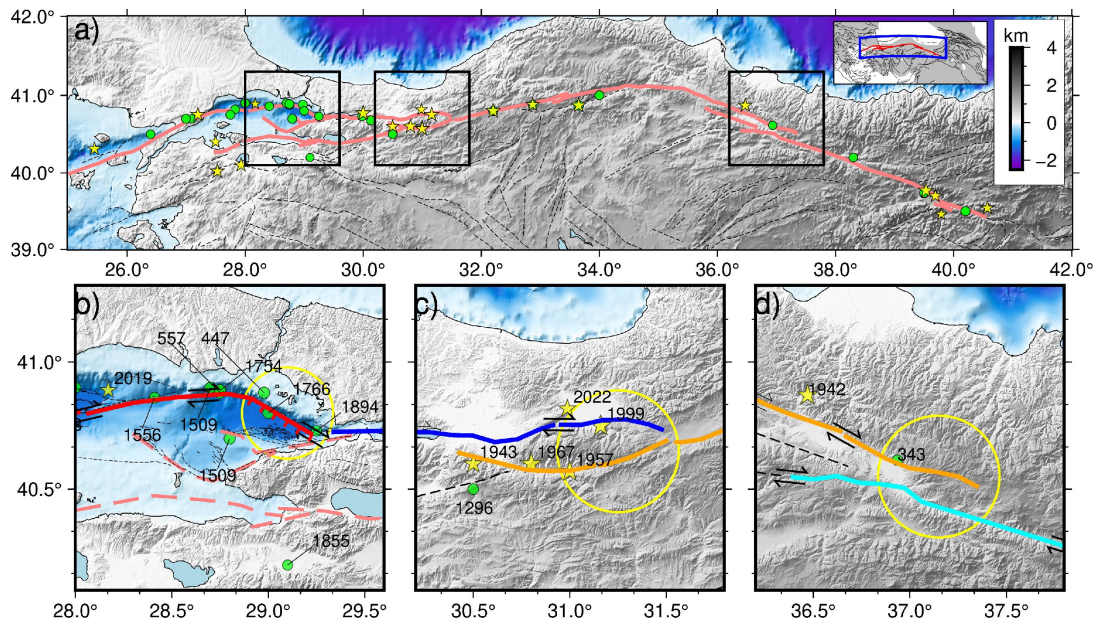


Figure 5.14: The Map (a) shows the synchronized segments along NAF in different color codes, and historical earthquakes on it (green circles) and most recent earthquakes (Time>1900) with the yellow stars. The segment boundaries are highlighted with a black frame on map (a) and plotted on a larger scale in b-d. The possible barriers are highlighted in the large yellow circles in subplots b-d.

5.6 Conclusion

Motivated by the synchronized historical pattern along North Anatolian Fault (NAF) Zone, we investigated the fault synchronization on a physics-based asperity-barrier model in the rate and state friction (RSF) framework. Even though the model lacks depth information and is necessarily conceptual, results point to many aspects of NAF. The sensitivity analyses reveal that to sustain a long-term synchronization pattern, i.e., NAF, the stress interaction between asperities should be neither over-coupled nor too weakly coupled. Here the barrier's strength has a vital role and can vastly change the synchronization pattern. Besides, the barrier's size and the direct velocity effect parameter in the framework of RSF play a key role. We observed no relevance of asperity barrier size to fault synchronization, at least for our simulation setup, which is often proposed for barrier efficiency approximations. Over 27000 simulation results suggest longer duration, and extensions of after-slips account for the coupling between asperities, which is observable in nature. The synchronized faults tend to generate higher slip rates and rupture speeds, but they are irrelevant to the magnitudes of earthquakes. The outcome of this study paves the way to investigate the observable indicators in nature so the predictability of earthquakes.

CHAPTER 6

CONCLUSION

This study aims to reveal the triggering and stress transfer process of earthquakes. The results help to quantify the seismic risk assessments, in such a way that after a rupture process how the surrounding faults are affected and is it possible to quantify the next rupture's failure delay. Moreover when the faults behave coupled, so that the failure times are quasi-regular and they are more predictable.

First of all, the mechanism of the triggering process is analyzed with analytical and numerical method by considering several state evolution formula within the framework of rate and state friction. Results indicate how the response of the state laws can differ, explaining the contradictory results on earthquake triggering studies. The analytical and numerical results are in a good agreement and reveal that the process is mainly controlled by asperity patch size, direct velocity effect parameter, and effective normal stress. The rest of the fault parameters are not significantly sensitive. Also, the peak ground velocities and the frequency are important to quantify an earthquake's triggering potential. Our analytical formulation reveals well the mechanism under certain conditions. Yet, the relation should be validated with a real data for further studies. Finally, we reasonably favor Ruina law, because of doing a better job in the real case scenarios.

Secondly, the possible triggering scenarios of the moderate M5.8 earthquake that was ruptured in the vicinity of Marmara fault is analyzed. The conclusion is that the moderate earthquake was not strong enough to induce an instant triggering but brought the locked fault closer to failure. Many studies agree that the time left to a large earthquake within this segment is likely to be less than a few decades (e.g., [55, 95]). Within this time window, realistic simulations utilizing Ruina state law

which favors earthquake triggering resulted in greater failure time advance (exceeding one year) than the conventional Coulomb failure model.

Thirdly the off-fault delayed triggered aftershocks of the M7.0 Samos rupture was analyzed using a normal-shear stress coupling relation. The results show, two distinct time regimes that, when weakening term is not activated and a healing process at the fault interface prevails, a shear-normal stress coupling effect increase the failure time, suggesting a higher triggering potential. Otherwise the induced clock advances resemble each other. The possible fault mechanisms are analyzed in the study. The results can mimic both instant and delay triggering of earthquakes with $M_w \leq 4$ after the Samos earthquake. Faults adjacent to the rupture are more likely to trigger, particularly the NE-SW trending strike-slip fault bounding the Ikaria Island from the West, producing a large earthquake. In contrast, faults near İzmir remain unaffected by the dynamic triggering of the Samos Earthquake.

Finally, the long term faults interactions are analyzed using a continuum formulation using spectral boundary integral method, for which the shear stress is assumed to be rate and state friction. Motivated by the historical synchronized pattern along North Anatolian Fault (NAF) Zone, the investigation of fault synchronization on a physics-based asperity-barrier model points to many aspects of fault stress transfer coupling. The sensitivity analyses reveal that to sustain a long-term synchronization pattern, i.e., NAF, the stress interaction between asperities should be neither over-coupled nor too weakly coupled. Therefore the barrier's size and frictional properties with direct velocity effect parameter in the framework of RSF play a key role. We observed no relevance of asperity barrier size to fault synchronization, at least for the simulation setup, which is often proposed for barrier efficiency approximations. Over 27000 simulation results suggest longer duration and extensions of after-slips account for the coupling between asperities, which is observable in nature. The synchronized faults tend to generate higher slip rates and rupture speeds, but they are irrelevant to the magnitudes of earthquakes. The outcome of this study paves the way to investigate the observable indicators in nature so the predictability of earthquakes.

REFERENCES

- [1] J. Gomberg, M. L. Blanpied, and N. Beeler, “Transient triggering of near and distant earthquakes,” *Bulletin of the Seismological Society of America*, vol. 87, no. 2, pp. 294–309, 1997.
- [2] H. Karabulut, S. E. Güvercin, F. Eskiköy, A. Ö. Konca, and S. Ergintay, “The moderate size 2019 september m w 5.8 silivri earthquake unveils the complexity of the main marmara fault shear zone,” *Geophysical Journal International*, vol. 224, no. 1, pp. 377–388, 2021.
- [3] X. Le Pichon, B. M. D. Lepinay, B. Meyer, R. Armijo, N. Go, R. Saatc, and B. Tok, “The active Main Marmara Fault,” *Earth and Planetary Science Letters*, vol. 192, 2001.
- [4] X. Le Pichon, N. Chamot-Rooke, C. Rangin, and A. M. C. Sengör, “The North Anatolian fault in the Sea of Marmara,” *Journal of Geophysical Research: Solid Earth*, vol. 108, no. B4, pp. 1–20, 2003.
- [5] R. Tibi, G. Bock, Y. Xia, M. Baumbach, H. Grosser, C. Milkereit, S. Karakisa, S. Zünbül, R. Kind, and J. Zschau, “Rupture processes of the 1999 august 17 izmit and november 12 düzce (turkey) earthquakes,” *Geophysical Journal International*, vol. 144, no. 2, pp. F1–F7, 2001.
- [6] M. E. Aksoy, M. Meghraoui, M. Vallée, and Z. Çakır, “Rupture characteristics of the ad 1912 mürefte (ganos) earthquake segment of the north anatolian fault (western turkey),” *Geology*, vol. 38, no. 11, pp. 991–994, 2010.
- [7] A. Kiratzi, C. Papazachos, A. Özacar, A. Pinar, C. Kkallas, and E. Sopaci, “Characteristics of the 2020 samos earthquake (aegean sea) using seismic data,” *Bulletin of Earthquake Engineering*, pp. 1–23, 2021.
- [8] E. Altunel and A. Pinar, “Tectonic implications of the mw 6.8, 30 october

- 2020 kuşadası gulf earthquake in the frame of active faults of western turkey,” *Turkish Journal of Earth Sciences*, vol. 30, no. 4, pp. 436–448, 2021.
- [9] S. Pavlides, T. Tsapanos, N. Zouros, S. Sboras, G. Koravos, and A. Chatzipetros, “Using active fault data for assessing seismic hazard: a case study from the aegean sea, greece,” in *Earthquake geotechnical engineering satellite conference XVIIIth international conference on soil mechanics & geotechnical engineering*, vol. 10, p. 2009, 2009.
- [10] R. Basilic, V. Kastelic, M. Demircioglu, D. Garcia Moreno, E. Nemser, P. Petricca, S. Sboras, G. Besana-Ostman, J. Cabral, T. Camelbeeck, *et al.*, “The european database of seismogenic faults (edsf) compiled in the framework of the project share,” 2013.
- [11] B. Uzel, H. Sözbilir, Ç. Özkaymak, N. Kaymakçı, and C. G. Langereis, “Structural evidence for strike-slip deformation in the izmir–balıkesir transfer zone and consequences for late cenozoic evolution of western anatolia (turkey),” *Journal of Geodynamics*, vol. 65, pp. 94–116, 2013.
- [12] Ö. Emre, T. Y. Duman, S. Özalp, F. Şaroğlu, Ş. Olgun, H. Elmacı, and T. Çan, “Active fault database of turkey,” *Bulletin of Earthquake Engineering*, vol. 16, no. 8, pp. 3229–3275, 2018.
- [13] N. Beeler and D. Lockner, “Why earthquakes correlate weakly with the solid earth tides: Effects of periodic stress on the rate and probability of earthquake occurrence,” *Journal of Geophysical Research: Solid Earth*, vol. 108, no. B8, 2003.
- [14] A. M. Şengör, O. Tüysüz, C. Imren, M. Sakiñ, H. Eyidoğan, N. Görür, X. L. Pichon, and C. Rangin, “The north anatolian fault: A new look,” *Annual Review of Earth and Planetary Sciences*, vol. 33, pp. 37–112, 2005.
- [15] F. Bulut and A. Doğru, “Time frame for future large earthquakes near İstanbul based on east-to-west decelerating failure of the north anatolian fault,” *Turkish Journal of Earth Sciences*, vol. 30, no. 2, pp. 204–214, 2021.
- [16] N. Pondard, R. Armijo, G. C. P. King, B. Meyer, and F. Flerit, “Fault interactions in the Sea of Marmara pull-apart (North Anatolian Fault): earthquake

clustering and propagating earthquake sequences,” *Geophysical Journal International*, vol. 171, pp. 1185–1197, oct 2007.

- [17] J. Fraser, J. S. Pigati, A. Hubert-Ferrari, K. Vanneste, U. Avsar, and S. Altinok, “A 3000-Year Record of Ground-Rupturing Earthquakes along the Central North Anatolian Fault near Lake Ladik, Turkey,” *Bulletin of the Seismological Society of America*, vol. 99, pp. 2681–2703, oct 2009.
- [18] T. Parsons, “Recalculated probability of $m \geq 7$ earthquakes beneath the sea of marmara, turkey,” *Journal of Geophysical Research: Solid Earth*, vol. 109, pp. 1–21, 2004.
- [19] C. Zabcı, H. S. Akyüz, V. Karabacak, T. Sançar, E. Altunel, H. Gürsoy, and O. Tatar, “Palaeoearthquakes on the Kelkit Valley segment of the North Anatolian Fault, Turkey: Implications for the surface rupture of the historical 17 august 1668 Anatolian earthquake,” *Turkish Journal of Earth Sciences*, vol. 20, pp. 411–427, jan 2011.
- [20] Y. Finzi and S. Langer, “Damage in step-overs may enable large cascading earthquakes,” *Geophysical Research Letters*, vol. 39, pp. n/a–n/a, aug 2012.
- [21] “Large earthquake triggering, clustering, and the synchronization of faults,” *Bulletin of the Seismological Society of America*, vol. 100, pp. 901–909, 2010.
- [22] N. Lapusta, J. R. Rice, Y. Ben-Zion, and G. Zheng, “Elastodynamic analysis for slow tectonic loading with spontaneous rupture episodes on faults with rate- and state-dependent friction,” *Journal of Geophysical Research: Solid Earth*, vol. 105, no. B10, pp. 23765–23789, 2000.
- [23] M. Y. Thomas, N. Lapusta, H. Noda, and J. P. Avouac, “Quasi-dynamic versus fully dynamic simulations of earthquakes and aseismic slip with and without enhanced coseismic weakening,” *Journal of Geophysical Research: Solid Earth*, vol. 119, pp. 1986–2004, 2014.
- [24] V. Lambert and N. Lapusta, “Resolving simulated sequences of earthquakes and fault interactions: Implications for physics-based seismic hazard assessment,” *Journal of Geophysical Research: Solid Earth*, vol. 126, 10 2021.

- [25] V. Lambert, N. Lapusta, and S. Perry, “Propagation of large earthquakes as self-healing pulses or mild cracks,” *Nature*, vol. 591, pp. 252–258, mar 2021.
- [26] N. Kato, “Interaction of slip on asperities: Numerical simulation of seismic cycles on a two-dimensional planar fault with nonuniform frictional property,” *Journal of Geophysical Research: Solid Earth*, vol. 109, pp. 1–17, 2004.
- [27] Y. Kaneko, J.-P. Avouac, and N. Lapusta, “Towards inferring earthquake patterns from geodetic observations of interseismic coupling,” *Nature Geoscience*, vol. 3, pp. 363–369, 2010.
- [28] P. Dublanchet, P. Bernard, and P. Favreau, “Interactions and triggering in a 3-d rate-and-state asperity model,” *Journal of Geophysical Research: Solid Earth*, vol. 118, pp. 2225–2245, 2013.
- [29] J. H. Dieterich, “Modeling of rock friction 1. experimental results and constitutive equations,” *Journal of Geophysical Research: Solid Earth*, vol. 84, pp. 2161–2168, 5 1979.
- [30] A. Ruina, “Slip instability and state variable friction laws.,” *Journal of Geophysical Research*, vol. 88, pp. 10359–10370, 12 1983.
- [31] G. Perrin, J. R. Rice, and G. Zheng, “Self-healing slip pulse on a frictional surface,” *Journal of the Mechanics and Physics of Solids*, vol. 43, no. 9, pp. 1461–1495, 1995.
- [32] K. Nagata, M. Nakatani, and S. Yoshida, “A revised rate-and state-dependent friction law obtained by constraining constitutive and evolution laws separately with laboratory data,” *Journal of Geophysical Research: Solid Earth*, vol. 117, no. B2, 2012.
- [33] C. Marone, “Laboratory-derived friction laws and their application to seismic faulting,” *Annual Review of Earth and Planetary Sciences*, vol. 26, no. 1, pp. 643–696, 1998.
- [34] J. Dieterich, “A constitutive law for rate of earthquake production and its application to earthquake clustering,” *Journal of Geophysical Research: Solid Earth*, vol. 99, no. B2, pp. 2601–2618, 1994.

- [35] J.-P. Ampuero and A. M. Rubin, “Earthquake nucleation on rate and state faults—aging and slip laws,” *Journal of Geophysical Research: Solid Earth*, vol. 113, no. B1, 2008.
- [36] M. Nakatani, “Conceptual and physical clarification of rate and state friction: Frictional sliding as a thermally activated rheology,” *Journal of Geophysical Research: Solid Earth*, vol. 106, no. B7, pp. 13347–13380, 2001.
- [37] G. C. King, R. S. Stein, and J. Lin, “Static stress changes and the triggering of earthquakes,” *Bulletin of the Seismological Society of America*, vol. 84, no. 3, pp. 935–953, 1994.
- [38] R. S. Stein, A. A. Barka, and J. H. Dieterich, “Progressive failure on the north anatolian fault since 1939 by earthquake stress triggering,” *Geophysical Journal International*, vol. 128, no. 3, pp. 594–604, 1997.
- [39] D. Kilb, J. Gomberg, and P. Bodin, “Triggering of earthquake aftershocks by dynamic stresses,” *Nature*, vol. 408, no. 6812, p. 570, 2000.
- [40] E. E. Brodsky and N. J. van der Elst, “The uses of dynamic earthquake triggering,” *Annual Review of Earth and Planetary Sciences*, vol. 42, pp. 317–339, 2014.
- [41] H. M. Savage and C. Marone, “Effects of shear velocity oscillations on stick & slip behavior in laboratory experiments,” *J. Geophys. Res.*, vol. 112, p. 2301, 2007.
- [42] H. M. Savage and C. Marone, “Potential for earthquake triggering from transient deformations,” *Journal of Geophysical Research: Solid Earth*, vol. 113, no. B5, 2008.
- [43] D. Kilb, J. Gomberg, and P. Bodin, “Aftershock triggering by complete Coulomb stress changes,” *Journal of Geophysical Research: Solid Earth*, vol. 107, no. B4, pp. ESE 2–1–ESE 2–14, 2002.
- [44] F. Lorenzo-Martín, F. Roth, and R. Wang, “Elastic and inelastic triggering of earthquakes in the north anatolian fault zone,” *Tectonophysics*, vol. 424, no. 3–4, pp. 271–289, 2006.

- [45] J. Gomberg, P. Reasenberg, P. I. Bodin, and R. Harris, “Earthquake triggering by seismic waves following the landers and Hector mine earthquakes,” *Nature*, vol. 411, no. 6836, p. 462, 2001.
- [46] J. Gomberg, N. Beeler, M. Blanpied, and P. Bodin, “Earthquake triggering by transient and static deformations,” *Journal of Geophysical Research: Solid Earth*, vol. 103, no. B10, pp. 24411–24426, 1998.
- [47] M. Belardinelli, A. Bizzarri, and M. Cocco, “Earthquake triggering by static and dynamic stress changes,” *Journal of Geophysical Research: Solid Earth*, vol. 108, no. B3, 2003.
- [48] H. Perfettini, J. Schmittbuhl, and A. Cochard, “Shear and normal load perturbations on a two-dimensional continuous fault: 1. Static triggering,” *Journal of Geophysical Research: Solid Earth*, vol. 108, no. B9, pp. 1–16, 2003.
- [49] H. Perfettini and J. Schmittbuhl, “Shear and normal load perturbations on a two-dimensional continuous fault: 2. Dynamic triggering,” *J. Geophys. Res.*, vol. 108, no. B9, p. 2409, 2003.
- [50] S. Yoshida, “Numerical simulations of earthquake triggering by dynamic and static stress changes based on a revised friction law,” *Journal of Geophysical Research: Solid Earth*, vol. 123, no. 5, pp. 4109–4122, 2018.
- [51] S. Yoshida, T. Maeda, and N. Kato, “Earthquake triggering model based on normal-stress-dependent Nagata law: application to the 2016 Mie offshore earthquake,” *Earth, Planets and Space*, vol. 72, no. 1, pp. 1–13, 2020.
- [52] H. M. Savage and C. Marone, “Potential for earthquake triggering from transient deformations,” *J. Geophys. Res.*, vol. 113, p. 5302, 2008.
- [53] J. Gomberg, P. Reasenberg, M. Cocco, and M. E. Belardinelli, “A frictional population model of seismicity rate change,” *Journal of Geophysical Research: Solid Earth*, vol. 110, no. 5, pp. 1–10, 2005.
- [54] P. Bhattacharya and A. M. Rubin, “Frictional response to velocity steps and 1-d fault nucleation under a state evolution law with stressing-rate dependence,” *Journal of Geophysical Research: Solid Earth*, vol. 119, no. 3, pp. 2272–2304, 2014.

- [55] T. Parsons, “Recalculated probability of $m \geq 7$ earthquakes beneath the sea of marmara, turkey,” *Journal of Geophysical Research: Solid Earth*, vol. 109, no. B5, 2004.
- [56] M. Bohnhoff, F. Bulut, G. Dresen, P. E. Malin, T. Eken, and M. Aktar, “An earthquake gap south of Istanbul,” *Nature Communications* 2013 4:1, vol. 4, pp. 1–6, jun 2013.
- [57] M. B. Yıkılmaz, D. L. Turcotte, E. M. Heien, L. H. Kellogg, and J. B. Rundle, “Critical Jump Distance for Propagating Earthquake Ruptures Across Step-Overs,” *Pure and Applied Geophysics*, vol. 172, pp. 2195–2201, aug 2015.
- [58] G. Perrin, J. R. Rice, and G. Zheng, “Self-healing slip pulse on a frictional surface,” *Journal of the Mechanics and Physics of Solids*, vol. 43, no. 9, pp. 1461–1495, 1995.
- [59] E. Sopaci, “eyupsopaci/sset: Spring slider models for earthquake triggering simulations using rate and state friction,” Jan. 2023.
- [60] E. Sopaci, “Spectral boundary integral method for spontaneous failures using rate and state friction,” Dec. 2022.
- [61] E. E. Brodsky, “Long-range triggered earthquakes that continue after the wave train passes,” *Geophysical Research Letters*, vol. 33, p. L15313, 2006.
- [62] C. Aiken, X. Meng, and J. Hardebeck, “Testing for the ‘predictability’ of dynamically triggered earthquakes in the geysers geothermal field,” *Earth and Planetary Science Letters*, vol. 486, pp. 129–140, 2018.
- [63] E. Nissen, J. R. Elliott, R. A. Sloan, T. J. Craig, G. J. Funning, A. Hutko, B. E. Parsons, and T. J. Wright, “Limitations of rupture forecasting exposed by instantaneously triggered earthquake doublet,” *Nature Geoscience*, vol. 9, no. 4, pp. 330–336, 2016.
- [64] A. M. Freed, “Earthquake triggering by static, dynamic, and postseismic stress transfer,” *Annual Review of Earth and Planetary Sciences*, vol. 33, no. 1, pp. 335–367, 2005.

- [65] J. Gomberg, N. M. Beeler, M. L. Blanpied, and P. Bodin, “Earthquake triggering by transient and static deformations,” *Journal of Geophysical Research: Solid Earth*, vol. 103, no. 10, pp. 24411–24426, 1998.
- [66] J. Gomberg, “The failure of earthquake failure models,” *Journal of Geophysical Research: Solid Earth*, vol. 106, no. B8, pp. 16253–16263, 2001.
- [67] C. Voisin, “Dynamic triggering of earthquakes: The nonlinear slip-dependent friction case,” *Journal of Geophysical Research: Solid Earth*, vol. 107, no. B12, pp. ESE–10, 2002.
- [68] A. O. Konca, S. Leprince, J.-P. Avouac, and D. V. Helmberger, “Rupture process of the 1999 m w 7.1 duzce earthquake from joint analysis of spot, gps, insar, strong-motion, and teleseismic data: A supershear rupture with variable rupture velocity,” *Bulletin of the Seismological Society of America*, vol. 100, no. 1, pp. 267–288, 2010.
- [69] K. Nanjo, “Were changes in stress state responsible for the 2019 ridgecrest, california, earthquakes?,” *Nature communications*, vol. 11, no. 1, pp. 1–10, 2020.
- [70] S. Mancini, M. Segou, M. J. Werner, and T. Parsons, “The predictive skills of elastic coulomb rate-and-state aftershock forecasts during the 2019 ridgecrest, california, earthquake sequence,” *Bulletin of the Seismological Society of America*, vol. 110, no. 4, pp. 1736–1751, 2020.
- [71] J. L. Hardebeck, “A stress-similarity triggering model for aftershocks of the mw 6.4 and 7.1 ridgecrest earthquakes,” *Bulletin of the Seismological Society of America*, vol. 110, pp. 1716–1727, 8 2020.
- [72] J. Dieterich, “Applications of rate-and state-dependent friction to models of fault slip and earthquake occurrence. treat,” *Geophysics*, vol. 4, pp. 93–110, 2007.
- [73] J. R. Rice and S. T. Tse, “Dynamic motion of a single degree of freedom system following a rate and state dependent friction law,” *Journal of Geophysical Research: Solid Earth*, vol. 91, no. B1, pp. 521–530, 1986.

- [74] P. N. Brown, G. D. Byrne, and A. C. Hindmarsh, “Vode: A variable-coefficient ode solver,” *SIAM Journal on Scientific and Statistical Computing*, vol. 10, no. 5, pp. 1038–1051, 1989.
- [75] E. E. Brodsky and S. G. Prejean, “New constraints on mechanisms of remotely triggered seismicity at long valley caldera,” *Journal of Geophysical Research: Solid Earth*, vol. 110, no. B4, 2005.
- [76] J. H. Dieterich, “Earthquake nucleation on faults with rate-and state-dependent strength,” *Tectonophysics*, vol. 211, no. 1-4, pp. 115–134, 1992.
- [77] C. B. Worden, D. J. Wald, T. I. Allen, K. Lin, D. Garcia, and G. Cua, “A revised ground-motion and intensity interpolation scheme for shakemap,” *Bulletin of the Seismological Society of America*, vol. 100, pp. 3083–3096, 12 2010.
- [78] M. Utkucu, S. S. Nalbant, J. McCloskey, S. Steacy, and Ö. Alptekin, “Slip distribution and stress changes associated with the 1999 november 12, düzce (turkey) earthquake (mw= 7.1),” *Geophysical Journal International*, vol. 153, no. 1, pp. 229–241, 2003.
- [79] W. D. Barnhart, G. P. Hayes, and R. D. Gold, “The july 2019 ridgecrest, california, earthquake sequence: Kinematics of slip and stressing in cross-fault ruptures,” *Geophysical Research Letters*, vol. 46, no. 21, pp. 11859–11867, 2019.
- [80] J. Lozos and R. Harris, “Dynamic rupture simulations of the m6. 4 and m7. 1 july, 2019 ridgecrest, california earthquakes,” *Geophysical Research Letters*, p. e2019GL086020.
- [81] K. Chen, J.-P. Avouac, S. Aati, C. Milliner, F. Zheng, and C. Shi, “Cascading and pulse-like ruptures during the 2019 ridgecrest earthquakes in the eastern california shear zone,” *Nature Communications*, vol. 11, no. 1, pp. 1–8, 2020.
- [82] S. Yoshida, T. Maeda, and N. Kato, “Earthquake triggering model based on normal-stress-dependent Nagata law: application to the 2016 Mie offshore earthquake,” *Earth, Planets and Space*, vol. 72, no. 1, p. 141, 2020.

- [83] J. P. Ampuero and A. M. Rubin, “Earthquake nucleation on rate and state faults - Aging and slip laws,” *Journal of Geophysical Research: Solid Earth*, vol. 113, no. 1, pp. 1–21, 2008.
- [84] S. T. Tse and J. R. Rice, “Crustal earthquake instability in relation to the depth variation of frictional slip properties,” *Journal of Geophysical Research*, vol. 91, no. B9, p. 9452, 1986.
- [85] J. R. Rice, “Spatio-temporal complexity of slip on a fault,” *Journal of Geophysical Research: Solid Earth*, vol. 98, no. B6, pp. 9885–9907, 1993.
- [86] J. R. Rice and S. T. Tse, “Dynamic motion of a single degree of freedom system following a rate and state dependent friction law,” *Journal of Geophysical Research*, vol. 91, no. B1, pp. 521–530, 1986.
- [87] Y. Abe and N. Kato, “Complex earthquake cycle simulations using a two-degree-of-freedom spring-block model with a rate- and state-friction law,” *Pure and Applied Geophysics*, vol. 170, pp. 745–765, 5 2013.
- [88] M. Linker and J. H. Dieterich, “Effects of variable normal stress on rock friction: Observations and constitutive equations,” *Journal of Geophysical Research: Solid Earth*, vol. 97, no. B4, pp. 4923–4940, 1992.
- [89] P. Bhattacharya, A. M. Rubin, E. Bayart, H. M. Savage, and C. Marone, “Critical evaluation of state evolution laws in rate and state friction: Fitting large velocity steps in simulated fault gouge with time-, slip-, and stress-dependent constitutive laws,” *Journal of Geophysical Research: Solid Earth*, vol. 120, no. 9, pp. 6365–6385, 2015.
- [90] H. Perfettini and J.-P. Avouac, “Stress transfer and strain rate variations during the seismic cycle,” *Journal of Geophysical Research: Solid Earth*, vol. 109, 6 2004.
- [91] J. R. Cash and A. H. Karp, “A Variable Order Runge-Kutta Method for Initial Value Problems with Rapidly Varying Right-Hand Sides,” *ACM Transactions on Mathematical Software (TOMS)*, vol. 16, no. 3, pp. 201–222, 1990.

- [92] E. Sopacı, *Physics-based earthquake triggering and fault interactions*. PhD thesis, Middle East Technical University Geodetic-Geographic Information Technologies, Ankara, Turkey, 2023.
- [93] J.-H. Wang, “A review on scaling of earthquake faults,” *TAO: Terrestrial, Atmospheric and Oceanic Sciences*, vol. 29, no. 6, p. 5, 2018.
- [94] T. Hergert and O. Heidbach, “Geomechanical model of the marmara sea region—ii. 3-d contemporary background stress field,” *Geophysical Journal International*, vol. 185, no. 3, pp. 1090–1102, 2011.
- [95] D. Lange, H. Kopp, J. Y. Royer, P. Henry, Z. Çakir, F. Petersen, P. Sakic, V. Ballu, J. Bialas, M. S. Özeren, S. Ergintav, and L. Géli, “Interseismic strain build-up on the submarine North Anatolian Fault offshore Istanbul,” *Nature Communications*, vol. 10, no. 1, 2019.
- [96] Y. Yamamoto, N. Takahashi, A. Pinar, D. Kalafat, S. Citak, M. Comoglu, R. Polat, and Y. Kaneda, “Geometry and segmentation of the North Anatolian Fault beneath the Marmara Sea, Turkey, deduced from long-term ocean bottom seismographic observations,” *Journal of Geophysical Research: Solid Earth*, vol. 122, no. 3, pp. 2069–2084, 2017.
- [97] S. Ergintav, R. E. Reilinger, R. Cakmak, M. Floyd, Z. Cakir, U. Doğan, R. W. King, S. McClusky, and H. Özener, “Istanbul’s earthquake hot spots: Geodetic constraints on strain accumulation along faults in the marmara seismic gap,” *Geophysical Research Letters*, vol. 41, pp. 5783–5788, 8 2014.
- [98] J. Schmittbuhl, H. Karabulut, O. Lengliné, and M. Bouchon, “Long-lasting seismic repeaters in the Central Basin of the Main Marmara Fault,” *Geophysical Research Letters*, 2016.
- [99] G. Baltzopoulos, L. Luzi, and I. Iervolino, “Analysis of near-source ground motion from the 2019 ridgecrest earthquake sequence,” *Bulletin of the Seismological Society of America*, vol. 110, no. 4, pp. 1495–1505, 2020.
- [100] A. A. Ozacar, “The 2002 denali fault and 2001 kunlun fault earthquakes: Complex rupture processes of two large strike-slip events,” *Bulletin of the Seismological Society of America*, vol. 94, pp. S278–S292, 12 2004.

- [101] T. Hergert, O. Heidbach, A. Bécel, and M. Laigle, “Geomechanical model of the marmara sea region—i. 3-d contemporary kinematics,” *Geophysical Journal International*, vol. 185, no. 3, pp. 1073–1089, 2011.
- [102] E. Sopaci and A. A. Özacar, “Simulation of seismic triggering and failure time perturbations associated with the 30 October 2020 Samos earthquake (Mw 7.0),” *TURKISH JOURNAL OF EARTH SCIENCES*, vol. 30, pp. 653–664, sep 2021.
- [103] Y. Liu and J. R. Rice, “Spontaneous and triggered aseismic deformation transients in a subduction fault model,” *Journal of Geophysical Research*, vol. 112, p. B09404, 9 2007.
- [104] M. Wei, Y. Liu, Y. Kaneko, J. J. McGuire, and R. Bilham, “Dynamic triggering of creep events in the salton trough, southern california by regional $m \geq 5.4$ earthquakes constrained by geodetic observations and numerical simulations,” *Earth and Planetary Science Letters*, vol. 427, pp. 1–10, 10 2015.
- [105] M. Wei, Y. Kaneko, P. Shi, and Y. Liu, “Numerical modeling of dynamically triggered shallow slow slip events in new zealand by the 2016 mw 7.8 kaikoura earthquake,” *Geophysical Research Letters*, vol. 45, pp. 4764–4772, 5 2018.
- [106] A. Pizzi, A. D. Domenica, F. Gallović, L. Luzi, and R. Puglia, “Fault segmentation as constraint to the occurrence of the main shocks of the 2016 central italy seismic sequence,” *Tectonics*, vol. 36, pp. 2370–2387, 11 2017.
- [107] L. Gasperini, M. Stucchi, V. Cedro, M. Meghraoui, G. Uçarkus, and A. Polonia, “Active fault segments along the north anatolian fault system in the sea of marmara: implication for seismic hazard,” *Mediterranean Geoscience Reviews*, vol. 3, pp. 29–44, 3 2021.
- [108] P. Zhang, F. Mao, and D. Slemmons, “Rupture terminations and size of segment boundaries from historical earthquake ruptures in the basin and range province,” *Tectonophysics*, vol. 308, pp. 37–52, 7 1999.
- [109] S. G. Wesnousky, “Predicting the endpoints of earthquake ruptures,” *Nature*, vol. 444, pp. 358–360, 11 2006.

- [110] E. Richardson and C. Marone, “Effects of normal stress vibrations on frictional healing,” *Journal of Geophysical Research: Solid Earth*, vol. 104, pp. 28859–28878, 12 1999.
- [111] G. Karakaisis, “Effects of zonation on the results of the application of the regional time predictable seismicity model in greece and japan,” *Earth, planets and space*, vol. 52, no. 4, pp. 221–228, 2000.
- [112] K. H. Coban and N. Sayil, “Evaluation of earthquake recurrences with different distribution models in western anatolia,” *Journal of Seismology*, vol. 23, no. 6, pp. 1405–1422, 2019.
- [113] Z. Çakir, A. A. BARKA, and E. Evren, “Coulomb stress interactions and the 1999 marmara earthquakes,” *Turkish Journal of Earth Sciences*, vol. 12, no. 1, pp. 91–103, 2003.
- [114] N. J. van der Elst and H. M. Savage, “Frequency dependence of delayed and instantaneous triggering on laboratory and simulated faults governed by rate-state friction,” *Journal of Geophysical Research: Solid Earth*, vol. 120, no. 5, pp. 3406–3429, 2015.
- [115] E. Sopaci and A. A. Özacar, “Investigation of dynamic and static effects on earthquake triggering using different rate and state friction laws and marmara simulation,” in *EGU General Assembly Conference Abstracts*, p. 533, 2020.
- [116] S. Toda, R. S. Stein, V. Sevilgen, and J. Lin, “Coulomb 3.3 graphic-rich deformation and stress-change software for earthquake, tectonic, and volcano research and teaching—user guide,” *US Geological Survey open-file report*, vol. 1060, no. 2011, p. 63, 2011.
- [117] A. Ganas, P. Elias, P. Briole, V. Tsironi, S. Valkaniotis, J. Escartin, I. Karasante, and E. Efstathiou, “Fault responsible for samos earthquake identified. temblor,” 2020.
- [118] A. Ganas, P. Elias, P. Briole, S. Valkaniotis, J. Escartin, V. Tsironi, I. Karasante, and C. Kosma, “Co-seismic and post-seismic deformation, field observations and fault model of the 30 october 2020 mw= 7.0 samos earthquake, aegean sea,” *Acta Geophysica*, vol. 69, no. 3, pp. 999–1024, 2021.

- [119] V. Sakkas, “Ground deformation modelling of the 2020 mw6.9 samos earthquake (greece) based on insar and gnss data,” *Remote Sensing*, vol. 13, no. 9, p. 1665, 2021.
- [120] A. Akinci, D. Cheloni, and A. A. Dindar, “The 30 october 2020, m7.0 samos island (eastern aegean sea) earthquake: effects of source rupture, path and local-site conditions on the observed and simulated ground motions,” *Bulletin of Earthquake Engineering*, vol. 19, no. 12, pp. 4745–4771, 2021.
- [121] V. Karakostas, O. Tan, A. Kostoglou, E. Papadimitriou, and P. Bonatis, “Seis-motectonic implications of the 2020 samos, greece, mw 7.0 mainshock based on high-resolution aftershock relocation and source slip model,” *Acta Geophysica*, vol. 69, no. 3, pp. 979–996, 2021.
- [122] K. H. Chen, R. Bürgmann, and R. M. Nadeau, “Do earthquakes talk to each other? triggering and interaction of repeating sequences at parkfield,” *Journal of Geophysical Research: Solid Earth*, vol. 118, no. 1, pp. 165–182, 2013.
- [123] E. SOPACI, “Hız-ve-durum sürtünme yasaları ve burridge-knopoff yay blok sistemi kullanılarak depremlerin dinamik modellenmesi,” *Jeodezi ve Jeoinformasyon Dergisi*, vol. 6, no. 2, pp. 115–127, 2019.
- [124] J. Dieterich, V. Cayol, and P. Okubo, “The use of earthquake rate changes as a stress meter at kilauea volcano,” *Nature*, vol. 408, no. 6811, pp. 457–460, 2000.
- [125] M. Y. Thomas, J.-P. Avouac, and N. Lapusta, “Rate-and-state friction properties of the longitudinal valley fault from kinematic and dynamic modeling of seismic and aseismic slip,” *Journal of Geophysical Research: Solid Earth*, vol. 122, no. 4, pp. 3115–3137, 2017.
- [126] A. Ziv and A. M. Rubin, “Static stress transfer and earthquake triggering: No lower threshold in sight?,” *Journal of Geophysical Research: Solid Earth*, vol. 105, no. B6, pp. 13631–13642, 2000.
- [127] E. E. Brodsky, V. Karakostas, and H. Kanamori, “A new observation of dynamically triggered regional seismicity: Earthquakes in greece following the

- august 1999 izmit, turkey earthquake,” *Geophysical Research Letters*, vol. 27, no. 17, pp. 2741–2744, 2000.
- [128] E. Sopaci and A. A. Özacar, “Do large earthquakes along major faults synchronize in time?,” 2022.
- [129] C. Cattania and P. Segall, “Crack models of repeating earthquakes predict observed moment-recurrence scaling,” *Journal of Geophysical Research: Solid Earth*, vol. 124, pp. 476–503, 1 2019.
- [130] F. Corbi, F. Funiciello, S. Brizzi, S. Lallemand, and M. Rosenau, “Control of asperities size and spacing on seismic behavior of subduction megathrusts,” *Geophysical Research Letters*, vol. 44, pp. 8227–8235, 2017.
- [131] M. Rosenau, I. Horenko, F. Corbi, M. Rudolf, R. Kornhuber, and O. Oncken, “Synchronization of great subduction megathrust earthquakes: Insights from scale model analysis,” *Journal of Geophysical Research: Solid Earth*, vol. 124, pp. 3646–3661, 2019.
- [132] Y. Luo and J. P. Ampuero, “Stability of faults with heterogeneous friction properties and effective normal stress,” *Tectonophysics*, vol. 733, pp. 257–272, 2018.
- [133] E. Hairer, G. Wanner, and S. P. Nørsett, *Solving Ordinary Differential Equations I*, vol. 8. Springer Berlin Heidelberg, 1993.
- [134] B. A. Erickson, J. Jiang, M. Barall, N. Lapusta, E. M. Dunham, R. Harris, L. S. Abrahams, K. L. Allison, J. P. Ampuero, S. Barbot, C. Cattania, A. Elbanna, Y. Fialko, B. Idini, J. E. Kozdon, V. Lambert, Y. Liu, Y. Luo, X. Ma, M. B. McKay, P. Segall, P. Shi, M. V. D. Ende, and M. Wei, “The community code verification exercise for simulating sequences of earthquakes and aseismic slip (seas),” *Seismological Research Letters*, vol. 91, pp. 874–890, 2020.
- [135] K.-R. Koch, “Parameter estimation in linear models,” in *Parameter Estimation and Hypothesis Testing in Linear Models*, pp. 149–269, Springer, 1999.
- [136] M. Schatzman and M. Schatzman, *Numerical analysis: a mathematical introduction*. Oxford University Press on Demand, 2002.

- [137] M. Wei and P. Shi, “Synchronization of earthquake cycles of adjacent segments on oceanic transform faults revealed by numerical simulation in the framework of rate-and-state friction,” *Journal of Geophysical Research: Solid Earth*, vol. 126, pp. 1–15, 2021.
- [138] C. Cattania, “Complex Earthquake Sequences On Simple Faults,” *Geophysical Research Letters*, vol. 46, pp. 10384–10393, sep 2019.
- [139] P. Romanet and S. Ozawa, “Fully dynamic earthquake cycle simulations on a nonplanar fault using the spectral boundary integral element method (sbiem),” *Bulletin of the Seismological Society of America*, vol. 112, pp. 78–97, 2022.
- [140] F. Lorenzo-Martín, F. Roth, and R. Wang, “Elastic and inelastic triggering of earthquakes in the North Anatolian Fault zone,” *Tectonophysics*, vol. 424, pp. 271–289, oct 2006.
- [141] L. Wang, R. Wang, F. Roth, B. Enescu, S. Hainzl, and S. Ergintav, “Afterslip and viscoelastic relaxation following the 1999 M 7.4 İzmit earthquake from GPS measurements,” *Geophysical Journal International*, vol. 178, pp. 1220–1237, sep 2009.
- [142] M. Bouchon, H. Karabulut, M. Aktar, S. Özalaybey, J. Schmittbuhl, M.-P. Bouin, and D. Marsan, “The nucleation of the İzmit and Düzce earthquakes: some mechanical logic on where and how ruptures began,” *Geophysical Journal International*, vol. 225, no. 3, pp. 1510–1517, 2021.
- [143] H. Gürsoy, O. Tatar, Z. Akpınar, A. Polat, L. Mesci, and D. Tunçer, “New observations on the 1939 Erzincan Earthquake surface rupture on the Kelkit Valley segment of the North Anatolian Fault Zone, Turkey,” *Journal of Geodynamics*, vol. 65, pp. 259–271, apr 2013.

APPENDIX A

FULL INERTIAL EFFECTS ON SYNCHRONIZATION

A1. Full Inertial Effects on Synchronization We run several set-ups to check if applying full inertial effects change our conclusion on synchronization. We apply the type three kernel as proposed in [22]. The effective normal stress and $a - b_{asp}$ are set to 70 MPa and -0.005 rather than the parameters given in the table of the main manuscript, and initial conditions are set equal for the sake of comparison. Figure A.1 shows how rupture propagation is faster for the full-dynamic method than the quasi-dynamic (inertial effects are simplified to radiation damping). However in the end final values are quite similar.

Figure A.2 shows the results for the same parameters as in Figure A.1, but on three asperities with heterogeneous initial conditions. After four cycles, FD approximation does not differ significantly from QD, and it does not provide a better synchronization, either. Even, more partial ruptures emerge, which could be a cause of the accumulated error or a result of over-coupling as discussed in the manuscript.

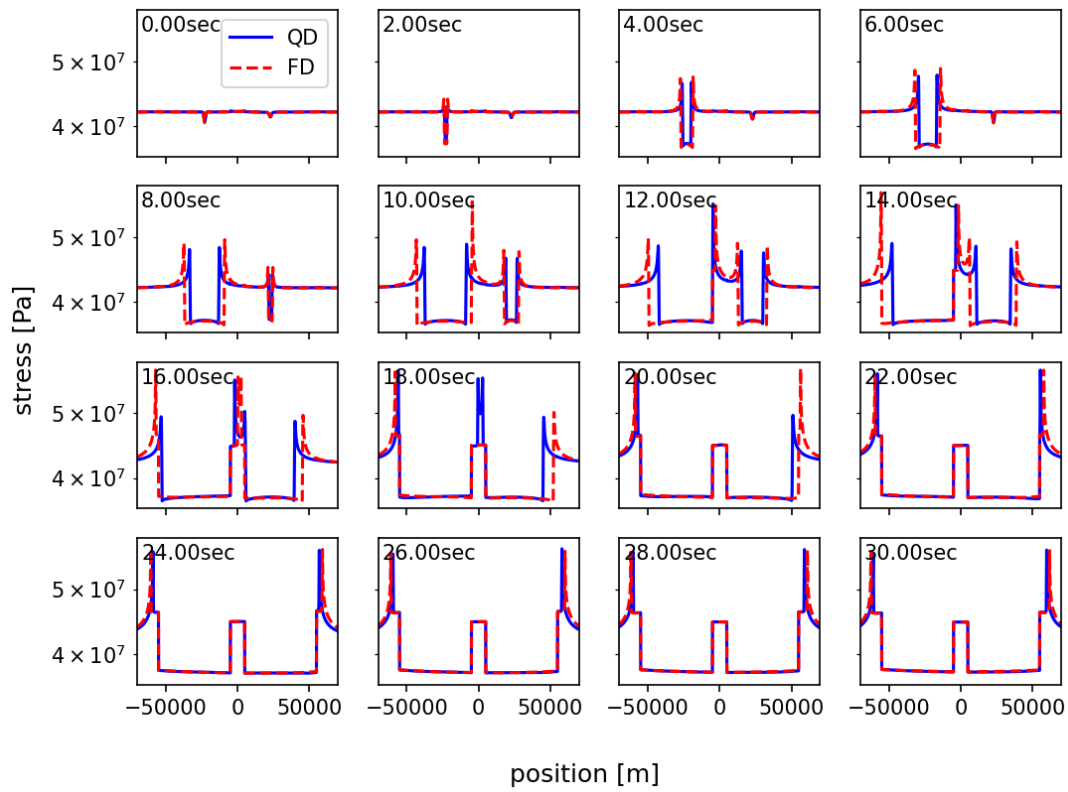


Figure A.1: The rupture difference between full-dynamic, and quasi-dynamic (inertial effects are simplified to radiation damping as all the simulations done in the main manuscript. The frames are plotted every 2 seconds for a two-asperity model. The color code for plots are given in the legend

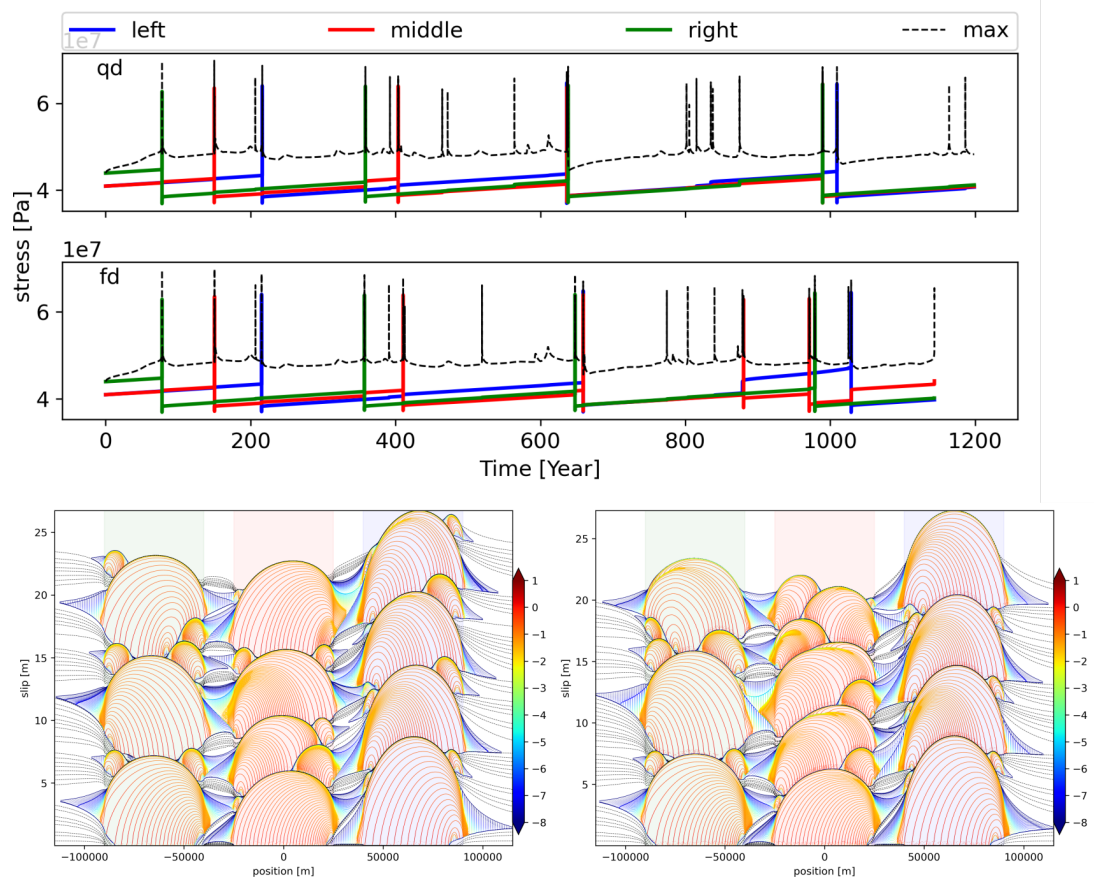


Figure A.2: Plots show the difference between FD and QD. The time series of stress are given on upper subplots. The slip profiles for qd (left) and fd (right) are given in below figures.

APPENDIX B

CURRICULUM VITAE

Surname, Name: Sopaci Eyüp

EDUCATION

Degree	Institution	Year
MS	KTU Geodesy	2013
BS	KTU Geodesy&Photog. Eng.	2008

FOREIGN LANGUAGES Turkish (mother tongue), English (Advance), German (B2)

Publication

1. Kayıkçı, E. T., & Sopacı, E. (2015). Testing the normality of the residuals of surface temperature data at VLBI/GPS co-located sites by goodness of fit tests. *Arabian Journal of Geosciences*, 11(8), 10119-10134.
2. SOPACI, E. (2019). Hız-ve-durum sürtünme yasaları ve Burridge-Knopoff yay blok sistemi kullanılarak depremlerin dinamik modellenmesi. *Jeodezi ve Jeoinformasyon Dergisi*, 6(2), 115-127.
3. SOPACI, E., & Özacar, A. A. (2021). Simulation of seismic triggering and failure time perturbations associated with the 30 October 2020 Samos earthquake (Mw 7.0). *Turkish Journal of Earth Sciences*, 30(5), 653-664.
4. Askan, A., Gülerce, Z., Roumelioti, Z., Sotiriadis, D., Melis, N. S., Altındal, A., ... & Margaris, B. (2021). The Samos Island (Aegean Sea) M7. 0 Earthquake: Analysis and engineering implications of strong motion data. *Bulletin of Earthquake*

Engineering,1-26.<https://doi.org/10.1007/s10518-021-01251-5>

5. Kiratzi, A., Papazachos, C., Özacar, A., Pinar, A., Kkallas, C., & Sopaci, E. (2021). Characteristics of the 2020 Samos earthquake (Aegean Sea) using seismic data. *Bulletin of Earthquake Engineering*, 1-23. <https://doi.org/10.1007/s10518-021-01239-1>

6. Gülerce, Z., Akbaş, B., Özacar, A. A., Sopacı, E., Önder, F. M., Uzel, B., ... & Unutmaz, B. (2022). Predictive performance of current ground motion models for recorded strong motions in 2020 Samos Earthquake. *Soil Dynamics and Earthquake Engineering*, 152, 107053. <https://doi.org/10.1016/j.soildyn.2021.107053>

7. Sopaci, E. and Özacar, A. A.: Do Large Earthquakes along Major Faults Synchronize in Time?, EGU General Assembly 2022, Vienna, Austria, 23–27 May 2022, EGU22-508, <https://doi.org/10.5194/egusphere-egu22-508>, 2022

8. Sopaci, E. and Özacar, A. A.: Simulation of Instant and Delayed Seismic Triggering Observed After the 30 October 2020 Samos Earthquake at Nearby Faults, EGU General Assembly 2021, online, 19–30 Apr 2021, EGU21-13090, <https://doi.org/10.5194/egusphere-egu21-13090>, 2021.

9. Sopaci, E. and Özacar, A. A.: Investigation of Dynamic and Static Effects on Earthquake Triggering Using Different Rate and State Friction Laws and Marmara Simulation, EGU General Assembly 2020, Online, 4–8 May 2020, EGU2020-533, <https://doi.org/10.5194/egusphere-egu2020-533>, 2019